CHALMERS

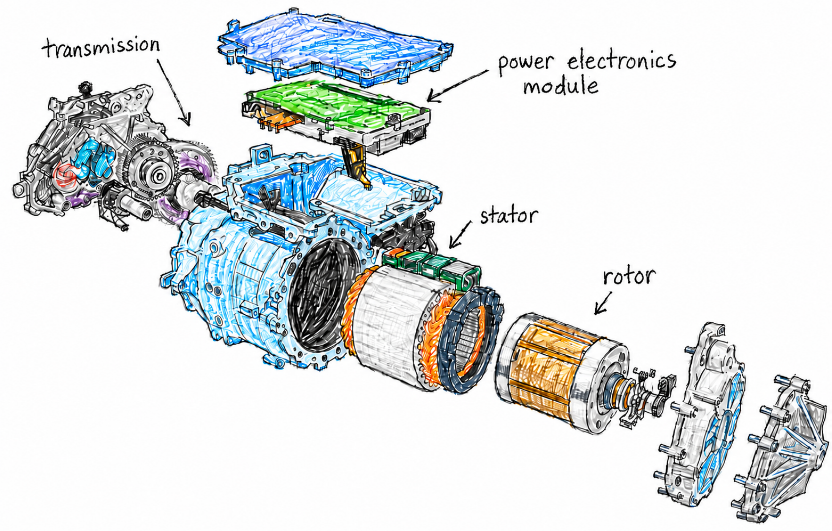

Towards Highly Efficient Electric Vehicle Powertrains

Architecture, Control, and Thermal Management

YU XU

Division of Energy Conversion and Propulsion Systems
Department of Mechanical Engineering
CHALMERS UNIVERSITY OF TECHNOLOGY
Göteborg, Sweden 2026

THESIS FOR THE DEGREE OF DOCTOR OF PHILOSOPHY IN THERMO AND FLUID DYNAMICS

Towards Highly Efficient Electric Vehicle Powertrains

Architecture, Control, and Thermal Management

YU XU

Department of Mechanical Engineering

CHALMERS UNIVERSITY OF TECHNOLOGY

Göteborg, Sweden 2026

Towards Highly Efficient Electric Vehicle Powertrains
Architecture, Control, and Thermal Management
YU XU
ISBN 978-91-8103-479-0

Doktorsavhandlingar vid Chalmers Tekniska Högskola
Ny serie nr. 5936
ISSN 0346-718X
Division of Energy Conversion and Propulsion Systems
Department of Mechanical Engineering
Chalmers University of Technology
SE-412 96 Göteborg
Sweden
Telephone: +46 (0)72-574 31 08

Cover Picture: Illustration of the Main Components of an Electric Drive Unit.

Chalmers Reproservice
Göteborg, Sweden 2026

Abstract

Battery electric vehicles are central to the transition toward sustainable road transport, yet their widespread adoption remains constrained by limited driving range and the cost, mass, and environmental burden associated with larger battery packs. Improving powertrain energy efficiency offers an alternative route to extend driving range without increasing battery capacity. This thesis investigates system-level methods for enhancing BEV powertrain efficiency through coordinated developments in powertrain architecture, control, and thermal management.

This thesis first examines powertrain architectures that introduce additional operational degrees of freedom. A dual-motor powertrain with disconnect functionality is investigated, where front and rear electric drive units can be selectively decoupled to eliminate no-load losses. An energy management strategy is developed to optimize operating mode selection and torque distribution while accounting for transient synchronization losses. Simulation results show that the proposed configuration reduces WLTC energy consumption by 8.21% compared with a conventional dual-motor powertrain. In addition, a configuration-aware motor design optimization framework is proposed to tailor the front and rear motors to the added flexibility, providing a further reduction in energy consumption.

This thesis also investigates control-oriented approaches for improving powertrain efficiency. For a single-motor powertrain with disconnect functionality, an eco-driving strategy is developed to exploit free-coasting through predictive optimization of traction torque and clutch state. Results show that energy consumption can be reduced by up to 11.6% on representative real-world routes. Furthermore, a torque modulation strategy is proposed to improve efficiency at low load by replacing continuous low torque operation with pulsating torque commands of equal average value. The modulation strategy is optimized at the whole-powertrain level and shown to reduce WLTC energy consumption by 1.05% for a single-motor powertrain and 2.21% for a dual-motor powertrain, while maintaining acceptable driver comfort.

The thesis further studies adjustable DC-link voltage as an additional efficiency measure. By introducing a bidirectional DC-DC converter between the battery and inverter, the DC-link voltage can be adapted to the operating condition to minimize the powertrain losses. Results show that this approach can reduce WLTC energy consumption by up to 3.25%, with larger benefits at low battery state of charge and when SiC-based power electronics are used.

The thesis further studies adjustable DC-link voltage as an additional efficiency measure. By introducing a bidirectional DC-DC converter between the battery and inverter, the DC-link voltage can be adapted to the operating condition to minimize the powertrain losses. Results show that this approach can reduce WLTC energy consumption by up to 3.25%, with larger benefits at low battery state of charge and when SiC-based power electronics are used. Further analysis with a high-voltage 900 V battery system shows that the adjustable DC-link voltage is not only beneficial for conventional 300–400 V architectures but also applicable to emerging high-voltage platforms.

Finally, this thesis develops an energy-efficient thermal management strategy. By coordinating coolant flow, oil flow, radiator fan operation, and active grille shutter position, the controller minimizes the combined energy consumption of the powertrain and its auxiliaries while respecting component temperature limits. Compared with a conventional rule-based strategy, the proposed method reduces energy consumption in both urban and highway driving.

In summary, this thesis presents a comprehensive study on efficiency-oriented design and control of battery electric vehicle powertrains. The results show that significant energy savings can be achieved by systematically introducing and exploiting additional degrees of freedom in powertrain architecture, operation, and thermal management.

Keywords: Battery electric vehicles, Electric powertrain efficiency, Electric drive unit, Powertrain architecture, Energy management, Thermal management, Powertrain optimization

List of publications

This thesis summarizes the author's work reported in the following publications:

Paper I **Y. Xu**, A. Kersten, S. Klacar, B. Ban, J. Hellsing, and D. Sedarsky. "Improved efficiency with adaptive front and rear axle independently driven powertrain and disconnect functionality." *Transportation Engineering, Volume 13, Pages 100192, 2023*

Paper II **Y. Xu**, A. Kersten, S. Klacar, and D. Sedarsky. "Maximizing Efficiency in Smart Adjustable DC Link Powertrains with IGBTs and SiC MOSFETs via Optimized DC-Link Voltage Control." *Batteries, Volume 9, Number 6, Pages 302, 2023*

Paper III **Y. Xu**, P. Lokur, S. Klacar, S. George, A. Andersson, D. Sedarsky, and N. Murgovski. "Maximizing the Energy-Saving Potential of Declutchable BEV Powertrains Via Eco-Driving." *2024 IEEE International Conference on Electrical Systems for Aircraft, Railway, Ship Propulsion and Road Vehicles & International Transportation Electrification Conference (ESARS-ITEC), Pages 1–6, 2024*

Paper IV **Y. Xu**, P. Ingelström, A. Kersten, A. Andersson, S. Klacar, S. George, and D. Sedarsky. "Improving Powertrain Efficiency Through Torque Modulation Techniques in Single and Dual Motor Electric Vehicles." *Transportation Engineering, Volume 18, Pages 100289, 2024*

Paper V **Y. Xu**, S. Klacar, S. George, A. Andersson, D. Sedarsky, and A. Kersten. "Optimizing Thermal Management in Battery Electric Vehicle Powertrains with Energy-Efficient Model Predictive Control." *Applied Thermal Engineering, Pages 129897, 2026*

Paper VI **Y. Xu**, J. Hellsing, S. Klacar, D. Sedarsky, and A. Kersten. "Utilizing Disconnect Function in Dual Motor Powertrain via Motor Design Optimization." *IEEE Transactions on Vehicular Technology, Under Review*

Paper VII **Y. Xu**. "Adjustable DC-Link Voltage Powertrains: A Comparison of Different Battery Voltage Levels." *Submitted to 2026 IEEE Transportation Electrification Conference and Expo, Asia-Pacific (ITEC Asia-Pacific)*

The author also contributed to the following publications although they are not covered in this thesis:

Paper I **Y. Xu**, A. Kersten, P. Ingelström, S. Amirpour, S. Klacar, and D. Sedarsky. "Comparative Study of Efficiency Improvement with Adjustable DC-Link Voltage Powertrain Using DC-DC Converter and Quasi-Z-Source Inverter." *2023 IEEE Transportation Electrification Conference and Expo, Asia-Pacific (ITEC Asia-Pacific), Pages 1–5, 2023*

Paper II S. Amirpour, T. Thiringer, and **Y. Xu**. "Mapping an Optimum DC-Link Voltage Across the Entire SiC-Based EV Drive Regions Using a Synchronous Boost DC-DC Converter." *WCX SAE World Congress Experience, 2024*

Paper III S. Amirpour, T. Thiringer, S. Soltanipour, and **Y. Xu**. "Optimal DC-Link Voltage Mapping for SiC-Based EV Drives Accounting for a Synchronous Boost Converter." *IEEE Access, 2025*

Acknowledgements

Finally, I have arrived at this very special moment that I have been looking forward to for so long. Five years ago, when I decided to pursue a PhD, I expected the journey to be a roller coaster, with moments of excitement, uncertainty, challenge, and growth. Looking back now, I feel incredibly fortunate that the ride has been far smoother and more rewarding than I ever imagined. This is not because the journey was always easy, but because I was never walking it alone. So many people have supported me, believed in me, encouraged me, and made these five years truly meaningful. This thesis carries my name on the cover, but this moment belongs, in many ways, to all of them as well.

First and foremost, I would like to express my deepest gratitude to my academic supervisor, Prof. David Sedarsky, for the trust he has placed in me and for his unwavering support and guidance throughout my research. I am equally grateful to my co-supervisor, Prof. Nikolce Murgovski, for his valuable insights in optimization and for the thoughtful advice that has contributed significantly to the progress and quality of my research.

I am deeply grateful to all of my industrial supervisors throughout the years, Leon Löwered, Dr. Simon Klacar, and Johan Hellsing. Although their roles have changed over the years due to organizational changes, from serving as technical leads in regular work to supervising my research and coordinating the PhD project, their commitment and guidance have remained constant. I am especially grateful for the many valuable discussions, opportunities, and encouragement they have provided along the way, without which I could not have made it this far.

My sincere gratitude also goes to my colleagues at CEVT, Zeekr/Geely Technology Europe, and Infimotion Technology Europe, including Dr. Anton Kersten, Dr. Andreas Andersson, Dr. Sepideh Amirpour, Dr. Pär Ingelström, , Shino George, Martin Nyman, Dr. Jianning Zhao, and many others, for their generous technical support and extensive expertise in power electronics, electric machines, and transmissions. As my research has spanned many different aspects of the powertrain system, this work would not have been possible without their willingness to share their knowledge, experience, and perspectives.

A very special thanks goes to Prashant Lokur, who started this PhD journey alongside me as part of the same research project. More than just a colleague, he has been a true comrade throughout these years. We have shared countless technical discussions, frustrations, excitement, doubts, and achievements, and experienced many of the ups and downs of the PhD journey together. I am deeply grateful for his support and companionship along the way.

I am also grateful to my project leaders and managers over the years, Dr. John Bergström, Dr. Jesper Marklund, Dr. Håkan Sandquist, Matthias Abrahamsson, Mark Saukkonen, and Fangkun Lindström, for their invaluable support and help in navigating the many administrative and organizational matters surrounding the project, which allowed me to focus more fully on the research itself.

Beyond the research itself, I would like to thank all my fellow PhD students at the Division of ECAPS — some of whom have already earned the title of Dr. along the way — including Pratheeba, Mohammad, Nidal, Christian, Lokesh, Lahari, Mina, Abhilash, Victor, Elvin, Vincent, and Nandu, as well as the senior staff, for making these years so enjoyable. I am equally grateful to my colleagues at the Division of MES for contributing to such a friendly and enjoyable working environment. I will always remember the many lunches and fika breaks, BBQs, Friday dinners, and spontaneous moments of laughter and conversation we shared.

The research presented in this thesis has been funded by Geely Technology Europe, Infimotion Technology Europe, and the Swedish Energy Agency (Energimyndigheten). Their financial support has made this research project possible, and I am sincerely grateful for the opportunities it has provided.

Finally, and most importantly, I could not have done this without the love and support of my partner, Ann-Sofie Eriksson. Her patience, encouragement, and belief in me have meant more than I can put into words, especially during the long days, stressful moments, and times when work demanded more attention than it probably should have. Knowing that she was always by my side made this journey much easier to carry. I am deeply grateful for everything we have shared along the way, and I could not have imagined reaching this moment without her.

Yu Xu 许煜
Göteborg 2026

To Ann-Sofie,

致予你，止于你，
只与你，挚予你。

For you, with you.
only you, always you.

Contents

Abstract i

List of publications iii

Acknowledgements v

List of Figures xii

List of Tables xv

1 Introduction 1
1.1 Motivation . . . 1
1.2 Objectives . . . 3
1.3 Research gaps and contributions . . . 4

2 Background 9
2.1 Powertrain losses . . . 9
2.1.1 Battery . . . 9
2.1.2 Power electronics . . . 10
2.1.3 Electric motor . . . 13
2.1.4 Transmission . . . 16
2.1.5 Drive-cycle analysis . . . 16
2.2 Control strategy . . . 18
2.2.1 Rule-based strategy . . . 18
2.2.2 Optimization-based strategy . . . 18

3 Dual-Motor Powertrain Utilizing Disconnect Functionality 21
3.1 Powertrain configuration . . . 21
3.2 Operating principle . . . 22
3.2.1 Disconnect functionality . . . 22
3.2.2 Energy management strategy . . . 23
3.3 Motor design optimization . . . 26
3.3.1 Problem formulation . . . 26
3.3.2 EDU loss map estimation . . . 27
3.3.3 Optimization framework . . . 29

3.4 Results and discussion 30
3.4.1 Casy study: comparison between AFRID and FRID 30
3.4.2 Configuration-aware motor design optimization 33
3.4.3 Number of clutch and motor asymmetry 37
3.4.4 Summary 38

4 Eco-driving with Disconnect Functionality 41
4.1 Free-coasting operation 41
4.2 Eco-driving strategy 42
4.2.1 Problem formulation 42
4.2.2 MPC setup 46
4.3 Results and discussion 46
4.3.1 Driving route 46
4.3.2 Efficiency improvement 47
4.3.3 Summary 48

5 Adjustable DC-link Voltage 51
5.1 Powertrain configuration 51
5.2 Operating principle 51
5.2.1 Varying DC-link voltage 51
5.2.2 DC-link voltage optimization 53
5.3 Results and discussion 54
5.3.1 Boost configuration with Si and SiC devices 54
5.3.2 Buck configuration in 900 V system 58
5.3.3 Summary 60

6 Powertrain Torque Modulation 61
6.1 Operating principle 61
6.2 Optimal modulation strategy 63
6.2.1 Modulation duty cycle 63
6.2.2 Modulation frequency 67
6.3 Results and discussion 70
6.3.1 Optimal modulation duty cycle 70
6.3.2 Driver comfort 71
6.3.3 Efficiency improvement 73
6.3.4 Summary 74

7 Energy-Efficient Powertrain Thermal Management 77
7.1 Thermal management system 77
7.2 Energy-efficient powertrain thermal management strategy 78
7.2.1 Problem formulation 78
7.2.2 MPC setup 80
7.3 Control-oriented model 81
7.3.1 Thermal model 81
7.3.2 Auxiliary component 84
7.3.3 Temperature-dependent loss 86

7.4 Results and discussion 87
7.4.1 Rule-based strategy 87
7.4.2 Driving route 89
7.4.3 Efficiency improvement 89
7.4.4 Summary 95

8 Conclusions and Future Work **97**
8.1 Conclusions and discussion 97
8.2 Future work 99

Bibliography **101**

List of Figures

1.1 Global electric car sales by powertrain and region (IEA), 2014–2024. [4] . 1
1.2 Typical energy losses distribution of a BEV [13]. 2
1.3 Typical BEV powertrain. 3
1.4 Sankey diagram of a typical BEV powertrain. 3
2.1 Battery equivalent circuit models. (a) Simplified model (b) Thevenin equivalent circuit model. 9
2.2 Non-isolated bidirectional buck–boost converter scheme. 10
2.3 Three phase inverter scheme. 12
2.4 PMSM equivalent electric circuit model. 13
2.5 Illustration of MTPA control strategy. 14
2.6 Vehicle speed profile of WLTC. 17
2.7 Forces acting on a vehicle in the longitudinal direction. 17
3.1 AFRID powertrain configuration with front- and rear-axle EDUs including clutches. Each EDU consists of a transmission, a three-phase motor, and an inverter. 21
3.2 EDU no-load losses. 22
3.3 Illustration of the dog clutch. (a) Structure. (b) Engagement process. . . 22
3.4 Parameterized motor geometry and selected design variables for the V-shaped IPMSM. 26
3.5 Procedure for motor loss map calculation. 28
3.6 Two-level PSO-based optimization framework for the AFRID powertrain. 29
3.7 Efficiency maps. (a) Front EDU. (b) Rear EDU. 31
3.8 Powertrain with the investigated front and rear EDUs. (a) Optimal torque split ratio in AWD mode. (b) Operating modes with minimal powertrain loss. 31
3.9 Overview of the GT-Suite simulation model. 32
3.10 Instantaneous powertrain loss of FRID and AFRID powertrains under the WLTC drive cycle. 33
3.11 Motor efficiency maps. Left column: predicted. Middle column: FEM. Right column: absolute difference $|\eta_{\mathrm{pred}} - \eta_{\mathrm{FEM}}|$ (%). (a)–(c) Front (=rear) motor for reference AFRID powertrain. (d)–(f) Optimized front motor for AFRID powertrain. (g)–(i) Optimized rear motor for AFRID powertrain. 35
3.12 Operating mode sequences over the WLTC driving cycle. (a) Reference AFRID powertrain. (b) Optimized AFRID powertrain. 36

3.13 Operating points of each EDU projected onto the EDU efficiency maps under different operating modes over the WLTC drive cycle. (a) Front EDU of reference AFRID. (b) Rear EDU of reference AFRID. (c) Front EDU of optimized AFRID. (d) Rear EDU of optimized AFRID. 37
4.1 Single-motor powertrain with disconnect functionality. 41
4.2 EDU loss map and torque envelope in reference to vehicle speed and EDU torque. 44
4.3 Transient energy loss during engagement and disengagement events in reference to vehicle speed. 45
4.4 Investigated representative routes in the Västra Götalands region, Sweden. 47
4.5 Structure of the co-simulation framework. 47
4.6 Vehicle speed under eco-driving compared to the reference profile. (a, c, e) Powertrain without disconnect functionality. (b, d, f) Powertrain with disconnect functionality. Rows represent LS, MS, and HS driving scenarios, respectively. 49
5.1 Adjustable DC-link voltage powertrain configuration with bidirectional DC-DC converter. 51
5.2 Motor loss maps with different DC-link voltages. (a) 250 V (b) 450 V. . . 52
5.3 Inverter loss maps with different DC-link voltages (Infineon FS820R08A6P2B IGBT module). (a) 250 V (b) 450 V. 52
5.4 Battery pack data under charge and discharge conditions. (a) OCV. (b) Internal resistance. 55
5.5 Simulation scheme in PLECS. 56
5.6 Optimized DC-link voltage in adjustable DC-link voltage powertrain compared with DC-link voltage in baseline powertrain. (a) IGBT-based powertrains. (b) MOSFET-based powertrains. 57
5.7 Powertrain loss breakdown. 57
5.8 Motor loss map at 900 V DC-link voltage. 58
5.9 Powertrain loss breakdown over the WLTC drive cycle. 59
5.10 Optimized DC-link voltage over the WLTC drive cycle. (a) Buck configuration (with minimum 50 V DC-link voltage). (b) Boost configuration. 60
6.1 Combined efficiency map of inverter and motor assembly. 61
6.2 Illustration of torque modulation with a duty cycle of 0.5. 62
6.3 Relative proportion of iron losses to the sum of iron and copper losses. . . 62
6.4 Transmission efficiency map. 63
6.5 Possible scenarios of torque modulation in a dual-motor powertrain. (a) Scenario I: $D_f + D_r < 1$. (b) Scenario II: $D_f + D_r = 1$. (c) Scenario III: $D_f + D_r > 1$. 66
6.6 Illustration of torque and three-phase current response. (a) Motor torque response with PI control. (b) Phase currents with PI control. (c) Motor torque response with deadbeat control. (d) Phase currents with deadbeat control. 69
6.7 ISO2631 frequency weighting curves. 70
6.8 Optimal modulation duty cycle of the single-motor powertrain. 70

6.9 Optimal modulation duty cycle of the dual-motor powertrain with $T_f = T_r = \frac{T_{\mathrm{dem}}}{2D}$. 71
6.10 Calculation procedure of VTV value. 72
6.11 VTV values of single- and dual-motor powertrains with optimal modulation duty cycle at different torque modulation frequencies. (a), (c), and (e) correspond to the single-motor powertrain at 10 Hz, 15 Hz, and 20 Hz, respectively. (b), (d), and (f) correspond to the dual-motor powertrain at 10 Hz, 15 Hz, and 20 Hz, respectively. 72
6.12 WLTC drive-cycle losses breakdown. (a) Single-motor powertrain. (b) Dual-motor powertrain. 74
6.13 WLTC drive-cycle powertrain operating points projected on the effective torque modulation area. (a) Single-motor powertrain. (b) Dual-motor powertrain. 74
7.1 Schematic of the investigated powertrain thermal management system. . . 77
7.2 Inverter cooling system and thermal model. (a) Geometry. (b) Reduced-order LPTN representation. 81
7.3 Motor cooling system and thermal model. (a) Geometry. (b) Reduced-order LPTN representation. 82
7.4 Rule-based powertrain thermal management strategy. 88
7.5 Speed profile and road grade of the representative real-world driving routes. (a) Urban. (b) Highway. 89
7.6 Implementation of the MPC-based thermal management strategy and its closed-loop interaction with the powertrain plant model. 90
7.7 Breakdown of energy usage difference between rule-based and MPC-based thermal management strategies. (a) Urban route and (b) Highway route. 91
7.8 Actuator control commands and key component temperatures for the urban route. (a) AGS angle. (b) Fan PWM duty cycle. (c) Coolant flow rate. (d) Oil flow rate. (e) Inverter junction temperature. (f) Motor winding temperature. (g) Motor magnet temperature. (h) Transmission sump oil temperature. 92
7.9 Actuator control commands and key component temperatures for the highway route. (a) AGS angle. (b) Fan PWM duty cycle. (c) Coolant flow rate. (d) Oil flow rate. (e) Inverter junction temperature. (f) Motor winding temperature. (g) Motor magnet temperature. (h) Transmission sump oil temperature. 94

List of Tables

3.1 Considered motor design parameters and bounds. 26
3.2 Vehicle parameters. 30
3.3 Energy consumption under WLTC drive cycle. 32
3.4 Optimal motor design parameters for the reference and optimized AFRID powertrains. 34
3.5 WLTC energy consumption and acceleration performance. 36
4.1 Energy consumption for different driving routes. 48
5.1 Energy consumption of baseline and adjustable DC-link voltage powertrains under the WLTC drive cycle at 80% battery SoC. 55
5.2 Energy consumption of baseline and adjustable DC-link voltage powertrains under the WLTC drive cycle at 20% battery SoC. 57
5.3 Investigated battery pack configurations. 58
5.4 WLTC drive-cycle energy consumption of investigated powertrains. 59
6.1 Approximate indications of likely reactions to various VTVs. 69
6.2 WLTC drive-cycle energy consumption of single- and dual-motor powertrains. 73
7.1 Energy consumption of rule-based and MPC-based thermal management strategies. 90

Nomenclature

Abbreviations

AC **A**lternating **C**urrent

AFRID **A**daptive **F**ront and **R**ear axle **I**ndependently **D**riven

AGS **A**ctive **G**rille **S**hutter

AWD **A**ll-**W**heel-**D**rive

BEV **B**attery **E**lectric **V**ehicle

DC **D**irect **C**urrent

DP **D**ynamic **P**rogramming

EDU **E**lectric **D**rive **U**nit

EMS **E**nergy **M**anagement **S**trategy

FEM **F**inite **E**lement **M**ethod

FFT **F**ast **F**ourier **T**ransformation

FRID **F**ront and **R**ear axle **I**ndependently **D**riven

FWD **F**ront-**W**heel-**D**rive

ICEV **I**nternal **C**ombustion **E**ngine **V**ehicle

IGBT **I**nsulated **G**ate **B**ipolar **T**ransistor

IPMSM **I**nterior **P**ermanent **M**agnet **S**ynchronous **M**achine

IPOPT **I**nterior **P**oint **Op**timizer

LPTN **L**umped **P**arameter **T**hermal **N**etwork

LUT **L**ook-**U**p **T**able

MINLP **M**ixed-**I**nteger **N**on**l**inear **P**rogramming

MOSFET **M**etal-**O**xide-**S**emiconductor **F**ield-**E**ffect **T**ransistor

MPC **M**odel **P**redictive **C**ontrol

MTPV **M**aximum **T**orque **P**er **V**oltage

NLP **N**on-**L**inear **P**rogramming

NLP **N**on**l**inear **P**rogramming

NN **N**eural **N**etwork

OCP **O**ptimal **C**ontrol **P**roblem

OCV **O**pen **C**ircuit **V**oltage

PI **P**roportional-**I**ntegral

PMSM **P**ermanent **M**agnet **S**ynchronous **M**achine

PSO	**P**article **S**warm **O**ptimization
PWM	**P**ulse-**W**idth **M**odulation
RMS	**R**oot-**M**ean-**S**quare
RWD	**R**ear-**W**heel-**D**rive
SiC	**S**ilicon **C**arbide
SoC	**S**tate of **C**harge
SQP	**S**equential **Q**uadratic **P**rogramming
SVPWM	**S**pace **V**ector **P**ulse-**W**idth **M**odulation
VTV	**V**ibration **T**otal **V**alue
WLTC	**W**orldwide **H**armonized **L**ight vehicles **T**est **C**ycle

1 Introduction

This chapter introduces the motivation, research objectives, and the main scientific contributions addressed in this thesis.

1.1 Motivation

The transportation sector is currently undergoing a profound technological transformation driven by the urgent need to mitigate climate change and reduce greenhouse gas emissions. Road transport accounts for a substantial share of global CO_2 emissions and energy consumption, making it a central focus of decarbonization strategies worldwide [1, 2]. In response, electrification of the road vehicle has emerged as one of the most promising pathways toward sustainable mobility.

Battery electric vehicles (BEVs) have gained significant attention due to their absence of tailpipe emissions and their potential to reduce life-cycle greenhouse gas emissions when powered by low-carbon electricity [3]. Over the past decade, rapid technological advancements, falling battery costs, and supportive governmental policies have contributed to a strong increase in global BEV adoption. Annual sales of electric vehicles have grown exponentially across major markets such as China, Europe, and the United States as depicted in Figure 1.1. This upward trend reflects both regulatory pressure and increasing consumer acceptance of electrified transportation.

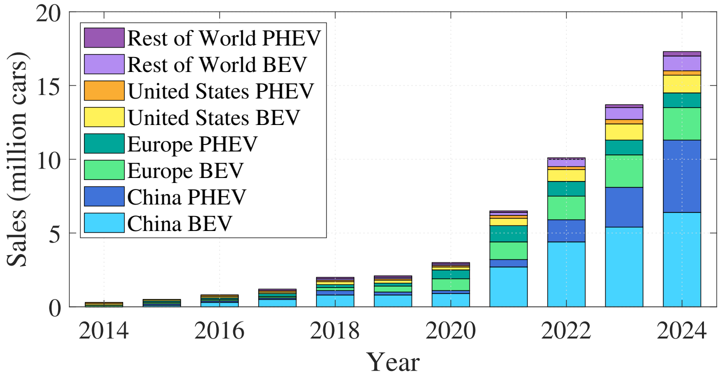

Figure 1.1: *Global electric car sales by powertrain and region (IEA), 2014–2024. [4]*

Despite the rapid growth, several technical challenges continue to hinder the widespread adoption of BEVs. One of the most frequently cited concerns is limited driving range, commonly referred to as “range anxiety”. This concern is not solely associated with the nominal driving range of the vehicle, but is further exacerbated by inadequate charging infrastructure, prolonged charging durations, and uncertainty in trip planning [5–8]. Although charging networks are continuously expanding, battery energy density remains a fundamental technological constraint. Lithium-ion batteries, which currently dominate the market, have seen significant improvements over the past decade. Advances in materials and cell design have increased gravimetric energy density from approximately 150 Wh/kg in 2010–2011 to around 250–260 Wh/kg in 2024 [9–11]. Despite this progress, batteries still impose practical limitations on vehicle range, overall cost, and vehicle mass [12].

Increasing battery capacity represents a straightforward approach to extending driving range. However, this strategy introduces significant trade-offs. Larger battery packs increase vehicle mass, require more raw materials, and lead to higher production-related environmental impacts, while also substantially increasing cost. Consequently, relying solely on battery scaling is neither economically nor environmentally optimal, which motivates the exploration of alternative approaches to extend driving range through improved vehicle energy efficiency. Figure 1.2 illustrates a typical distribution of energy losses within a BEV. A considerable portion of the total energy consumption is associated with the powertrain, which typically consists of a high-voltage battery pack, an inverter, an electric motor, and a transmission as illustrated in Figure 1.3. The combination of the inverter, electric motor, and transmission is commonly referred to as an electric drive unit (EDU).

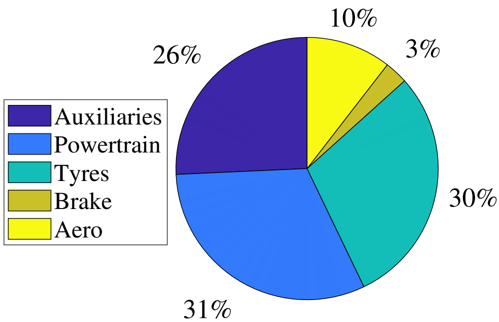

Figure 1.2: *Typical energy losses distribution of a BEV [13].*

In BEVs, the electric powertrain converts electrical energy stored in the high-voltage battery into mechanical energy at the wheels. The battery supplies direct current (DC) power, which is converted by the inverter into alternating current (AC) power suitable for driving the electric motor. The motor generates mechanical torque, which is transmitted to the wheels through a transmission that adjusts the speed and torque to match driving conditions. At each stage of the energy conversion process, energy losses occur for both propulsion and regenerative braking operations as visualized in Figure 1.4. The accumulation of these losses reduces the proportion of battery energy that is effectively

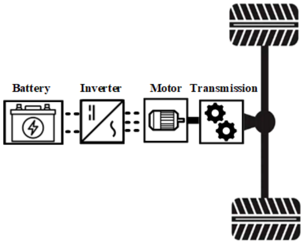

Figure 1.3: *Typical BEV powertrain.*

converted into useful vehicle motion, thereby constraining the achievable driving range. Consequently, enhancing powertrain energy efficiency offers a more sustainable pathway to extend driving range without increasing battery capacity [9, 14].

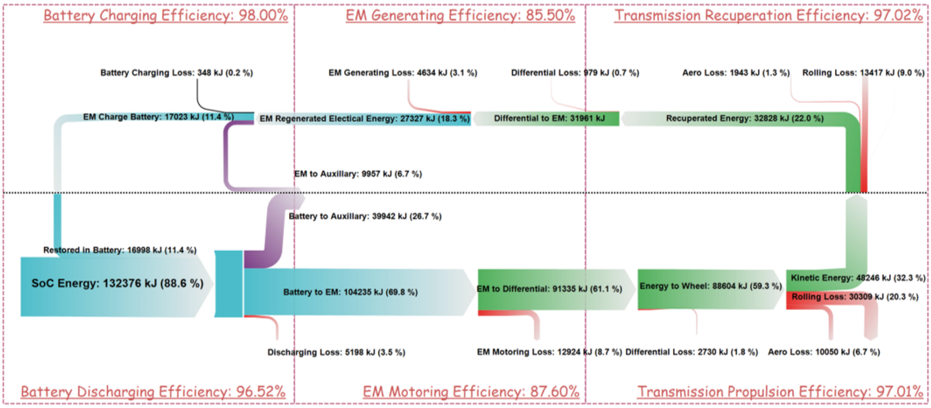

Figure 1.4: *Sankey diagram of a typical BEV powertrain.*

1.2 Objectives

Improving powertrain energy efficiency should not be viewed solely as improving the efficiency of each individual powertrain component, since the overall powertrain efficiency is determined not only by the efficiencies of the individual components but, more importantly, by how these components interact with each other under different operating conditions. Therefore, this thesis aims to explore solutions for improving BEV powertrain energy efficiency through a systematic approach, focusing primarily on three research directions.

The first research direction focuses on powertrain architecture innovation. Rather than treating the powertrain as a fixed assembly of components, it is considered as a reconfigurable system whose structure and interaction mechanisms can be redesigned to introduce additional operational degrees of freedom. By enabling more flexible operating conditions for key components, novel architectural concepts have the potential to improve system-level energy efficiency under varying driving conditions. Accordingly, the first objective of this thesis is to investigate alternative powertrain architectures that expand the design space for efficiency-oriented optimization.

While architectural solutions can provide substantial efficiency benefits, they may also increase system complexity and implementation cost. As a complementary pathway, efficiency improvements can be achieved through advanced control strategies that enhance the utilization of powertrain hardware. Such strategies may operate at multiple levels of the control hierarchy, from high-level supervisory energy management to low-level electric drive control. The second objective of this thesis is therefore to develop and evaluate efficiency-oriented powertrain control methodologies that improve energy utilization without requiring fundamental hardware modifications.

In addition to architecture and control, thermal management fundamentally influence powertrain energy efficiency. Temperature-dependent powertrain component losses and the energy consumption of thermal management auxiliaries jointly determine the overall energy efficiency. However, these aspects are often addressed independently. The third objective of this thesis is to develop integrated thermal management strategies that coordinate component temperatures across the powertrain, aiming to minimize total energy consumption while ensuring safe and reliable operation.

Together, these objectives establish a multi-domain framework for improving BEV powertrain energy efficiency, integrating architectural design, control strategy development, and thermal management into a coherent system-level optimization approach.

1.3 Research gaps and contributions

While extensive research has been conducted on improving BEV powertrain efficiency through both component-level and system-level approaches, further potential remains to be explored. Following the three research directions introduced above, the contributions of this thesis are positioned with respect to the limitations identified in previous research.

The main contributions of the thesis are summarized as follows:

- **Dual-motor powertrain with independent disconnect functionality and configuration-aware motor design.**

  Extensive research on multi-motor powertrain architectures has demonstrated the potential for improving energy efficiency through flexible torque distribution among the electric motors [15–18]. Among these architectures, dual motor powertrains with electric motors placed in the front and rear axles are widely adopted owing to their all-wheel-drive capability and fault tolerance [19–21]. However, when permanent magnet synchronous motors (PMSMs) are employed, an inactive or lightly loaded EDU can still generate considerable no-load losses, particularly at high rotational speeds [22, 23]. Previous studies have therefore suggested a single disconnect clutch to mechanically decouple one EDU, demonstrating meaningful reductions in drive-cycle energy consumption [24–26]. Nevertheless, the potential of independently disconnecting both front and rear EDUs, particularly when the motors exhibit differentiated efficiency characteristics, has received less attention. Moreover, the transient energy losses associated with EDU engagement and disengagement transitions are often neglected in the energy management strategy (EMS), despite their importance for avoiding excessive mode shifting. Therefore, one of the contributions of this thesis is the investigation of the dual-motor powertrain where the front and rear EDUs can be independently connected or disconnected with two sets of clutches. To fully exploit this additional operational flexibility, an EMS is developed that jointly considers optimal torque allocation, operating-mode selection, and the transient energy losses associated with mode shifting. This enables the efficiency characteristics of the individual EDUs to be effectively utilized under different driving conditions.

The work is further extended toward configuration-aware motor design. In most existing multi-motor powertrain studies, the EMS is derived from predefined motor or EDU efficiency maps, effectively treating the motor characteristics as fixed inputs. Conversely, motor design optimization is often performed using predefined operating points obtained from vehicle-level analysis [27, 28]. However, these two problems are inherently coupled in multi-motor powertrains: the EMS determines the operating-point distribution of each motor, while the motor design and its resulting efficiency characteristics directly influence the optimization of the EMS. Although several powertrain and EMS co-optimization approaches have been proposed, they commonly rely on scaled or parameterized reference motor efficiency maps, which are less suitable for detailed motor design optimization because of the highly nonlinear relationship between motor geometry and losses [29–33]. Hence, another contribution of this thesis is to bridge the gap between vehicle-level powertrain operation and motor design optimization by jointly optimizing the front and rear motor designs together with the corresponding EMS using fast and sufficiently accurate prediction of the motor and complete EDU loss maps associated with detailed motor geometric designs, rather than scaled reference efficiency maps.

- **Eco-driving combined with powertrain free-coasting with disconnect functionality.**

  Eco-driving has been widely investigated as an energy-efficient control approach by optimizing the vehicle speed trajectory according to predictive information such as road gradient and traffic conditions [34, 35]. Free-coasting has also demonstrated energy-saving potential in internal combustion engine vehicles (ICEVs) by allowing the vehicle to utilize its kinetic energy while avoiding powertrain losses, namely through the pulse-and-glide strategy [36, 37]. However, disconnect functionality in BEVs has predominantly been investigated for dual-motor powertrains, where one EDU is disconnected while the other remains active to provide the required traction torque. Consequently, the potential of completely disconnecting the powertrain in a BEV has received comparatively limited attention, since conventional speed-following operation generally requires the propulsion system to remain continuously available.

Therefore, another contribution of this thesis is the integration of eco-driving with disconnect functionality in a BEV with a single-motor powertrain. The vehicle speed trajectory and clutch state are jointly optimized, allowing periods of complete powertrain disconnect and free-coasting to be intentionally introduced when energetically beneficial.

- **Optimized DC-link voltage control in adjustable DC-link voltage powertrains.**

  In conventional BEV powertrains, the DC-link voltage is closely coupled to the battery terminal voltage, while the resulting powertrain energy efficiency is strongly affected by the vehicle operating condition and battery setup [38, 39]. Adjustable DC-link voltage has therefore been proposed as a means of improving powertrain efficiency by adapting the inverter supply voltage according to the operating condition [40–42]. However, previous studies often simplify or neglect the additional losses introduced by the DC–DC converter and commonly assume a fixed battery terminal voltage, despite its variation with load and state of charge. These assumptions can affect the estimated system-level benefit of adjustable DC-link operation.

  Therefore, one contribution of this thesis is the development of a system-level DC-link voltage optimization approach that minimizes the combined losses of the battery, DC–DC converter, inverter, and electric motor while accounting for battery terminal-voltage variation over the drive cycle. The influence of semiconductor technology is further investigated by comparing adjustable DC-link voltage powertrains based on silicon (Si) insulated-gate bipolar transistors (IGBTs) and silicon carbide (SiC) metal–oxide–semiconductor field-effect transistors (MOSFETs), since their different switching and conduction loss characteristics can significantly affect the achievable energy-saving potential.

  The work is further extended toward high-voltage battery architectures as battery systems of 800 V and above are increasingly adopted [43–45]. However, increasing the battery voltage does not necessarily improve powertrain efficiency under all operating conditions. While reduced current can decrease conduction and motor copper losses at high load, increased DC-link voltage can lead to higher power-electronics switching losses, particularly under low-load operation [46]. Most previous adjustable DC-link studies have focused on lower-voltage battery systems using boost conversion, while the potential of high-voltage systems employing buck conversion remains less explored. Hence, another contribution of this thesis is a systematic comparison of lower-voltage battery systems using boost conversion and higher-voltage battery systems using buck conversion, where the DC-link voltage is optimized according to the operating condition. This provides an indication of how battery voltage level and adjustable DC-link voltage powertrain configuration should be selected from an overall energy-efficiency perspective.

- **Powertrain torque modulation control.**

  EDU efficiency is generally lower in low-torque operating regions, and torque modulation has been proposed as a means of shifting the motor operation toward more efficient torque levels while maintaining the required average torque [47–49]. However, existing strategies are mainly optimized based on motor and inverter efficiency characteristics, while the resulting changes in battery and transmission losses are often neglected. Consequently, a torque modulation strategy that improves motor-drive efficiency does not necessarily minimize the overall powertrain energy loss.

  Therefore, one contribution of this thesis is the development of a torque-modulation strategy from an overall powertrain perspective, where the combined losses of the battery, inverter, electric motor, and transmission are considered when determining the optimal modulation parameters. This enables the efficiency gains obtained from shifting the motor toward more favorable operating regions to be balanced against the additional losses introduced elsewhere in the powertrain.

  Another contribution is the extension of torque modulation to dual-motor powertrains. Previous studies have primarily focused on single-motor applications, while the additional torque-distribution freedom available in dual-motor powertrains has received limited attention. In this thesis, torque modulation is coordinated between the front and rear motors, allowing both motors to exploit more efficient operating regions under low torque demand. Complementary modulation between the two motors is further introduced to reduce the resulting total powertrain torque fluctuation, thereby improving driver comfort while retaining the energy-efficiency benefit of torque modulation.

- **Integrated powertrain energy-oriented thermal management.**

  The energy efficiency of electric powertrains is strongly influenced by component operating temperatures. Temperature variations affect motor copper and iron losses, inverter conduction and switching losses, and transmission losses through the temperature-dependent viscosity of the lubricating oil [50–56]. Conventional thermal management strategies are primarily designed to maintain component temperatures within safe limits and often rely on rule-based control of cooling auxiliaries such as pumps and fans [57, 58]. Previous energy-oriented studies have either considered temperature-dependent powertrain efficiency [59–61] or focused on reducing cooling-system energy consumption [62–64]. More recent studies have begun to combine these objectives [65–69].

  However, most existing studies focus primarily on the inverter and electric motor, while the temperature-dependent losses of the transmission are less frequently included. This becomes increasingly important with the development of highly integrated EDUs, where the inverter, motor, and transmission are closely packaged and thermally coupled through coolant and oil circuits. Therefore, one contribution of this thesis is the development of an integrated energy-oriented thermal management strategy that jointly minimizes temperature-dependent powertrain losses and cooling-system auxiliary energy consumption while maintaining the component temperatures within their thermal limits.

2 Background

This chapter presents the theoretical foundations underpinning the powertrain efficiency analyses conducted in this thesis.

2.1 Powertrain losses

2.1.1 Battery

The electrochemical behavior of the battery can be represented using an equivalent circuit [70]. For applications concerned primarily with energy consumption analysis rather than detailed transient voltage dynamics, a simplified model consisting of an open-circuit voltage source (OCV) V_{oc} in series with an internal ohmic resistance R_0 provides sufficient accuracy, capturing the dominant resistive losses and terminal voltage behavior [71], as depicted in Figure 2.1a. The OCV and internal resistance are parameterized as functions of the state of charge (SoC) and temperature, with separate characterization for charge and discharge operation.

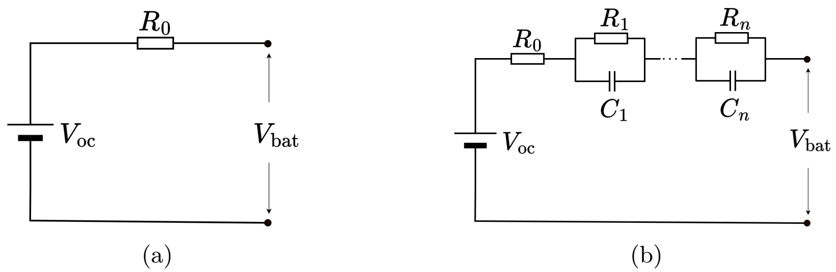

Figure 2.1: *Battery equivalent circuit models. (a) Simplified model (b) Thevenin equivalent circuit model.*

The SoC quantifies the remaining stored energy relative to the fully charged condition and is computed by integrating the battery current over time as

$$\mathrm{SoC}(t) = \mathrm{SoC}(t_0) - \frac{1}{C_{\mathrm{bat}}} \int_{t_0}^{t} I_{\mathrm{bat}}(\tau)\, d\tau, \tag{2.1}$$

where $\mathrm{SoC}(t_0)$ is the initial state of charge, C_{bat} is the nominal battery capacity, and I_{bat} is the battery current. In the simplified model, the terminal voltage is expressed as

$$V_{\mathrm{bat}} = V_{\mathrm{oc}} - I_{\mathrm{bat}} R_0, \tag{2.2}$$

and the corresponding resistive power loss can be expressed as

$$P_{\mathrm{loss,bat}} = I_{\mathrm{bat}}^2 R_0. \tag{2.3}$$

When the battery is subjected to rapidly varying load conditions, polarization effects introduce dynamic voltage behavior that cannot be captured by a purely resistive model. In such cases, additional RC branches can be incorporated to form a Thevenin equivalent circuit, as depicted in Figure 2.1b [72–75].

2.1.2 Power electronics

Switched-mode power converters regulate the flow of energy between the battery, electric motor, and other electrical subsystems. The DC–DC converter adapts voltage levels between subsystems, while the inverter converts the battery DC voltage into three-phase AC voltage for motor operation. Two semiconductor technologies are considered in this thesis: the Si-IGBT and the SiC-MOSFET. IGBTs are minority-carrier devices with relatively low on-state voltage at high currents, but exhibit turn-off tail currents and require an external antiparallel diode for reverse conduction, resulting in additional switching and reverse recovery losses. MOSFETs are majority-carrier devices with faster switching transitions, lower switching losses, and higher blocking voltage [76, 77]. These characteristics make SiC MOSFETs particularly attractive for modern high-voltage BEV applications, enabling higher efficiency, improved thermal capability, and higher switching frequency operation, despite their higher cost.

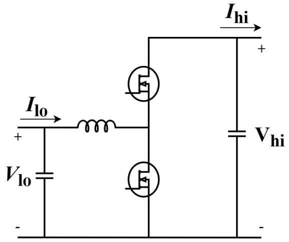

Figure 2.2: *Non-isolated bidirectional buck–boost converter scheme.*

A bidirectional non-isolated buck–boost DC–DC converter, shown in Figure 2.2, can serve as an intermediary between the battery and the DC-link [40, 78, 79]. This topology supports bidirectional energy flow, accommodating both propulsion and regenerative braking operation. The duty cycle d governing the switching operation is defined as

$$d = \begin{cases} \dfrac{V_{\mathrm{lo}}}{V_{\mathrm{hi}}}, & \text{buck operation} \\ 1 - \dfrac{V_{\mathrm{lo}}}{V_{\mathrm{hi}}}, & \text{boost operation} \end{cases} \tag{2.4}$$

where V_{lo} and V_{hi} denote the low- and high-side voltages, respectively. When the battery is connected to the low-voltage side and the DC-link to the high-voltage side (boost configuration), the converter operates in boost mode during propulsion to raise the battery voltage to higher DC-link voltage level, and in buck mode during regenerative braking to transfer energy back to the battery. Conversely, in the buck configuration, the battery is located on the high-voltage side and the power flow directions are reversed accordingly.

The IGBT-based DC–DC converter comprises the switching and conduction losses of the IGBT transistor and its antiparallel diode during the operation as

$$\begin{aligned} P_{\mathrm{DCDC,loss}} = {} & \left(V_{ce0} I_{\mathrm{lo}} + r_{ce} I_{\mathrm{lo}}^2\right) d + \left(V_{d0} I_{\mathrm{lo}} + r_d I_{\mathrm{lo}}^2\right)(1-d) \\ & + E_{sw} f_{sw} \left(\frac{I_{\mathrm{lo}}}{I_{\mathrm{ref}}}\right)^{K_{it}} \left(\frac{V_{\mathrm{hi}}}{V_{\mathrm{ref}}}\right)^{K_{vt}} + E_{rec} f_{sw} \left(\frac{I_{\mathrm{lo}}}{I_{\mathrm{ref}}}\right)^{K_{id}} \left(\frac{V_{\mathrm{hi}}}{V_{\mathrm{ref}}}\right)^{K_{vd}}, \end{aligned} \tag{2.5}$$

where V_{ce0} is the IGBT forward voltage drop, r_{ce} is the IGBT on-state resistance, V_{d0} is the diode forward voltage drop, r_d is the diode on-state resistance, E_{sw} is the transistor switching energy, f_{sw} is the switching frequency, I_{ref} and V_{ref} are reference current and voltage values used for switching loss linearization, E_{rec} is the diode reverse recovery energy, and K_{it}, K_{vt}, K_{id}, K_{vd} are exponents describing the current and voltage dependence of transistor and diode switching energy, respectively. Losses associated with gate driver and snubber circuits, as well as capacitive and inductive parasitics, are considered negligible and are therefore omitted [80].

For MOSFET-based converters, the reverse conduction capability of the MOSFET channel enables synchronous operation, in which both switches conduct alternately [81]. If the voltage drop across the MOSFET on-state resistance r_{ds} remains below the body diode forward voltage V_{sd0}, i.e., $I_{\mathrm{lo}} \cdot r_{ds} < V_{sd0}$, the reverse current flows entirely through the transistor channel rather than the body diode [82–84]. Under this condition, diode conduction and reverse recovery losses are avoided. The total losses of a MOSFET-based DC–DC converter are therefore expressed as

$$P_{\mathrm{DCDC,loss}} = r_{ds} I_{\mathrm{lo}}^2 + 2 E_{sw} f_{sw} \left(\frac{I_{\mathrm{lo}}}{I_{\mathrm{ref}}}\right)^{K_{it}} \left(\frac{V_{\mathrm{hi}}}{V_{\mathrm{ref}}}\right)^{K_{vt}}. \tag{2.6}$$

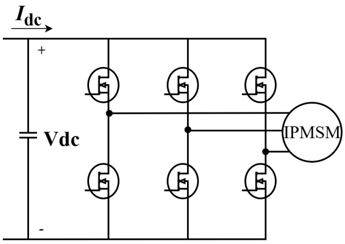

Figure 2.3: *Three phase inverter scheme.*

Figure 2.3 illustrates the structure of a three-phase inverter composed of three legs, each consisting of a half-bridge configuration with two switches. By employing space vector pulse-width modulation (SVPWM), improved DC-link voltage utilization can be achieved compared to conventional sinusoidal PWM [85]. Under ideal conditions, the amplitude of the AC phase voltage V_{ac} depends on the DC-link voltage V_{dc} and the modulation index m_a as

$$V_{\mathrm{ac}} = \frac{m_a V_{\mathrm{dc}}}{\sqrt{3}}. \tag{2.7}$$

For an IGBT-based inverter, the total losses consist of the conduction and switching contributions from both the IGBT and its antiparallel diode, and can be expressed analytically as follows [86, 87]

$$\begin{aligned} P_{\mathrm{inv,loss}} &= 6V_{ce0}I_{\mathrm{o}}\left(\frac{1}{2\pi}+\frac{m_a\cos\varphi}{8}\right)+6r_{ce}I_{\mathrm{o}}^2\left(\frac{1}{8}+\frac{m_a\cos\varphi}{3\pi}\right) \\ &+6V_{d0}I_{\mathrm{o}}\left(\frac{1}{2\pi}-\frac{m_a\cos\varphi}{8}\right)+6r_dI_{\mathrm{o}}^2\left(\frac{1}{8}-\frac{m_a\cos\varphi}{3\pi}\right) \\ &+6E_{sw}f_{sw}\left(\frac{I_{\mathrm{o}}}{\pi I_{\mathrm{ref}}}\right)^{K_{it}}\left(\frac{V_{\mathrm{dc}}}{V_{\mathrm{ref}}}\right)^{K_{vt}}+6E_{\mathrm{rec}}f_{sw}\left(\frac{I_{\mathrm{o}}}{\pi I_{\mathrm{ref}}}\right)^{K_{id}}\left(\frac{V_{\mathrm{dc}}}{V_{\mathrm{ref}}}\right)^{K_{vd}}, \end{aligned} \tag{2.8}$$

where I_{o} is the amplitude of AC phase current and $\cos\varphi$ is the power factor.

For a MOSFET-based inverter, when the reverse conduction capability of the MOSFET channel is utilized and diode conduction is avoided, the inverter losses consist only of MOSFET conduction and switching losses. Under this assumption, the total losses are given by

$$P_{\mathrm{inv,loss}} = \frac{3}{2}{I_{\mathrm{o}}}^2 r_{ds}+6E_{sw}f_{sw}\left(\frac{I_{\mathrm{o}}}{\pi I_{\mathrm{ref}}}\right)^{K_{it}}\left(\frac{V_{\mathrm{dc}}}{V_{\mathrm{ref}}}\right)^{K_{vt}}. \tag{2.9}$$

2.1.3 Electric motor

This thesis focuses exclusively on the interior permanent magnet synchronous motor (IPMSM) due to its superior power density and efficiency, making it a dominant choice in the current BEV market [88, 89]. In synchronous machines, the d–q axis representation in the rotor reference frame provides a physically intuitive and mathematically convenient description of the motor dynamics. The direct axis (d-axis) corresponds to the radial axis intersecting the centerline of the permanent magnets and represents the direction of the magnetic flux produced by the magnets. The quadrature axis (q-axis) is positioned 90 electrical degrees ahead of the d-axis and lies between two magnetic poles. Figure 2.4 illustrates the equivalent electrical circuit model of the PMSM in the d–q reference frame.

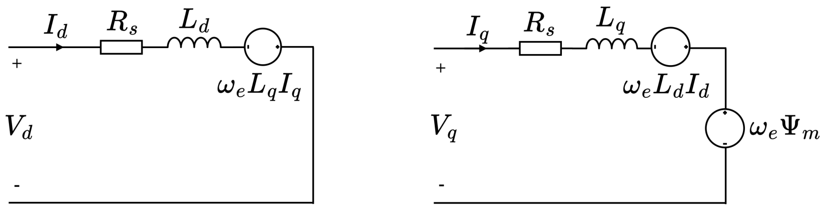

Figure 2.4: *PMSM equivalent electric circuit model.*

The steady-state stator voltage equations in the d–q reference frame are expressed as

$$V_d = R_s I_d - \omega_e L_q I_q, \tag{2.10}$$
$$V_q = R_s I_q + \omega_e L_d I_d + \omega_e \Psi_m, \tag{2.11}$$

where V_d and V_q are the d- and q-axis stator voltages, R_s is the stator resistance, L_d and L_q are the d- and q-axis inductances, Ψ_m is the permanent magnet flux linkage, and $\omega_e = n_p \omega_r$ is the electrical angular speed, with ω_r being the mechanical rotor speed and n_p the number of pole pairs.

For salient machines such as the IPMSM ($L_d \neq L_q$), the electromagnetic torque consists of both magnet torque and reluctance torque as

$$T_e = \frac{3}{2} n_p \left(\Psi_m I_q + (L_d - L_q) I_d I_q \right). \tag{2.12}$$

For IPMSMs, the maximum torque per ampere (MTPA) control strategy (as illustrated in Figure 2.5) is widely adopted in the constant torque region to determine the optimal current components I_d and I_q that minimize the stator current magnitude and thereby reduce copper losses, while respecting the DC-link voltage limit V_{dc} [90]. The MTPA problem can be formulated as

$$\min_{I_d, I_q} \quad \sqrt{I_d^2 + I_q^2}, \tag{2.13}$$

$$\text{s.t.} \quad T_e(I_d, I_q) = T^\star, \tag{2.14}$$

$$\sqrt{V_d^2(I_d, I_q, \omega_e) + V_q^2(I_d, I_q, \omega_e)} \leq \frac{V_{\mathrm{dc}}}{\sqrt{3}}, \tag{2.15}$$

where $T^\star$ is the commanded torque. The voltage limit, typically represented as an ellipse in the I_d–I_q plane, defines the maximum allowable stator voltage magnitude. The base speed marks the highest speed at which the motor can maintain the MTPA strategy while satisfying the voltage constraint. When operating beyond the base speed, a field-weakening strategy is employed by injecting negative I_d to reduce the effective air-gap flux and limit the back electromotive force. This enables operation at higher speeds within the voltage constraint but leads to increased losses and reduced torque capability, since the motor operates outside the optimal MTPA region. At even higher speeds, the control objective transitions to maximum torque per voltage (MTPV), where the current trajectory is selected to maximize torque under the active voltage constraint. In this region, the voltage limit becomes the dominant constraint, and the operating point moves along the boundary of the voltage ellipse.

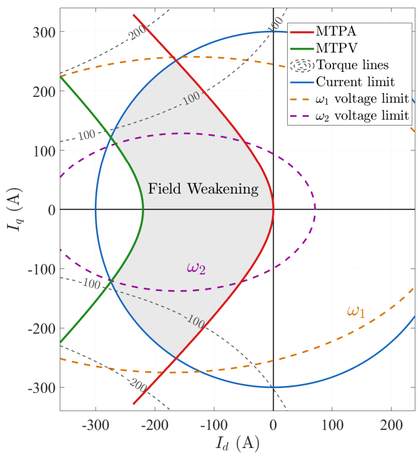

Figure 2.5: *Illustration of MTPA control strategy.*

The total losses in a PMSM primarily consist of copper losses, iron losses, and mechanical losses. Copper losses arise from the stator winding resistance and are expressed as

$$P_{\mathrm{cu}} = 3R_s I_{s,\mathrm{rms}}^2 = \frac{3}{2} R_s (I_d^2 + I_q^2), \tag{2.16}$$

where $I_{s,\mathrm{rms}}$ is the RMS stator phase current. The resistance R_s can be further broken down into R_{dc} and R_{ac} to account for DC and AC copper losses. The DC resistance R_{dc} represents the ohmic resistance of the conductor. In contrast, the AC resistance R_{ac} accounts for additional frequency-dependent losses caused by non-uniform current distribution within the conductors. These losses arise primarily due to the skin effect and the proximity effect [91]. The ratio $R_{\mathrm{ac}}/R_{\mathrm{dc}}$ increases with electrical frequency and is therefore strongly dependent on motor speed, current excitation, and winding geometry [51]. The DC resistance is temperature dependent due to the variation of copper resistivity with temperature and can be expressed as

$$R_{\mathrm{dc}}(T_{\mathrm{w}}) = R_{\mathrm{dc}}(T_{\mathrm{ref}}) \left[1 + \alpha \left(T_{\mathrm{w}} - T_{\mathrm{ref}}\right)\right], \tag{2.17}$$

where T_{w} is the winding temperature, T_{ref} is the reference temperature, and α is the temperature coefficient of resistivity for copper. The AC resistance is also temperature dependent, since it is influenced by conductor resistivity and the associated electromagnetic field distribution. Using the ratio between AC and DC resistance at the reference temperature, the AC resistance can be expressed as [92]

$$R_{\mathrm{ac}}(T_{\mathrm{w}}) = R_{\mathrm{dc}}(T_{\mathrm{w}}) \, \frac{\left(\dfrac{R_{\mathrm{ac}}(T_{\mathrm{ref}})}{R_{\mathrm{dc}}(T_{\mathrm{ref}})} - 1\right)}{\left(1 + \alpha(T_{\mathrm{w}} - T_{\mathrm{ref}})\right)^{\beta+1}}, \tag{2.18}$$

where β is an empirical coefficient.

Iron losses, also referred to as core losses, originate mainly from magnetic hysteresis and induced eddy currents in the ferromagnetic materials of the stator and rotor. Under sinusoidal excitation, the average iron loss can be described using the classical Steinmetz formulation as

$$P_{\mathrm{fe}} = k_h f \hat{B}^n + k_c f^2 \hat{B}^2, \tag{2.19}$$

where k_h is the hysteresis coefficient, k_c is the eddy current coefficient, f is the electrical frequency, $\hat{B}$ is the peak magnetic flux density, and n depends on the material properties and operating conditions. In inverter-fed PMSMs, the applied voltage and resulting flux waveforms are not purely sinusoidal but contain harmonics due to switching effects. These harmonics introduce additional core losses that are difficult to predict analytically [93]. As a consequence, iron losses estimated using sinusoidal-based models often require a correction factor (typically in the range of 1.5–2) to account for excess harmonic-induced losses [94].

Mechanical losses consist of friction losses and windage losses. Friction losses mainly originate from the rotor bearings and their lubrication system, where mechanical contact and viscous effects dissipate energy. Windage losses arise from aerodynamic drag caused by the interaction between the rotating rotor and the surrounding air (or cooling medium). For modeling purposes, the friction losses are categorized as part of the transmission losses and the windage losses are empirically correlated with rotor speed using an exponential function.

2.1.4 Transmission

The transmission reduces the rotational speed of the motor while amplifying its torque output, ensuring that the speed and torque delivered to the wheels meet the vehicle's operational requirements. For BEV applications, this is typically achieved through a fixed gear reduction stage. During operation, the transmission introduces several loss mechanisms, including gear meshing losses, bearing losses, and churning losses [95–98]. Gear meshing losses consist of sliding and rolling friction between gear teeth and are primarily load-dependent. Churning losses arise from the interaction between rotating components and the lubricating oil and are mainly speed-dependent. Bearing losses are influenced by both transmitted load and rotational speed. Consequently, the total transmission loss is a function of both rotational speed and transmitted torque. In addition, the transmission is temperature sensitive due to the temperature-dependent viscosity of the lubricating oil. Variations in oil temperature affect churning losses and frictional behavior, thereby influencing the overall transmission efficiency.

Compared with the electric motor and inverter, the transmission efficiency is generally less sensitive to variations in operating speed and torque and remains relatively stable over a wide operating range, allowing for simplification using a constant efficiency value, as is common practice in mathematical and vehicle-level studies [99, 100]. When more detailed transmission simulation or experimental data are available, the losses can instead be represented using efficiency or loss maps as functions of rotational speed and torque. For higher-fidelity models, oil temperature can also be included as an additional dependency to account for the influence of lubricant viscosity on churning and friction losses.

2.1.5 Drive-cycle analysis

A drive cycle prescribes the vehicle speed as a function of time and is used to represent specific driving conditions in a repeatable and standardized manner. Different drive cycles are designed to capture various driving patterns, including acceleration, deceleration, cruising, and idling, in order to evaluate how efficiently a BEV utilizes its available energy during operation.

One of the most widely adopted legislative drive cycles is the Worldwide Harmonized

Light Vehicles Test Cycle (WLTC), shown in Figure 2.6. The WLTC spans approximately 1800 s and consists of low, medium, high, and extra-high speed phases, thereby covering a broad range of operating conditions relevant to modern passenger vehicles [101]. In addition to legislative cycles, real-world driving cycles derived from logged vehicle data can be used to more directly represent case-specific vehicle usage [102]. Such cycles capture the influence of traffic conditions, road gradients, driver behavior, and ambient environment, thereby providing a complementary perspective to standardized testing procedures.

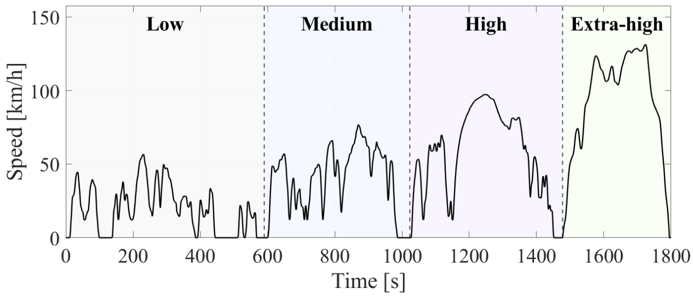

Figure 2.6: *Vehicle speed profile of WLTC.*

As illustrated in Figure 2.7, the powertrain must generate tractive force at the wheels to overcome aerodynamic drag, rolling resistance, road gradient force, and acceleration. The longitudinal force balance can be expressed as

$$\frac{T_{\text{trac}}}{R_r} = mg\sin(\theta) + \frac{1}{2}\rho_a C_d A v^2 + C_r mg\cos(\theta) + (m + m_i)\dot{v}, \tag{2.20}$$

where T_{trac} is the required traction torque at wheels, R_r is the effective tire rolling radius, m is the vehicle mass, g is gravitational acceleration, θ is the road gradient, ρ_a is air density, C_d is the aerodynamic drag coefficient, A is the frontal area, v is vehicle speed, C_r is the rolling resistance coefficient, and m_i represents the equivalent rotational inertia.

Given a prescribed speed trajectory $v(t)$ from a drive cycle, (2.20) determines the required traction torque and power, which form the input to the subsequent powertrain loss models.

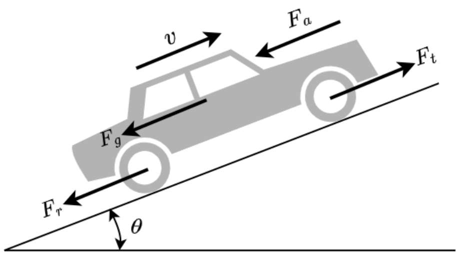

Figure 2.7: *Forces acting on a vehicle in the longitudinal direction.*

2.2 Control strategy

In electrified powertrains, the supervisory control layer is responsible for coordinating multiple subsystems, including electric motors, inverters, battery systems, transmissions, and thermal circuits. As the number of actuators and degrees of freedom increases, the control problem becomes increasingly complex.

The primary objective of the powertrain control is to satisfy the driver torque demand while ensuring that all operational constraints are respected. These constraints arise from actuator limits (e.g., maximum motor torque and current limits), battery-related restrictions such as SoC and voltage boundaries, as well as thermal limitations of critical components including electric motors, inverters, and cooling circuits. Beyond guaranteeing feasibility and safe operation, proper energy and thermal management strategies aim to optimize overall system performance, particularly in terms of energy efficiency.

From a methodological standpoint, powertrain control strategies can generally be classified into two main categories: rule-based (heuristic) strategy and optimization-based strategy.

2.2.1 Rule-based strategy

Rule-based strategies rely on predefined control rules derived from engineering insight, experimental observations, and simplified system analysis. Two common realizations are map-based and state-machine-based strategies. In map-based approaches, optimal or near-optimal control actions are precomputed offline and stored in multi-dimensional look-up tables (LUTs) [103, 104]. Finite state machines are widely employed to describe distinct operating modes of the powertrain. Each state corresponds to a predefined configuration of component operation, and transitions between states are triggered when specified logical conditions or threshold values are met [105]. These thresholds are typically determined through calibration processes that consider efficiency targets, driveability requirements, and component protection constraints.

These approaches are widely adopted in industrial applications due to their transparency, robustness, and ease of real-time implementation. However, their performance is highly dependent on calibration quality, and optimality cannot be guaranteed under varying operating conditions.

2.2.2 Optimization-based strategy

Optimization-based strategies formulate the supervisory control problem as a constrained optimal control problem. The controller determines the control inputs by minimizing a predefined objective function subject to system dynamics and operational constraints. The objective function is typically constructed to reflect overall powertrain energy efficiency and may include terms related to powertrain losses and penalties on actuator usage.

The optimization problem can be formulated in discrete time as follows. Consider a nonlinear system described by

$$x_{k+1} = f_k(x_k, u_k), \tag{2.21}$$

where $x_k \in X_k$ denotes the system state at time step k and $u_k \in U_k$ represents the control input. The index $k = 0, 1, \ldots, N-1$ defines the finite horizon. Both the state and control variables are subject to operational constraints.

The performance objective over a horizon of length N is expressed through a cumulative cost function

$$J(x_0, u) = L_N(x_N) + \sum_{k=0}^{N-1} L_k(x_k, u_k), \tag{2.22}$$

where $L_k(x_k, u_k)$ represents the stage cost and $L_N(x_N)$ is a terminal cost. The corresponding optimal control problem is formulated as

$$\min_{u} \; J(x_0, u), \tag{2.23}$$

subject to the system dynamics and state/input constraints. The stage cost typically captures instantaneous power losses and efficiency penalties, while the terminal cost may enforce desired end conditions.

Optimization-based strategies can be divided into offline global optimization methods and online predictive optimization methods. The former category includes approaches such as dynamic programming (DP), which require full knowledge of the drive cycle and are primarily used for benchmarking purposes or for assessing the maximum achievable performance potential of a specific powertrain architecture. The latter includes real-time implementable methods such as model predictive control (MPC), which rely on short-term predictions and receding-horizon optimization.

Dynamic programming: DP is a global optimization technique founded on Bellman's principle of optimality [106]. When the entire driving profile is known in advance, DP computes the globally optimal control sequence over the full horizon.

The method proceeds by defining the cost-to-go function and solving the problem recursively backward. The Bellman recursion is given by

$$J_k(x_k) = \min_{u_k \in U_k} \left[L_k(x_k, u_k) + J_{k+1}(f_k(x_k, u_k)) \right], \tag{2.24}$$

with terminal condition

$$J_N(x_N) = L_N(x_N). \tag{2.25}$$

By discretizing the state and control spaces and solving from $k = N - 1$ down to $k = 0$, DP guarantees global optimality under the chosen discretization. This property makes it particularly suitable for evaluating the theoretical efficiency and thermal performance limits of different powertrain configurations. However, the computational burden increases exponentially with the dimension of the state space, a phenomenon commonly referred to as the curse of dimensionality. Consequently, DP is primarily used offline as a benchmarking tool rather than for direct real-time implementation.

Model predictive control: MPC is an online optimization strategy that repeatedly solves a finite-horizon optimal control problem at each sampling instant [107]. At step k, a sequence of future control inputs is obtained by minimizing

$$\min_{u_{k:k+N-1}} \sum_{i=k}^{k+N-1} L_i(x_i, u_i) + L_{k+N}(x_{k+N}), \tag{2.26}$$

subject to system dynamics and constraints over a prediction horizon of length N. Only the first control action of the optimized sequence is applied to the system. At the next time step, the optimization is repeated with updated state information, following the receding-horizon principle.

Unlike offline global optimization, MPC does not require full knowledge of the entire drive cycle. Instead, it relies on short-term predictions, such as velocity forecasts or route information, and computes locally optimal solutions over the prediction horizon. MPC explicitly handles state and input constraints and can incorporate predictive thermal behavior, making it well suited for integrated energy and thermal management. With appropriate horizon selection and model simplification, MPC can be implemented in real time for practical automotive applications.

3 Dual-Motor Powertrain Utilizing Disconnect Functionality

This chapter is based on Papers I and VI. The objective of this chapter is to investigate the energy-saving potential of dual-motor powertrain configurations incorporating disconnect functionality enabled by dog clutches. Furthermore, the chapter explores how the front and rear motor designs can be optimally tailored to fully exploit the additional degrees of freedom introduced by the disconnect functionality.

3.1 Powertrain configuration

A dual-motor powertrain with a front and rear axle independently driven (FRID) configuration can incorporate disconnect functionality via clutches placed in the front and rear axles. This configuration is referred to as the adaptive front and rear axle independently driven (AFRID) powertrain, as illustrated in Figure 3.1. In this configuration, two EDUs are installed on the front and rear axles, respectively, and each EDU can be mechanically connected to or disconnected from its corresponding axle through the clutch.

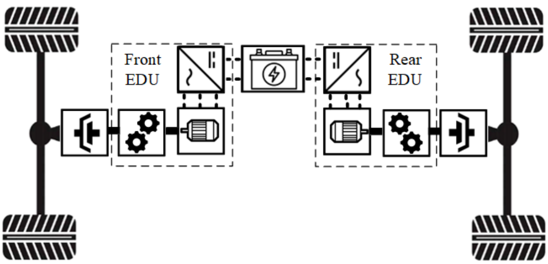

Figure 3.1: *AFRID powertrain configuration with front- and rear-axle EDUs including clutches. Each EDU consists of a transmission, a three-phase motor, and an inverter.*

The disconnect functionality allows an inactive EDU to be completely decoupled from the powertrain, thereby eliminating no-load losses (illustrated in Figure 3.2) associated with free-spinning operation when torque is not required. These losses mainly originate from inverter and PMSM losses caused by reactive current required to counteract the back electromotive force in the field-weakening region [22], as well as mechanical friction in the rotating components of the EDU.

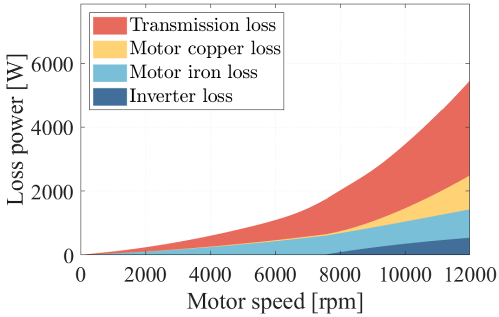

Figure 3.2: *EDU no-load losses.*

Depending on the engagement states of the EDUs and the clutches, the AFRID powertrain can operate in three distinct driving modes: front-wheel drive (FWD), rear-wheel drive (RWD), and all-wheel drive (AWD).

3.2 Operating principle

3.2.1 Disconnect functionality

Owing to its positive mechanical locking mechanism, the dog clutch contributes negligible parasitic losses during steady-state operation (approximately 5 W) and only minimal energy consumption during actuation (approximately 16 kJ). The structure and engagement process of the dog clutch are illustrated in Figure 3.3.

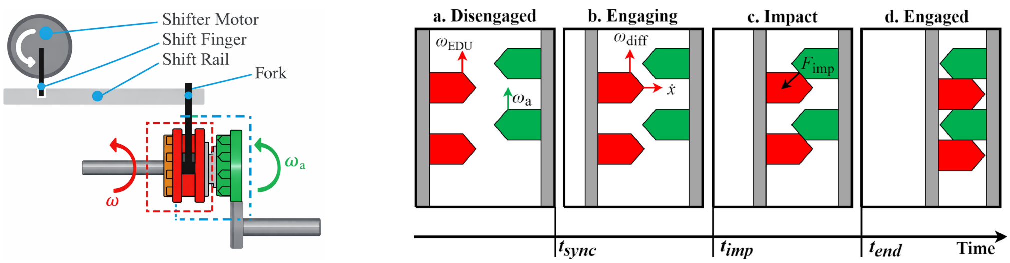

(a) (b)

Figure 3.3: *Illustration of the dog clutch. (a) Structure. (b) Engagement process.*

During the engagement process, the rotational speed of the EDU output shaft, ω, is synchronized with the drive axle speed, ω_a, prior to actuation of the clutch by the shifter fork. Conversely, after clutch disengagement, the EDU rotational speed is actively reduced to zero. This braking process enables partial recovery of the rotational kinetic energy while preventing subsequent free-spinning losses.

The EDU rotational speed is regulated by a speed-control torque, T_c, which is positive during synchronization and negative during braking to counteract both inertial effects and friction as

$$T_c = J_E \frac{d\omega}{dt} + T_{fr}(\omega), \tag{3.1}$$

where J_E denotes the EDU rotational inertia and T_{fr} is the speed-dependent frictional torque. The speed control process during clutch engagement and disengagement introduces transient energy losses. The transient energy loss depends on the EDU rotational speed at the instant of disengagement during braking or the target speed required for synchronization during engagement. Since the EDU rotational speed is linearly proportional to the vehicle speed. For simplicity, the associated synchronization or braking energy loss is approximated as a quadratic function of vehicle speed expressed as

$$E_{\text{sync/brk}} = d_1 v^2 + d_2 v, \tag{3.2}$$

where $E_{\text{sync/brk}}$ denotes the transient energy loss associated with EDU speed synchronization or braking process, and d_1 and d_2 are the fitting coefficients.

3.2.2 Energy management strategy

The AFRID powertrain introduces an additional degree of freedom through the disconnect functionality. Accordingly, the EMS consists of two main components: operating mode selection and torque split.

The operating mode selection governs transitions among FWD, RWD, and AWD modes based on driving conditions. When the powertrain operates in AWD mode, the powertrain torque demand is optimally distributed between the front and rear EDUs to maximize the overall powertrain energy efficiency.

Torque split strategy

In AWD mode, the torque demand required for traction or regenerative braking is distributed between the front and rear EDUs. This relationship can be expressed as

$$T_{\text{dem}} = T_f + T_r, \tag{3.3}$$

where T_{dem} denotes the powertrain torque demand, and T_f and T_r represent the front and rear EDU torques, respectively. To parameterize the torque distribution between the two EDUs, a torque split factor $\alpha \in [0, 1]$ is introduced. The individual EDU torques can then be expressed as

$$\begin{cases} T_f = \alpha T_{\text{dem}}, \\ T_r = (1-\alpha) T_{\text{dem}}. \end{cases} \tag{3.4}$$

The power loss of each EDU is a function of its operating speed and torque. For a given vehicle speed and torque demand, the choice of α directly influences the overall powertrain losses. An optimal torque split can thus be obtained by minimizing the combined losses of the front and rear EDUs. The optimization problem is formulated as

$$\begin{aligned} \min_{\alpha} \quad & P_{\text{EDU,loss},f}(\omega_f, \alpha T_{\text{dem}}) + P_{\text{EDU,loss},r}(\omega_r, (1-\alpha) T_{\text{dem}}), \\ \text{s.t.} \quad & T_{f,\min}(\omega_f) \leq \alpha T_{\text{dem}} \leq T_{f,\max}(\omega_f), \\ & T_{r,\min}(\omega_r) \leq (1-\alpha) T_{\text{dem}} \leq T_{r,\max}(\omega_r), \\ & \alpha \in [0, 1], \end{aligned} \tag{3.5}$$

where ω_f and ω_r denote the rotational speeds of the front and rear EDU output shafts, respectively. $P_{\text{EDU,loss},f}(\cdot)$ and $P_{\text{EDU,loss},r}(\cdot)$ represent the power loss of the front and rear EDUs. $T_{f,\min}(\omega_f)$, $T_{f,\max}(\omega_f)$, $T_{r,\min}(\omega_r)$, and $T_{r,\max}(\omega_r)$ denote the speed-dependent torque limits of the front and rear EDUs. The optimal torque split factor α^* is determined using a grid-search-based approach [108, 109] based on front and rear EDU loss maps.

Mode selection strategy

For each operating mode, a static powertrain loss map is constructed as a function of vehicle speed and powertrain torque demand. In AWD mode, the powertrain loss map is obtained from the optimal torque split solution, where the minimum total powertrain loss is determined by (3.5). In FWD mode, the total powertrain loss is given solely by the front EDU loss map, since the rear EDU is inactive. Likewise, in RWD mode, the total powertrain loss is determined exclusively by the rear EDU loss map.

Although these static loss maps describe steady-state operating losses, additional transient energy losses are incurred when shifting between operating modes due to EDU speed synchronization and braking. These transient losses must be explicitly incorporated into the operating mode selection strategy to avoid excessive transient energy losses from frequent mode shifts. Therefore, DP is employed to determine the optimal operating mode sequence that minimizes the overall powertrain energy loss over a given drive cycle.

The drive cycle is discretized into N stages with a sampling time of $\Delta T = 1$ s. The operating mode is defined as the state variable

$$x_k \in \{1, 2, 3\}, \tag{3.6}$$

where $x_k = 1$, $x_k = 2$, and $x_k = 3$ correspond to FWD, RWD, and AWD operation, respectively. The control input is defined as the mode shift command

$$u_k \in \{-2, -1, 0, 1, 2\}, \tag{3.7}$$

where the value of u_k indicates the change in operating-mode index between two consecutive stages. Specifically, $u_k = 0$ represents no mode shift and the mode transition is governed by

$$x_{k+1} = x_k + u_k. \tag{3.8}$$

Only transitions satisfying $x_{k+1} \in \{1, 2, 3\}$ are admissible. At each stage k, the vehicle speed v_k is assumed to be known, and the corresponding torque demand $T_{\text{dem},k}$ is obtained from the discretized longitudinal vehicle dynamics in (2.20). In addition, the selected operating mode must satisfy the torque feasibility constraint

$$T_{\min}(x_k, v_k) \leq T_{\text{dem},k} \leq T_{\max}(x_k, v_k), \tag{3.9}$$

where $T_{\min}$ and $T_{\max}$ denote the minimum and maximum torque limits associated with each operating mode. Operating modes that violate this constraint are excluded from the DP search.

The instantaneous energy loss at stage k consists of the steady-state powertrain loss associated with the selected operating mode and the transient energy loss caused by a mode shift. The stage cost is therefore defined as

$$g_k(x_k, u_k) = P_{\text{loss},k}(x_k, v_k, T_{\text{dem},k})\, \Delta T + E_{\text{shift},k}(x_k, u_k), \tag{3.10}$$

where $P_{\text{loss},k}(x_k, v_k, T_{\text{dem},k})$ is obtained from the precomputed powertrain loss map of the selected operating mode. The shift energy loss $E_{\text{shift},k}(x_k, u_k)$ accounts for the transient losses associated with the specific operating mode shift as

$$E_{\text{shift}} = \begin{cases} E_{r,\text{sync}}(v_k) + E_{f,\text{brk}}(v_k), & (\text{FWD} \to \text{RWD}), \\ E_{f,\text{sync}}(v_k) + E_{r,\text{brk}}(v_k), & (\text{RWD} \to \text{FWD}), \\ E_{r,\text{sync}}(v_k), & (\text{FWD} \to \text{AWD}), \\ E_{r,\text{brk}}(v_k), & (\text{AWD} \to \text{FWD}), \\ E_{f,\text{sync}}(v_k), & (\text{RWD} \to \text{AWD}), \\ E_{f,\text{brk}}(v_k), & (\text{AWD} \to \text{RWD}), \\ 0, & (\text{no mode shift}), \end{cases} \tag{3.11}$$

where $E_{f,\text{sync}}(v_k)$ and $E_{r,\text{sync}}(v_k)$ denote the transient energy losses associated with synchronizing the front and rear EDUs, respectively, and $E_{f,\text{brk}}(v_k)$ and $E_{r,\text{brk}}(v_k)$ represent the corresponding braking losses.

3.3 Motor design optimization

The AFRID powertrain enables the EMS to determine which EDU is active at each instant through operating mode selection. Allowing asymmetric front and rear motor designs makes it possible to tailor each motor to its dominant operating region, thereby maximizing the energy-saving potential of integrating two disconnect clutches. In this way, the disconnect functionality is not only used to eliminate no-load losses but also to actively route operating points toward the more efficient EDU, thereby improving the overall powertrain energy efficiency.

3.3.1 Problem formulation

The motor design is parameterized by seven geometric variables for both the front and rear motors, as illustrated in Figure 3.4. The corresponding lower and upper bounds are summarized in Table 3.1. Noting that the conductor height ratio is defined as the ratio of the actual conductor height to the reference height corresponding to a slot fully filled with conductors in the radial direction as both motors employ hairpin windings.

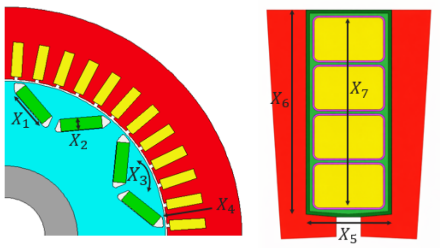

Figure 3.4: *Parameterized motor geometry and selected design variables for the V-shaped IPMSM.*

Table 3.1: Considered motor design parameters and bounds.

Variable	Description	Bounds
X_1	Magnet bar width	[12.0, 20.0]
X_2	Magnet thickness	[3.0, 6.0]
X_3	Pole V-angle	[90.0, 160.0]
X_4	Air gap length	[0.5, 2.0]
X_5	Slot width	[3.0, 6.0]
X_6	Slot depth	[12.0, 18.0]
X_7	Conductor height ratio	[0.9, 1.0]

The optimization focuses on jointly designing the front and rear motors to maximize the energy-saving potential of the disconnect functionality in the AFRID powertrain under the corresponding EMS. Hence the optimization variables consist of the geometric parameters of the front and rear motors, denoted as

$$\boldsymbol{X}_f = [X_{1,f}, \ldots, X_{7,f}], \quad \boldsymbol{X}_r = [X_{1,r}, \ldots, X_{7,r}]. \tag{3.12}$$

The objective of the optimization is to minimize the drive-cycle powertrain energy loss, E_{cycle}, while satisfying vehicle performance constraints, in particular the 0–100 km/h acceleration time. The optimization problem can therefore be formulated as

$$\begin{aligned} \min_{\boldsymbol{X}_f, \boldsymbol{X}_r} \quad & E_{\text{cycle}}, \\ \text{s.t.} \quad & t_{0\text{–}100} \leq t_{\text{lim}}, \\ & \boldsymbol{X}_f \in \Omega_f, \quad \boldsymbol{X}_r \in \Omega_r, \end{aligned} \tag{3.13}$$

where Ω_f and Ω_r denote the feasible geometric design spaces of the front and rear motors, $t_{0\text{–}100}$ denotes the 0–100 km/h acceleration time, and t_{lim} is the specified performance limit. The acceleration time $t_{0\text{–}100}$ is evaluated based on the maximum wheel tractive force in AWD mode as

$$F_{\text{max}} = \frac{1}{R_r} \left(T_{f,\text{max}}(\omega_f) + T_{r,\text{max}}(\omega_r) \right). \tag{3.14}$$

The acceleration time is then computed as a function of the maximum tractive force using the longitudinal vehicle dynamics described in (2.20).

3.3.2 EDU loss map estimation

Due to the strong coupling among motor design, EDU loss maps, and EMS, it is necessary to rapidly estimate the EDU loss maps with a given motor design. This allows the corresponding EMS to be re-optimized during each iteration of the motor design optimization process. In this thesis, a neural-network-based (NN) surrogate model is adopted [110, 111].

Data collection

Based on the design space listed in Table 3.1, a latin hypercube sampling method is used to generate a number of motor design variants through finite element method (FEM) simulations in Ansys Motor-CAD. The geometric validity of each design variant is verified, and infeasible designs are discarded. In addition, samples violating the maximum allowable current density (determined by the conductor height ratio and slot area at maximum current) are excluded. As a result, only geometrically and electrically feasible motor designs are retained for dataset generation. For each design variant, the d–q axis flux linkages and motor losses are sampled over uniform grids in I_d, I_q, and motor speed.

NN-based surrogate model

Three NNs are developed to enable efficient motor loss map construction while retaining key intermediate physical information. Specifically, a flux linkage NN is trained to predict the d–q axis flux linkages, ψ_d and ψ_q, as functions of the motor design variables and current excitation (I_d, I_q). A winding resistance NN is employed to predict the stator phase winding resistance. Since AC loss effects are speed-dependent, both the motor design variables and operating speed are used as inputs. In addition, a motor loss NN is constructed to predict motor loss as a function of the motor design variables, current excitation, and operating speed.

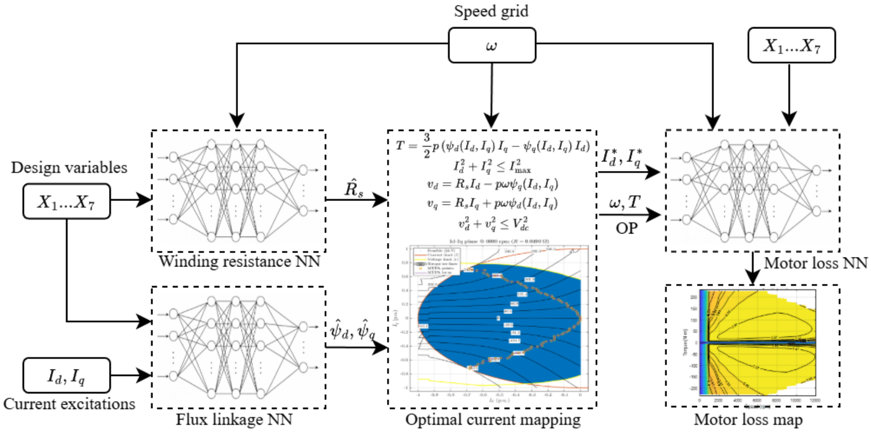

Figure 3.5: *Procedure for motor loss map calculation.*

The overall procedure for motor loss map construction is illustrated in Figure 3.5. For a given motor design, the winding-resistance NN first predicts the stator phase resistance R_s. In parallel, the flux-linkage NN generates the d–q axis flux linkage maps $\psi_d(I_d, I_q)$ and $\psi_q(I_d, I_q)$ over the predefined current bounds. Using the predicted flux linkages and resistance, the optimal current references $(I_d^\star, I_q^\star)$ are determined under current and voltage constraints following the current control strategy discussed in Section 2.1.3. The resulting operating points and corresponding optimal currents are then used as inputs to the motor-loss NN to predict motor losses. The predicted motor losses are further combined with inverter losses calculated using the optimal current references $(I_d^\star, I_q^\star)$ (Section 2.1.2) and transmission losses to construct the complete EDU loss map. The transmission losses are implemented using the same torque-speed-dependent map for the different motor design variants, since the gear ratio is not considered as an optimization parameter and therefore remains constant throughout the analysis.

3.3.3 Optimization framework

A particle swarm optimization (PSO) algorithm is employed to efficiently explore the high-dimensional design space. The framework follows a two-loop structure as illustrated in Figure 3.6.

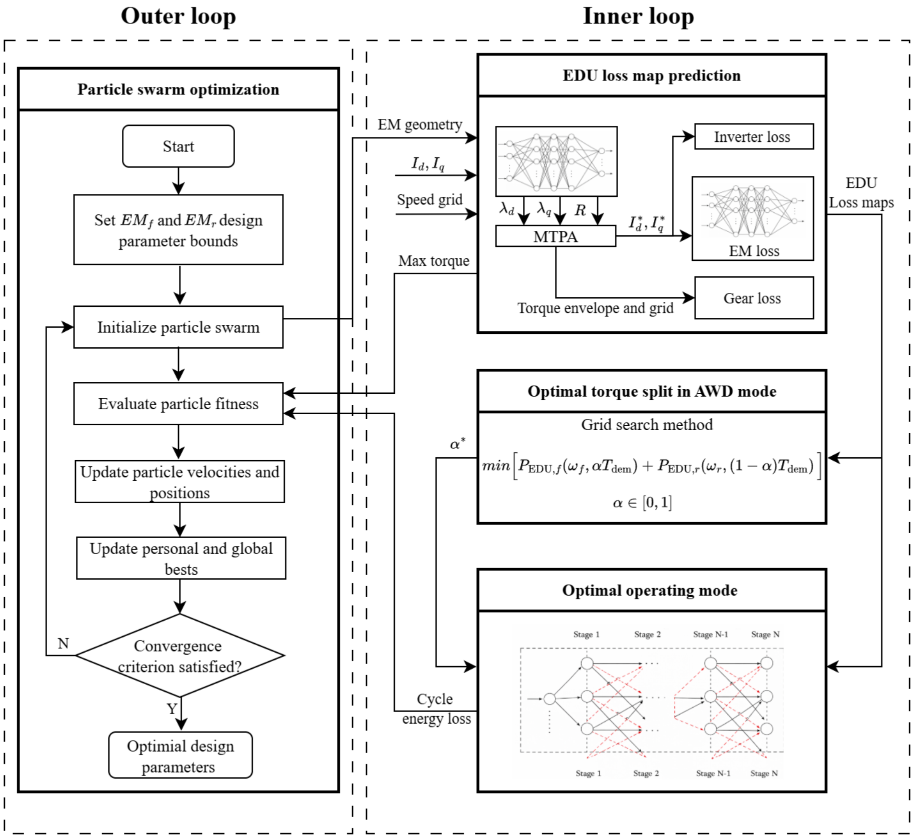

Figure 3.6: *Two-level PSO-based optimization framework for the AFRID powertrain.*

In the outer loop, PSO explores the front and rear motor design spaces, where each particle represents a candidate pair of motor designs within predefined bounds. For each candidate, the inner loop first constructs the corresponding front and rear EDU loss maps. With the updated EDU loss maps, the EMS described in Section 3.2.2 is re-optimized, and the minimum drive-cycle energy loss E_{cycle} is obtained via DP. In addition, the 0–100 km/h acceleration time is evaluated based on the maximum available tractive torque. The resulting energy efficiency and performance metrics are then returned to the outer loop and combined using a quadratic exterior penalty

$$J = E_{\text{cycle}} + \lambda \max(0,\, t_{0\text{–}100} - t_{\text{lim}})^2\,, \tag{3.15}$$

where λ is the penalty coefficient. Within the feasible region ($t_{0\text{–}100} \leq t_{\text{lim}}$), the penalty term is zero and candidates are ranked solely by E_{cycle}.

Particles are iteratively updated according to personal and global best solutions until convergence. The final result yields the optimal asymmetric front and rear motor designs that minimize drive-cycle energy consumption while satisfying the acceleration constraint.

3.4 Results and discussion

3.4.1 Casy study: comparison between AFRID and FRID

To evaluate the energy-saving potential of the disconnect functionality in connection with dual-motor powertrain, a case study is conducted by comparing a conventional FRID powertrain with the AFRID powertrain under the same vehicle and EDU setups. The vehicle parameters are listed in Table 3.2.

Table 3.2: Vehicle parameters.

Parameter	**Symbol**	**Value**	**Unit**
Vehicle mass	m	2640	kg
Vehicle drag coefficient	C_d	0.372	-
Vehicle frontal area	A	2.8	m^2
Tire rolling radius	R_r	377	mm
Tire rolling resistance	C_r	0.01	-

The front and rear EDUs share the same inverter and transmission architecture and operate within a similar torque–speed range, enabling FWD, RWD, and AWD capability across the entire vehicle speed range. However, the motors in the front and rear EDUs employ different winding topologies. The front motor uses stranded windings, whereas the rear motor adopts a hairpin winding configuration [112]. As illustrated in Figure 3.7, the front EDU exhibits higher efficiency at high speeds and low-torque operating conditions due to the stranded winding design. In contrast, the rear EDU operates more efficiently at lower speeds and higher torque levels owing to the hairpin winding configuration.

The resulting optimal torque split ratio and operating modes with minimal powertrain loss, arising from the complementary efficiency characteristics of the front and rear EDUs, are illustrated in Figure 3.8. It can be observed that when two EDUs with different efficiency characteristics are deployed, the optimal torque distribution ratio is not always 0.5, as in the case of two identical EDUs [113]. Furthermore, considering the no-load losses of the EDUs, it is more efficient to use both the front and rear EDUs together, even

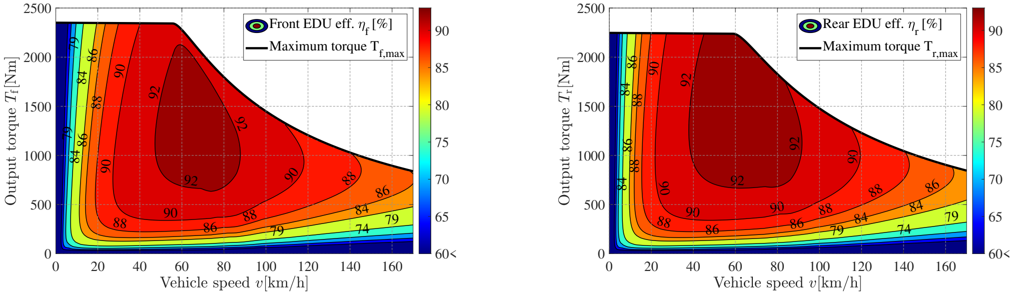

(a) (b)

Figure 3.7: *Efficiency maps. (a) Front EDU. (b) Rear EDU.*

under low-torque operating conditions in AWD mode when disconnect functionality is not considered. For the AFRID powertrain, at low vehicle speeds and medium-to-low torque levels, the RWD mode generally exhibits lower losses. In contrast, at higher vehicle speeds with low-to-moderate torque demand, the FWD mode becomes more efficient. For high torque demands, the AWD mode provides the lowest losses by distributing the torque between the front and rear EDUs.

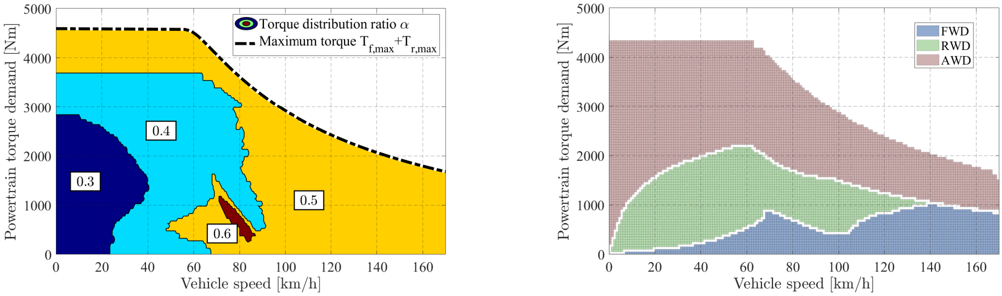

(a) (b)

Figure 3.8: *Powertrain with the investigated front and rear EDUs. (a) Optimal torque split ratio in AWD mode. (b) Operating modes with minimal powertrain loss.*

To access the energy efficiency improvement by the disconnect functionality in connection with dual-motor powertrains, the energy consumption of the AFRID powertrain is evaluated through simulation and compared with the FRID powertrain over WLTC drive cycle. It should be noted that the FRID powertrain operates exclusively in AWD mode with an optimal torque split strategy due to the absence of disconnect functionality. The simulations are conducted in GT-Suite, where the complete powertrain system model together with the corresponding powertrain EMS is implemented, as schematically illustrated in Figure 3.9.

The simulation results are summarized in Table 3.3. Compared to the FRID powertrain, the AFRID configuration achieves 8.21% reduction in energy consumption over the WLTC.

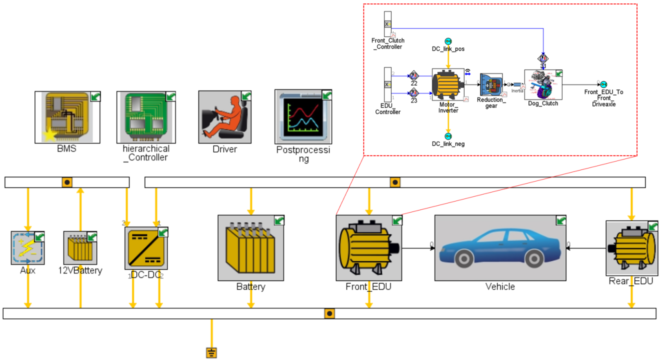

Figure 3.9: *Overview of the GT-Suite simulation model.*

Table 3.3: Energy consumption under WLTC drive cycle.

Powertrain	Energy Cons. [kWh/100 km]
FRID	22.17
AFRID	20.35 (-8.21%)

The comparison of instantaneous powertrain losses between the FRID and AFRID powertrains over the WLTC is illustrated in Figure 3.10. It can be observed that the AFRID powertrain predominantly operates in single-axle drive modes (FWD or RWD) under the whole cycle as the powertrain operates mainly with low-to-medium torque demand, thereby reducing no-load losses by avoiding unnecessary simultaneous operation of both EDUs. In the low-to-medium speed region (before approximately 1000 s), RWD operation is dominant. In this phase, a noticeable reduction in powertrain loss is achieved compared to the FRID powertrain, which operates in AWD mode throughout the cycle. In the medium-to-high and extra-high speed region (after approximately 1200 s), FWD becomes dominant. In this region, the reduction in powertrain loss achieved by AFRID is particularly significant, as EDU no-load losses increase approximately quadratically with speed. Consequently, avoiding the operation of the less efficient EDU at high speeds yields substantial efficiency benefits.

In addition, the AWD mode is primarily activated during high torque demand conditions for acceleration and deceleration. It is generally engaged during the deceleration phase prior to a vehicle stop and maintained for the subsequent launch. Under these conditions, torque sharing between the front and rear EDUs improves overall powertrain efficiency, while the associated transient energy loss is marginal due to low vehicle speed.

It can also be observed that powertrain loss spikes occur in the AFRID configuration during operating mode transitions at higher vehicle speeds (after approximately 800 s). This effect is particularly evident when switching between FWD and RWD modes, as such transitions require synchronization of one EDU and braking of the other, resulting

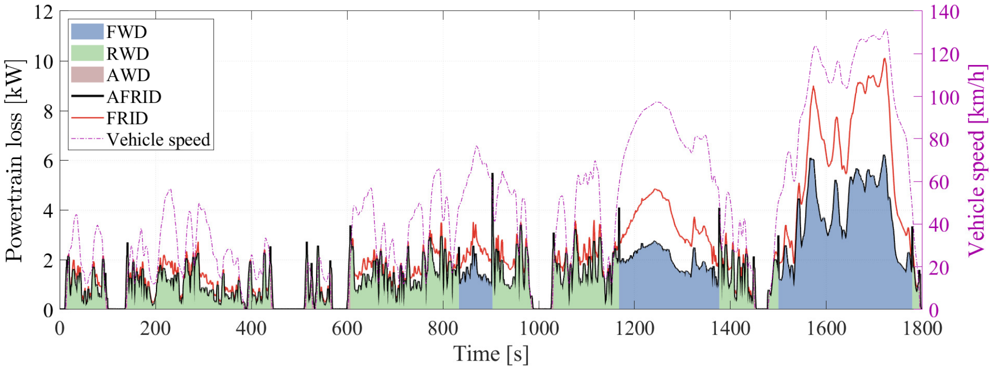

Figure 3.10: *Instantaneous powertrain loss of FRID and AFRID powertrains under the WLTC drive cycle.*

in increased transient energy losses. In contrast, mode transitions at lower speeds mainly occur between RWD and AWD, where only one EDU undergoes synchronization or braking, leading to comparatively minor additional losses. This highlights the importance of accounting for transient energy losses in the EMS design, particularly at higher vehicle speeds. Neglecting such losses may lead to excessive mode shifting, where limited steady-state efficiency gains are offset by relatively large transient losses, ultimately increasing the overall powertrain loss.

3.4.2 Configuration-aware motor design optimization

To fully exploit the energy-saving potential enabled by the disconnect functionality in the AFRID powertrain, motor design optimization is conducted to provide optimally tailored front and rear motor designs for minimizing the WLTC drive-cycle energy loss. In addition, a maximum 0–100 km/h acceleration time of 6 s is imposed as a performance constraint to ensure that vehicle performance is not compromised.

To further highlight the benefit of individually tailored motor designs, a reference AFRID powertrain is introduced for comparison. In this reference case, identical motor designs are assumed for the front and rear EDUs, i.e.,

$$\boldsymbol{X}_f = \boldsymbol{X}_r.$$

Under this symmetry constraint, the same optimization procedure is applied, resulting in a halved number of independent design variables. This comparison reflects the efficiency gains achieved through asymmetric motor design enabled by disconnect functionality.

Optimal motor designs

The optimal motor design parameters obtained from the proposed optimization method for the reference and optimized AFRID cases are summarized in Table 3.4. The designs are then verified by FEM simulations in Ansys Motor-CAD. Figure 3.11 presents the predicted motor efficiency maps, the corresponding FEM-validated maps, and their absolute differences for all three motors. For the majority of the operating range, the absolute efficiency deviation is below 0.1%, with only small localized regions exhibiting discrepancies of approximately 0.5%–0.7% compared with the FEM results. This close agreement validates the effectiveness of the NN-based loss map estimation method.

Table 3.4: Optimal motor design parameters for the reference and optimized AFRID powertrains.

	Reference AFRID	**Optimized AFRID**	
Parameter	$\mathbf{EM_f = EM_r}$	$\mathbf{EM_f}$	$\mathbf{EM_r}$
Magnet thickness [mm]	5.77	6.00	5.46
Magnet bar width [mm]	17.00	20.00	17.17
Pole V-angle [°]	131.14	90.00	128.25
Slot depth [mm]	12.91	15.70	12.00
Slot width [mm]	4.79	4.60	4.05
Air gap length [mm]	1.40	0.89	2.00
Wire height ratio [-]	1.00	1.00	0.92
Maximum torque [Nm]	232	279	222
Maximum power [kW]	187	202	176

A clear distinction in the motor efficiency characteristics can be observed between the reference and optimized AFRID cases. In the reference case, which enforces identical front and rear motors, the efficiency distribution is relatively balanced across a wide speed–torque region. This compromise solution provides moderate efficiency over the entire operating range but does not specifically favor either low-speed or high-speed operation.

In contrast, the optimized AFRID case yields asymmetric front and rear motor designs that are tailored to different operating conditions. The front motor features a thicker magnet, increased magnet bar width, larger effective conductor area, and a reduced air gap. These design choices increase the air-gap flux density and torque capability while lowering DC copper losses through improved conductor utilization, thereby enlarging the high-efficiency region in the low-speed and medium-to-high torque area. This effect is also reflected in the achievable torque: the maximum torque increases from 232 Nm in the reference design to 279 Nm for the optimized front motor. Such characteristics are particularly advantageous during launch and urban driving, where high torque demand dominates.

Conversely, the optimized rear motor adopts a comparatively larger air gap, reduced slot and conductor dimensions, and a lower conductor height ratio. The larger air gap reduces the effective air-gap flux density, leading to a lower peak torque capability (222 Nm), while simultaneously alleviating magnetic saturation and reducing iron losses at elevated speeds [114, 115]. In addition, the reduced conductor height ratio positions the conductors

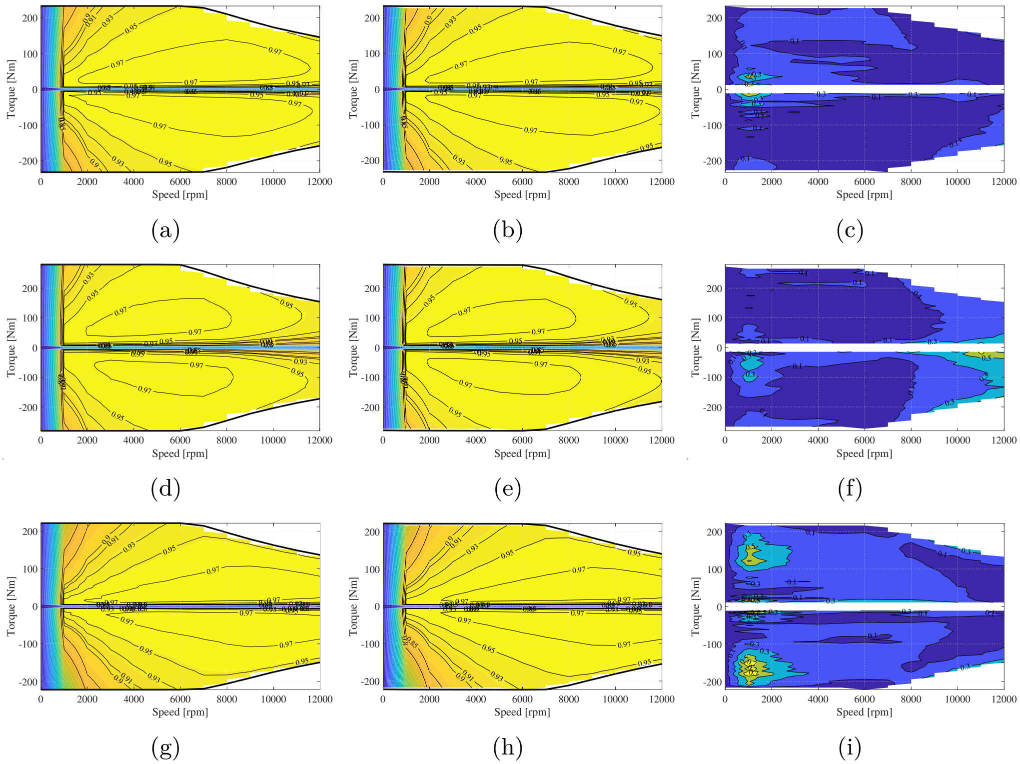

Figure 3.11: *Motor efficiency maps. Left column: predicted. Middle column: FEM. Right column: absolute difference* $|\eta_{\text{pred}} - \eta_{\text{FEM}}|$ *(%). (a)–(c) Front (=rear) motor for reference AFRID powertrain. (d)–(f) Optimized front motor for AFRID powertrain. (g)–(i) Optimized rear motor for AFRID powertrain.*

deeper inside the slot, increasing their distance from the slot opening where high-frequency leakage flux is strongest [116]. This mitigates proximity and skin-effect losses, which are particularly significant for hairpin windings, thereby decreasing AC copper losses during high-speed operation [117]. As a result, the rear motor achieves superior efficiency in the medium-to-high speed region and is better suited for cruising conditions characterized by lower torque and higher rotational speeds.

Efficiency improvement

The energy consumption and acceleration performance are then evaluated using powertrain system simulation carried out in GT-Suite.

The WLTC drive-cycle energy consumption and 0–100 km/h acceleration performance obtained for the two cases are summarized in Table 3.5. The optimized AFRID powertrain reduces the WLTC battery energy consumption from 20.41 to 20.21 kWh/100 km,

Table 3.5: WLTC energy consumption and acceleration performance.

	Reference AFRID	**Optimized AFRID**
Energy Cons. [kWh/100 km]	20.41	20.21 (-0.98%)
t_{0-100} [s]	5.7	5.3 (-7.02%)

corresponding to an improvement of 0.98%. Both cases satisfy the imposed performance constraint for the optimization, with 0–100 km/h acceleration times below 6 s. In addition, the optimized AFRID exhibits slightly improved performance, with 0.4 s faster acceleration time.

The optimal operating modes of both cases over WLTC drive cycle, obtained from the DP-based mode selection strategy, are illustrated in Figure 3.12. Additionally, the corresponding operating points of each EDU projected on the efficiency maps under different operating modes are presented in Figure 3.13.

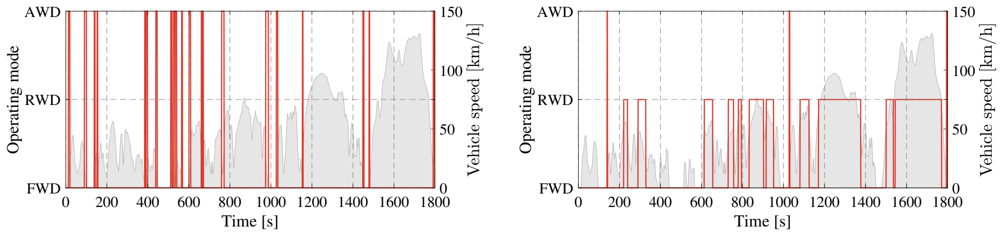

(a) (b)

Figure 3.12: *Operating mode sequences over the WLTC driving cycle. (a) Reference AFRID powertrain. (b) Optimized AFRID powertrain.*

It is worth noting that the reference AFRID powertrain with identical front and rear motor/EDUs only operates optimally between FWD and AWD mode. This is as expected as the two motors exhibit identical efficiency characteristics, resulting in the same loss behavior for FWD and RWD operation. In other words, the reference AFRID powertrain is effectively equivalent to a conventional FRID powertrain with a single clutch. Moreover, AWD operation is rarely selected over the WLTC drive cycle and occurs only sporadically during low-speed, high-torque conditions, such as vehicle launch and deceleration to a stop. Therefore, when identical motors are employed, the second clutch offers limited practical advantage from an energy-efficiency perspective.

For the optimized AFRID powertrain, AWD operation becomes almost negligible over the WLTC cycle, with most vehicle launch and braking events handled in FWD mode compared with the reference configuration. This behavior can be attributed to the improved low- and medium-speed efficiency and higher torque capability of the optimized front motor, whose high-efficiency operating region covers the majority of these operating conditions, as illustrated in Figure 3.13a and Figure 3.13c. Moreover, the operating time is approximately evenly distributed between FWD and RWD modes. FWD dominates the low- and medium-speed segments of the cycle (first 1200 s), while RWD is utilized

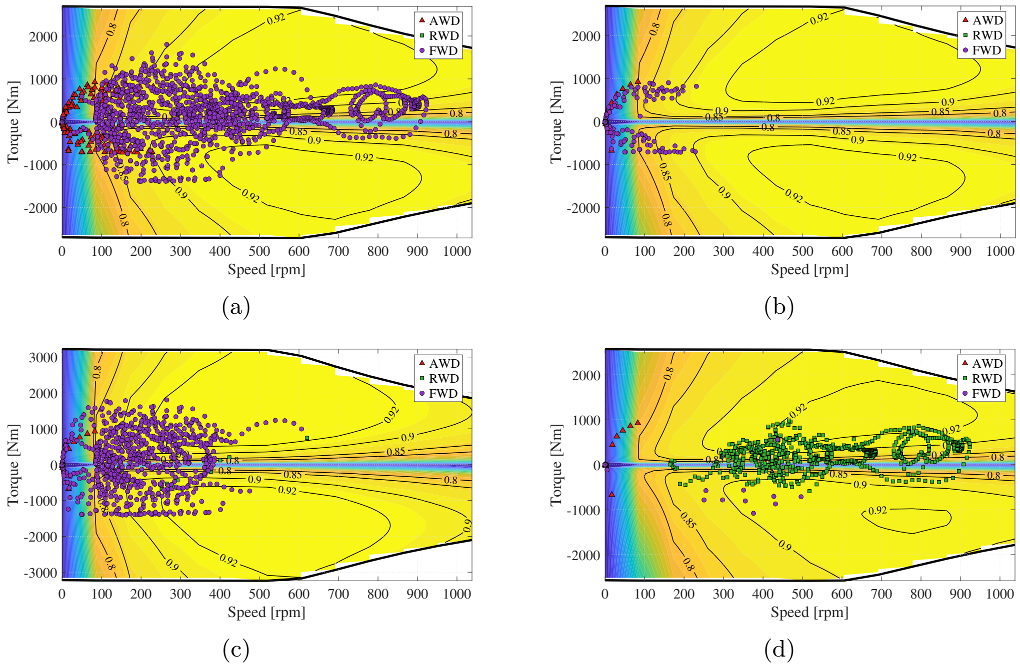

Figure 3.13: *Operating points of each EDU projected onto the EDU efficiency maps under different operating modes over the WLTC drive cycle. (a) Front EDU of reference AFRID. (b) Rear EDU of reference AFRID. (c) Front EDU of optimized AFRID. (d) Rear EDU of optimized AFRID.*

more frequently during the high- and extra-high-speed sections after 1200 s. This shift reflects the superior high-speed efficiency of the optimized rear motor.

3.4.3 Number of clutch and motor asymmetry

The AFRID powertrain enables independent activation of the front and rear EDUs through dual disconnect clutches, allowing efficient single-axle operation over a large portion of driving conditions. This architectural flexibility leads to a substantial WLTC energy consumption reduction to 20.35 kWh/100 km, corresponding to an 8.21% improvement relative to the FRID powertrain. This result is obtained for the case of mild motor asymmetry introduced through differences in winding topology between the front and rear motors.

The achievable efficiency benefit is strongly influenced by the degree of motor asymmetry. The task-oriented asymmetric front and rear motor design enabled by the proposed co-optimization framework expands the effective high-efficiency operating region of the

AFRID powertrain and reduces the WLTC energy consumption to 20.21 kWh/100 km, corresponding to an additional improvement of 0.69%.

This also underlines the importance of employing two independent disconnect clutches. When identical motors are used in the reference AFRID powertrain, the additional operational flexibility provided by dual clutches cannot be effectively exploited, and the system behavior approaches that of a conventional single-clutch dual-motor powertrain. In contrast, asymmetric motor characteristics allow each EDU to operate more frequently within its optimal efficiency region, thereby enabling meaningful utilization of both clutches. As a result, a total WLTC energy consumption reduction of approximately 0.98% is achieved relative to the AFRID configuration with identical motors (20.41 kWh/100 km), which is also representative of the optimized single-clutch FRID powertrain.

3.4.4 Summary

This chapter investigated the energy-saving potential of disconnect functionality in dual-motor powertrains through the proposed AFRID configuration. By independently decoupling the front and rear EDUs, the AFRID configuration provides additional operational flexibility compared with the conventional FRID powertrain and avoids unnecessary no-load losses through single-axle operation over large portions of typical driving conditions.

The first study primarily evaluates the benefit of disconnect functionality. The front and rear motor designs are fixed and exhibit mildly different efficiency characteristics due to the use of stranded and hairpin windings, respectively. Compared with the FRID powertrain, the AFRID configuration reduces the WLTC energy consumption from 22.17 to 20.35 kWh/100 km, corresponding to an improvement of 8.21%. This improvement is mainly enabled by the disconnect functionality. The different winding technologies also influence the preferred operating mode and torque distribution through their differentiated efficiency characteristics, although this contribution is not separately quantified.

The subsequent study investigates the additional benefit of tailoring the motor designs to the AFRID architecture. In this study, both motors employ hairpin windings, while their geometric parameters, including magnet dimensions, air gap, slot geometry, and conductor dimensions, are optimized. A reference AFRID powertrain is first obtained using the proposed optimization framework while imposing identical front and rear motor designs, resulting in a WLTC energy consumption of 20.41 kWh/100 km. When the identical-motor constraint is removed, the resulting optimized asymmetric motors achieve 20.21 kWh/100 km, corresponding to an improvement of approximately 0.98% relative to the reference AFRID configuration with identical motors. Since both cases are obtained using the same optimization framework and employ the same AFRID architecture and hairpin winding technology, this improvement reflects the benefit of geometric motor asymmetry together with the ability of the EMS to exploit the resulting differentiated efficiency characteristics.

Compared with the mildly asymmetric AFRID configuration from the first study, the optimized asymmetric design provides a further reduction from 20.35 to 20.21 kWh/100 km, corresponding to approximately 0.69%. This indicates that mild asymmetry introduced through different winding technologies already provides some opportunity to exploit the two independent disconnect clutches, while task-oriented geometric optimization further differentiates the motor efficiency regions and enables more effective use of FWD and RWD operation.

The efficiency benefit is therefore closely related to the interaction between motor asymmetry and the EMS. With identical motors, FWD and RWD exhibit essentially identical loss characteristics, limiting the practical benefit of the second clutch and making the system behave similarly to a single-clutch dual-motor powertrain. With asymmetric motors, the EMS can instead route operating points toward the more efficient EDU, allowing each motor to operate more frequently within its preferred high-efficiency region.

Overall, the disconnect functionality provides the primary energy-saving mechanism by eliminating unnecessary no-load losses, while asymmetric motor design and coordinated EMS provide incremental but meaningful gains by allowing the EMS to exploit the dual-clutch AFRID architecture more effectively.

4 Eco-driving with Disconnect Functionality

This chapter is based on Paper III. The objective of this chapter is to investigate the energy-saving potential achieved by utilizing the free-coasting capability enabled by a disconnect functionality.

4.1 Free-coasting operation

Under legislative drive cycle constraints, at least one EDU must remain engaged to ensure strict speed tracking. Accordingly, Chapter 3 showed that, in dual-motor powertrains, disconnect functionality primarily reduces no-load losses by deactivating one EDU while the other supplies the required traction torque. In contrast, full free-coasting could be achieved with all EDUs disconnected if strict speed tracking were relaxed, as may be permissible in real-world driving scenarios.

To examine the free-coasting potential, a single-motor powertrain equipped with disconnect functionality is considered, as illustrated in Figure 4.1. The disconnect functionality enables complete mechanical decoupling of the EDU from the drive axle, allowing genuine free-coasting operation in which the vehicle utilizes its kinetic energy without incurring powertrain losses or drag. The energy-saving potential of disconnect functionality in a single-motor powertrain is closely linked to the possibility of optimizing the vehicle speed trajectory itself. By allowing bounded deviations from a reference speed and strategically planning acceleration and coasting phases, the clutch can be disengaged more frequently and for longer durations.

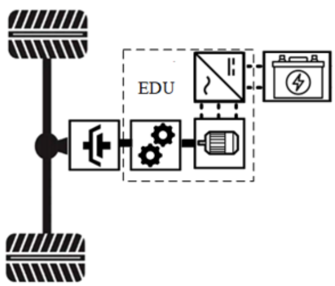

Figure 4.1: *Single-motor powertrain with disconnect functionality.*

4.2 Eco-driving strategy

The eco-driving strategy can be formulated as an optimal control problem (OCP), in which vehicle dynamics, road information, and a reference speed profile are incorporated. The objective is to minimize powertrain energy loss by determining an optimal vehicle speed trajectory within a permissible range.

4.2.1 Problem formulation

Since road gradient and speed limits are location-dependent, the problem can be reformulated in spatial coordinates as

$$\frac{dv}{dt} = \frac{dv}{ds}\frac{ds}{dt} = \frac{dv}{ds}v, \tag{4.1}$$

where t and s are the time and distance notations, respectively. By combining (2.20) and (4.1) and assuming that the brake demand is fully covered by regenerative braking, the vehicle dynamics in spatial form is derived as

$$\frac{\mathrm{d}v}{\mathrm{d}s} = \frac{\frac{T_{\mathrm{dem}}}{R_r} - mg\sin(\theta(s)) - \frac{1}{2}\rho C_d A v^2 - C_r mg\cos(\theta(s))}{(m+m_i)v}. \tag{4.2}$$

By applying the Euler forward method, (4.2) is discretized as

$$v(k+1) = \ v(k) + \frac{\Delta s}{(m+m_i)v}\left(\frac{T_{\mathrm{dem}}}{R_r} - mg\sin(\theta(s)) - \frac{1}{2}\rho_a C_d A v^2 - C_r mg\cos(\theta(s))\right).$$

where Δs is the discretized distance interval. Since eco-driving is intended for real-world implementation with continuously updated road preview information, the OCP must be solved online. MPC is therefore adopted, as it enables real-time, receding-horizon optimization while incorporating future route information.

Eco-driving without disconnect functionality

For the conventional powertrain without disconnect functionality, the EDU torque is the only control variable for the OCP as

$$u(k) = [T(k)] \tag{4.3}$$

The cost function consists of two terms representing the control objectives of trip time and cumulative powertrain energy loss over the control horizon as

$$\min_{T(\cdot|k)} \lambda_1 \sum_{i=0}^{N} \frac{\Delta s}{v[k+i \mid k]} + \lambda_2 \sum_{i=0}^{N} P_{\text{loss}}[k+i \mid k] \frac{\Delta s}{v[k+i \mid k]} \tag{4.4}$$

where the prediction and control horizons are set as N, $[k+i|k]$ denotes the value of the corresponding variables at the future i-th distance step predicted at the current distance step k, and λ_1 and λ_2 are the weighting factors.

In addition, the problem is subject to

$$T_{\min}(v[k+i \mid k]) \leq T[k+i \mid k] \leq T_{\max}(v[k+i \mid k]) \tag{4.5}$$

$$(1-\alpha_{\text{dev}})v_{\text{ref}}[k+i] \leq v[k+i \mid k] \leq (1+\alpha_{\text{dev}})v_{\text{ref}}[k+i] \tag{4.6}$$

The constraints above ensure the EDU torque demand stays within the limits. Moreover, a coefficient α_{dev} is introduced to define the permissible deviation from the reference speed, ensuring that the actual speed stays within an acceptable range relative to the reference speed v_{ref}.

To facilitate numerical computation within the OCP, the static EDU loss maps are approximated using polynomial functions. Accordingly, the EDU loss power is represented as a polynomial function of vehicle speed and EDU torque as

$$P_{\text{loss}}(v, T) = \sum_{i=0}^{2} \sum_{j=0}^{2} \alpha_{ij} v^i T^{2j}, \tag{4.7}$$

where α_{ij} is the fitted coefficient.

Similarly, the torque limits are approximated as polynomial functions of vehicle speed as

$$T_{\max}(v) = \sum_{i=0}^{5} \beta_k v^i, \tag{4.8}$$

$$T_{\min}(v) = \sum_{i=0}^{5} \gamma_k v^i, \tag{4.9}$$

where β_k and γ_k are the fitted coefficients. These fitted representations provide smooth and computationally efficient approximations of the original map-based characteristics as depicted in Figure 4.2.

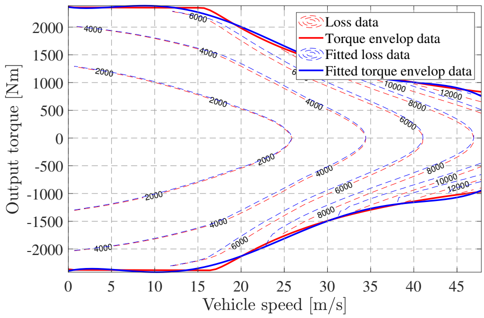

Figure 4.2: *EDU loss map and torque envelope in reference to vehicle speed and EDU torque.*

Eco-driving with disconnect functionality

For the single-motor powertrain with disconnect functionality, the OCP incorporates two control variables

$$u(k) = [T(k), c(k)], \tag{4.10}$$

where c is the clutch state which is a binary variable indicating engagement and disengagement state with 1 and 0, respectively. To account for the transient energy loss associated with EDU synchronization during engagement and braking during disengagement, a clutch actuation variable z is introduced to represent clutch state transitions as

$$z[k+i \mid k] = c[k+i \mid k] - c[k+i-1 \mid k], \tag{4.11}$$

with

$$z[k+i \mid k] \in \{-1, 0, 1\}, \tag{4.12}$$

where $z = -1, 0, 1$ indicate disengagement, no actuation, and engagement event. To represent transient energy losses associated with synchronization and braking events in a compact form, the formulation in (3.1) is modified by introducing a signed speed term. This is achieved by multiplying the clutch state transition variable z with the vehicle speed v, yielding

$$E_{\text{sync/brk}} = d_1(zv)^2 + d_2(zv), \tag{4.13}$$

where positive values of zv correspond to clutch engagement (synchronization), while negative values represent disengagement (braking), as illustrated in Figure 4.3. This representation enables both engagement and disengagement transient losses to be captured within a unified mathematical expression suitable for numerical optimization.

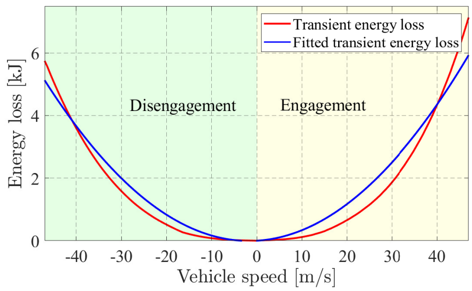

Figure 4.3: *Transient energy loss during engagement and disengagement events in reference to vehicle speed.*

Consequently, the cost function consists of three terms representing the objectives of trip time minimization, cumulative powertrain energy loss, and transient energy loss over the prediction horizon. The OCP is formulated as

$$\begin{aligned}
\min_{T(\cdot|k),\, c(\cdot|k)} \quad & \lambda_1 \sum_{i=0}^{N} \frac{\Delta s}{v[k+i \mid k]} + \lambda_2 \sum_{i=0}^{N} P_{\text{loss}}[k+i \mid k] \frac{c[k+i \mid k]\Delta s}{v[k+i \mid k]} \\
& + \lambda_2 \sum_{i=0}^{N} E_{\text{sync/brk}}[k+i \mid k], \\
\text{s.t.} \quad & T[k+i \mid k] \geq c[k+i \mid k]\, T_{\min}(v[k+i \mid k]), \\
& T[k+i \mid k] \leq c[k+i \mid k]\, T_{\max}(v[k+i \mid k]), \\
& (1-\alpha_{\text{dev}})\, v_{\text{ref}}[k+i] \leq v[k+i \mid k] \leq (1+\alpha_{\text{dev}})\, v_{\text{ref}}[k+i], \\
& c[k+i \mid k] \in \{0, 1\}, \qquad i = 0, \ldots, N.
\end{aligned} \tag{4.14}$$

Since the cumulative powertrain loss and the transient synchronization/braking energy are of the same physical scale, the same weighting factor λ_2 is applied to both terms. When the clutch is disengaged ($c = 0$), the powertrain loss term becomes zero, reflecting the elimination of no-load losses. The first two constraints ensure the EDU torque is zero when the clutch is disconnected.

4.2.2 MPC setup

The eco-driving OCP is solved in a receding-horizon framework using MPC. At each spatial step, the OCP defined in (4.14) is solved over a finite horizon N using the latest available road preview information, including road gradient and speed limits. In this work, a spatial discretization step of $\Delta s = 20$ m is adopted. The prediction horizon is set to $N = 5$, corresponding to a preview distance of 100 m.

For a conventional powertrain without disconnect functionality, the OCP is a continuous nonlinear programming (NLP) problem. The interior-point optimizer (IPOPT) is employed due to its efficiency in handling large-scale nonlinear optimization problems with smooth dynamics and constraints.

In contrast, for the single-motor powertrain with disconnect functionality, the clutch state $c \in \{0, 1\}$ introduces discrete decision variables into the optimization problem. This results in a mixed-integer nonlinear programming (MINLP) formulation, where continuous variables, such as vehicle speed and traction torque, are coupled with binary clutch actuation decisions. The MINLP is solved using the open-source solver BONMIN, which employs a branch-and-bound framework with NLP relaxations to determine the optimal clutch engagement sequence and torque trajectory.

To improve computational efficiency in the receding-horizon implementation, a warm-start strategy is employed [118].

4.3 Results and discussion

4.3.1 Driving route

Three representative driving routes are selected, corresponding to Low-Speed (LS), Medium-Speed (MS), and High-Speed (HS) operating conditions, as illustrated in Figure 4.4. These routes capture different traffic characteristics and road environments typical of real-world driving. The route data, including speed profiles and elevation information, are obtained from measurement campaigns described in [102].

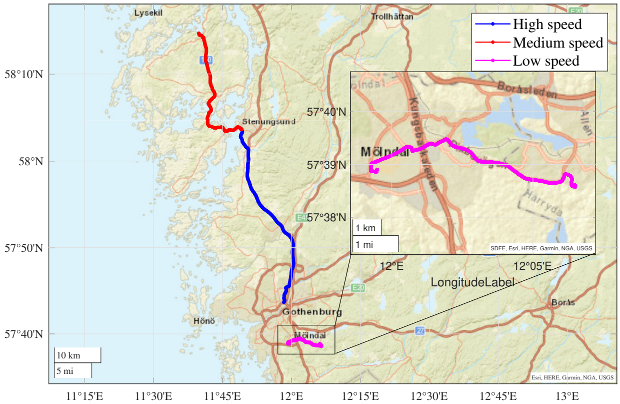

Figure 4.4: *Investigated representative routes in the Västra Götalands region, Sweden.*

4.3.2 Efficiency improvement

To assess the energy-saving potential of the proposed eco-driving strategy with disconnect functionality, three simulation cases are considered. Two powertrain configurations are evaluated using identical vehicle parameters (Table 3.2) and EDU characteristics (Figure 4.2). First, a baseline case without eco-driving is established, in which the vehicle strictly follows the recorded speed profile obtained from the route data. Second, an eco-driving strategy is applied to a conventional single-motor powertrain without disconnect functionality. Finally, the proposed eco-driving strategy with disconnect functionality is evaluated. To ensure a fair comparison without compromising trip duration, the weighting factors in the MPC cost function are slightly adjusted for each scenario such that comparable trip times are achieved.

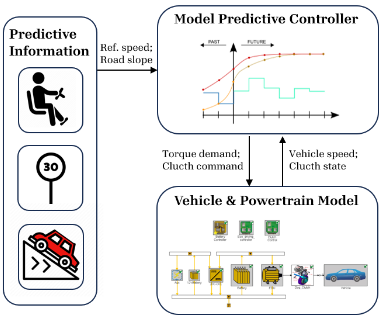

Figure 4.5: *Structure of the co-simulation framework.*

A co-simulation framework combining GT-Suite and Simulink is employed, as illustrated in Figure 4.5. Within the GT-Suite environment, a powertrain model is developed. The high-level eco-driving controller based on MPC is implemented in Simulink and MATLAB using the CasADi toolbox [119]. The controller utilizes road and traffic information along with real-time vehicle state feedback to compute optimal traction torque and clutch actuation commands. These control inputs are subsequently communicated to the GT-Suite to evaluate the resulting vehicle response and energy consumption.

Table 4.1 summarizes the resulting energy consumption for the three investigated driving routes under a permissible deviation from the reference speed profile of $\alpha_{\text{dev}} = 10\%$ when applying the eco-driving strategy. As illustrated in Figure 4.6, the primary energy-saving mechanism of eco-driving in a conventional powertrain lies in smoothing the speed trajectory, thereby reducing torque fluctuations and associated losses. Consequently, the implementation of eco-driving already leads to a noticeable reduction in energy consumption across all routes, confirming the effectiveness of predictive speed planning and trajectory smoothing.

Table 4.1: Energy consumption for different driving routes.

Route	**Baseline [kWh/100 km]**	**Eco-driving w/o disconnect [kWh/100 km]**	**Eco-driving w disconnect [kWh/100 km]**
LS	14.08	13.33 (-5.3%)	12.44 (-11.6%)
MS	18.26	16.96 (-7.1%)	16.58 (-9.2%)
HS	23.31	22.34 (-4.2%)	21.20 (-9.1%)

Further improvements are achieved when disconnect functionality is incorporated into the eco-driving strategy. Compared to the baseline case, energy reductions of 11.6%, 9.2%, and 9.1% are obtained for the LS, MS, and HS routes, respectively, whereas the eco-driving strategy without disconnect functionality yields smaller reductions of 5.3%, 7.1%, and 4.2%. These results highlight the additional benefit of enabling genuine free-coasting operation, which allows the vehicle to utilize its kinetic energy without incurring powertrain losses during disengaged phases.

The relative improvement is most pronounced in the LS route due to its highly dynamic speed profile, which provides more frequent opportunities for disengagement and extended coasting. In this scenario, the drivetrain remains disengaged for approximately 64% of the driving time. In contrast, the MS and HS routes exhibit less dynamic speed variations, resulting in reduced coasting opportunities, with disengagement occurring for approximately 50% of the time. The resulting operation resembles a pulse-and-glide (PnG)-like behavior [36, 37]; however, the proposed eco-driving framework maintains adherence to a continuously varying reference speed profile and explicitly accounts for route-dependent constraints.

4.3.3 Summary

This chapter investigated the role of disconnect functionality when integrated within an eco-driving strategy for single-motor powertrains. In addition to the conventional efficiency improvements achieved through speed trajectory smoothing and predictive

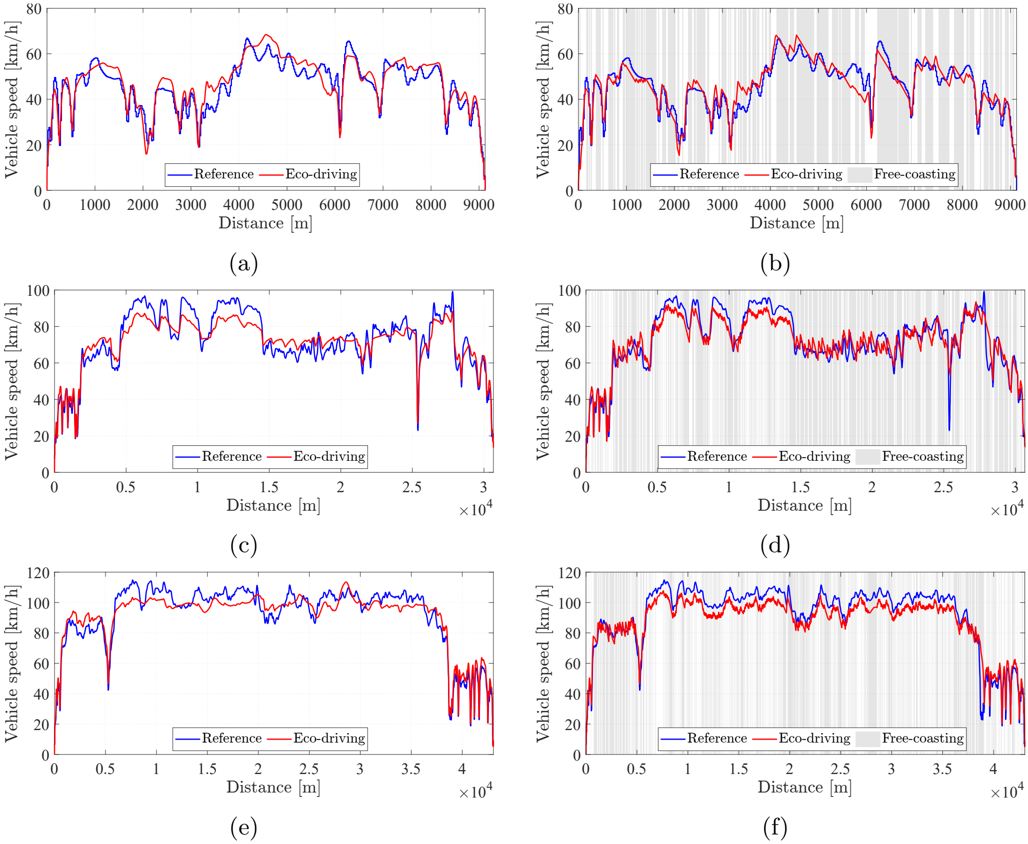

Figure 4.6: *Vehicle speed under eco-driving compared to the reference profile. (a, c, e) Powertrain without disconnect functionality. (b, d, f) Powertrain with disconnect functionality. Rows represent LS, MS, and HS driving scenarios, respectively.*

control, mechanical decoupling enables genuine free-coasting by allowing the EDU to remain disconnected during suitable operating phases. This capability introduces a distinct energy-saving mechanism that complements traditional eco-driving approaches.

Moreover, the advantages of disconnect functionality can potentially extend beyond single-motor configurations. In the AFRID powertrain discussed in Chapter 3, disconnect capability can introduce an additional operating mode alongside FWD, RWD, and AWD, namely a dedicated coasting mode. This expanded operational flexibility allows the powertrain to transition into a fully disengaged state when propulsion is not required, thereby enhancing overall efficiency.

5 Adjustable DC-link Voltage

This chapter is based on the work presented in Papers II and VII. The main objective is to evaluate the potential improvement in the energy efficiency of BEV powertrains through optimal adjustment of the DC-link voltage.

5.1 Powertrain configuration

The adjustable DC-link voltage powertrain, illustrated in Figure 5.1, incorporates a bidirectional DC–DC converter between the battery and the inverter. This configuration enables independent control of the DC-link voltage during both propulsion and regenerative operation of the powertrain.

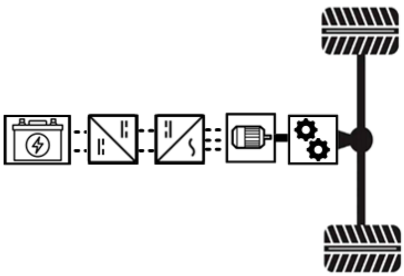

Figure 5.1: *Adjustable DC-link voltage powertrain configuration with bidirectional DC-DC converter.*

Depending on the arrangement of the high-voltage and low-voltage sides of the DC–DC converter with respect to the battery terminal and the DC-link, the converter can be arranged in either boost or buck configuration. In boost configuration, the DC-link voltage is increased above the battery terminal voltage. Conversely, in buck configuration, the DC-link voltage is reduced below battery terminal voltage.

5.2 Operating principle

5.2.1 Varying DC-link voltage

For the motor operations, the energy-efficient MTPA control strategy is constrained by the available DC-link voltage supply, as described in Section 2.1.3. Below the base speed (i.e., before the DC-link voltage constraint becomes active), the motor operation follows the MTPA trajectory. In this operating region, the motor losses and torque output are largely insensitive to the DC voltage. As the supplied DC-link voltage increases, the voltage constraint in the I_d–I_q plane expands, resulting in a higher base speed and a larger operating region where the MTPA strategy can be maintained. Consequently, a higher DC-link voltage can improve torque capability and efficiency at higher motor speeds. Figure 5.2 illustrates the motor loss maps under different DC-link voltages.

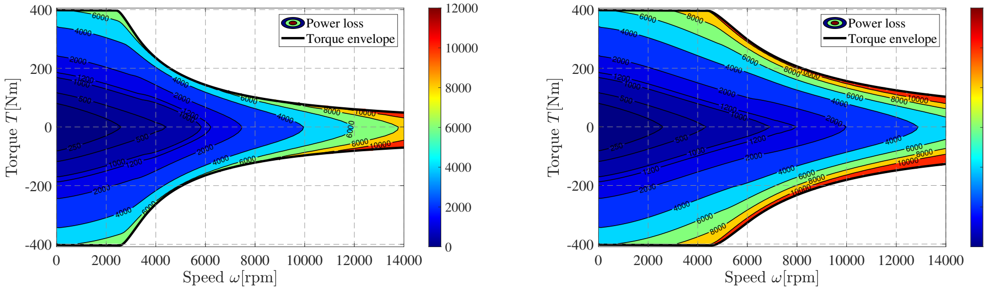

(a) (b)

Figure 5.2: *Motor loss maps with different DC-link voltages. (a) 250 V (b) 450 V.*

On the other hand, the inverter losses are also influenced by the DC-link voltage, as described in Section 2.1.2. Figure 5.3 shows inverter loss maps corresponding to different DC-link voltage levels. At low motor speeds, operating below the base speed, the required motor current remains nearly identical across different DC-link voltages under the MTPA strategy. As a result, the conduction losses in the inverter remain unchanged. However, switching losses increase with higher DC-link voltage, making a lower DC-link voltage more favorable for efficiency in low-speed operating conditions. At higher speeds, the inverter losses are increasingly dominated by conduction losses. Since a higher DC-link voltage extends the motor's MTPA operating region and reduces the current required to produce the same torque, the inverter conduction losses decrease. Therefore, a higher DC-link voltage becomes advantageous in high-speed operating conditions.

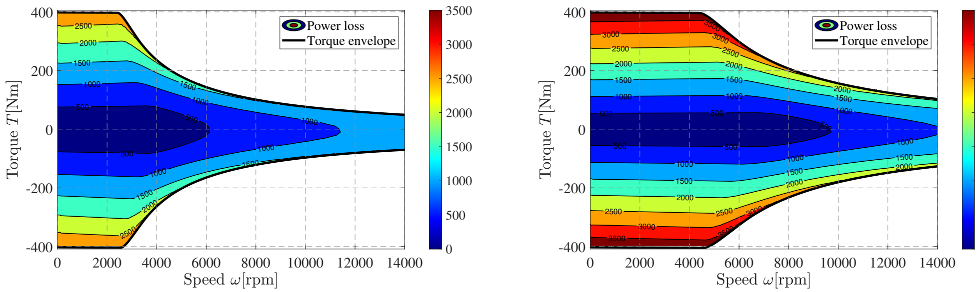

(a) (b)

Figure 5.3: *Inverter loss maps with different DC-link voltages (Infineon FS820R08A6P2B IGBT module). (a) 250 V (b) 450 V.*

These observations indicate that the optimal DC-link voltage depends strongly on the operating conditions of the powertrain. Lower DC-link voltage is generally beneficial at low-speed operation due to reduced switching losses, whereas higher DC-link voltage becomes advantageous at higher speeds by reducing current-related losses. In a conventional BEV powertrain, the DC-link voltage is determined by the battery terminal voltage and therefore cannot be independently controlled. The introduction of a bidirectional DC–DC converter between the battery and the inverter decouples the DC-link voltage from the battery voltage and enables dynamic adjustment of the DC-link voltage according to the vehicle operating conditions, thereby improving overall powertrain efficiency.

5.2.2 DC-link voltage optimization

While a DC–DC converter enables DC-link voltage adjustment, it also introduces additional conversion losses. Consequently, a thorough optimization of powertrain energy efficiency across different driving conditions must be performed at the system level. This requires accounting for losses in all powertrain components, including the DC–DC converter. To explore the full energy-saving potential offered by adjusting DC-link voltage over different driving conditions, DP-based optimization is employed to determine the optimal DC-link voltage sequence over a given drive cycle. The optimization explicitly considers the variation of battery operating conditions, including the dependence of battery OCV and internal resistance on the SoC, as well as the voltage drop across the internal resistance under load.

The drive cycle is discretized into N stages with a sampling time of $\Delta T = 1$ s. At each stage k, the vehicle speed v_k is assumed to be known, and the corresponding EDU operating point (ω_k, T_k) is obtained from the longitudinal vehicle dynamics as described in (2.20). The battery SoC is defined as the state variable x_k

$$x_k = \mathrm{SoC}_k. \tag{5.1}$$

The control input is defined as the DC-link voltage

$$u_k = V_{\mathrm{dc},k}, \tag{5.2}$$

which is constrained within the allowable voltage range determined by the converter configuration and battery terminal voltage. The state transition is governed by the battery current according to

$$x_{k+1} = x_k - \frac{I_{\mathrm{bat},k}(x_k, u_k)}{C_{\mathrm{bat}}} \Delta T, \qquad k = 0, 1, \ldots, N-1. \tag{5.3}$$

The instantaneous powertrain loss at stage k is defined as

$$g_k(x_k, u_k) = \left(P_{\text{bat,loss}}(x_k, u_k) + P_{\text{DCDC,loss}}(x_k, u_k) + P_{\text{EDU,loss}}(\omega_k, T_k, u_k)\right) \Delta T, \quad (5.4)$$

The optimization is subject to the following constraints

$$\begin{aligned} \text{SoC}_{\min} \leq x_k &\leq \text{SoC}_{\max}, \\ T_{\min}(\omega_k, u_k) \leq T_k &\leq T_{\max}(\omega_k, u_k), \\ I_{\text{bat,min}} \leq I_{\text{bat},k}(x_k, u_k) &\leq I_{\text{bat,max}}, \\ V_{\text{bat},k}(x_k) \leq u_k &\leq V_{\text{dc,max}}, \qquad \text{(boost configuration)}, \\ V_{\text{dc,min}} \leq u_k &\leq V_{\text{bat},k}(x_k), \qquad \text{(buck configuration)}. \end{aligned} \quad (5.5)$$

where $\text{SoC}_{\min}$ and $\text{SoC}_{\max}$ denote the minimum and maximum allowable battery SoC limits, respectively. $I_{\text{bat,min}}$ and $I_{\text{bat,max}}$ denote the minimum and maximum allowable battery current, determined by the battery operating limits and the current capability of the power electronic components during regeneration and propulsion, respectively.

Operating points violating these constraints are excluded from the DP search. The EDU loss can be evaluated directly from loss maps and analytical models as functions of speed, torque and DC-link voltage. In contrast, the battery loss and DC–DC converter loss depend on the battery current and terminal voltage. To evaluate these quantities, the DC-link power balance is enforced as

$$P_{\text{bat},k} - P_{\text{DCDC,loss}}(x_k, u_k) = P_{\text{EDU,loss}}(\omega_k, T_k, u_k) + P_{\text{mech}}(\omega_k, T_k), \quad (5.6)$$

where $P_{\text{bat},k} = V_{\text{bat},k} I_{\text{bat},k}$ denotes the battery terminal power and $P_{\text{mech}}(\omega_k, T_k)$ represents the mechanical power delivered by the EDU. This formulation solves for battery current $I_{\text{bat},k}$ and the terminal voltage $V_{\text{bat},k}$, allowing the corresponding battery and DC–DC converter losses in (5.4) to be evaluated under different operating conditions and battery states during the DP process.

5.3 Results and discussion

5.3.1 Boost configuration with Si and SiC devices

A battery pack with 300 V nominal voltage is considered, with OCV and internal resistance characteristics shown in Figure 5.4. The DC–DC converter is implemented in a boost configuration, allowing the DC-link voltage to be adjusted above the battery terminal voltage. Two types of semiconductors for power electronics are investigated: a Si IGBT module (Infineon FS820R08A6P2B) and a SiC MOSFET module (Wolfspeed CAS300M12BM2). The maximum DC-link voltage is limited to 450 V, determined by the blocking voltage rating of the IGBT module and motor voltage withstand capability, including an additional safety margin to account for transient overvoltage events.

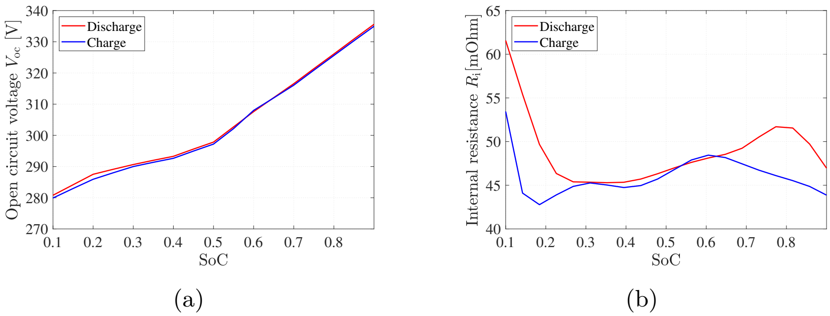

Figure 5.4: *Battery pack data under charge and discharge conditions. (a) OCV. (b) Internal resistance.*

The simulations are carried out in PLECS with a circuit-based model (illustrated in Figure 5.5), capturing detailed power electronics losses based on semiconductor device characteristics obtained from manufacturer datasheets, including conduction voltage drop, on-state resistance, and switching-energy lookup data. To evaluate the energy efficiency improvement enabled by the adjustable DC-link voltage powertrain, a baseline powertrain without a DC–DC converter is used for comparison. The energy consumption is evaluated over WLTC drive cycle.

Optimal DC-link voltage and semiconductor

Table 5.1 summarizes the WLTC drive-cycle energy consumption of the baseline and adjustable DC-link voltage powertrains for both Si-IGBT and SiC-MOSFET implementations at an initial battery state of charge of 80%. The corresponding optimized DC-link voltage trajectories obtained from the DP optimization are illustrated in Figure 5.6.

Table 5.1: Energy consumption of baseline and adjustable DC-link voltage powertrains under the WLTC drive cycle at 80% battery SoC.

Semiconductor	**Baseline powertrain [kWh/100 km]**	**Adjustable DC-link voltage powertrain [kWh/100 km]**
Si-IGBT	19.85	19.62 (-1.16%)
SiC-MOSFET	19.29	18.92 (-1.92%)

It can be observed that the optimal DC-link voltage remains relatively low and is generally

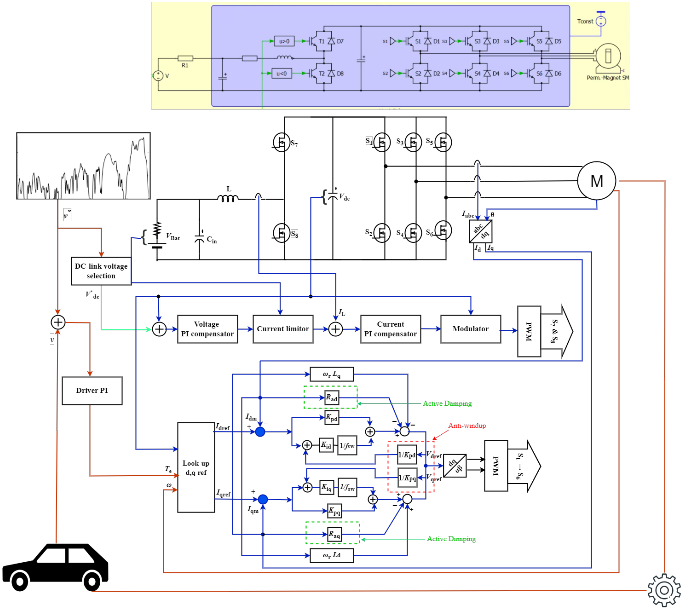

Figure 5.5: *Simulation scheme in PLECS.*

aligned with the battery terminal voltage during low-speed operation. This is expected since the motor operates below its base speed at the battery terminal voltage. In contrast, during high- and extra-high-speed operation, the optimal DC-link voltage reaches its upper bound. During medium-speed operation, the switching and conduction losses are of comparable magnitude, leading to different optimal voltage trajectories for IGBT- and MOSFET-based adjustable DC-link voltage powertrains. The optimal trade-off between loss components therefore depends strongly on the semiconductor characteristics, resulting in distinct optimal DC-link voltage profiles.

For the IGBT-based powertrain, the optimized DC-link voltage reduces the energy consumption from 19.85 to 19.62 kWh/100 km, corresponding to an improvement of 1.16%. A larger benefit is observed for the MOSFET-based powertrain, where the energy consumption decreases from 19.29 to 18.92 kWh/100 km, yielding a reduction of 1.92%. This indicates that the adjustable DC-link voltage offers greater energy-saving potential when combined with SiC devices. A detailed breakdown of the powertrain losses is provided in Figure 5.7. In the IGBT-based adjustable DC-link voltage powertrain, the additional losses introduced by the DC-DC converter still represent a noticeable portion of the total powertrain losses. In contrast, when SiC MOSFETs are employed, similar improvements in electric machine efficiency can be achieved while significantly reducing the power electronic losses. As a result, the additional DC-DC converter losses become comparatively small, enabling the adjustable DC-link voltage powertrain to more effectively realize its energy-saving potential.

Impact of SoC

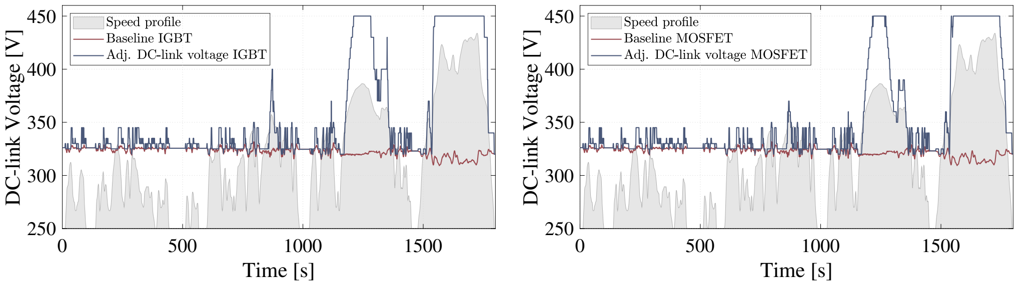

(a)

(b)

Figure 5.6: *Optimized DC-link voltage in adjustable DC-link voltage powertrain compared with DC-link voltage in baseline powertrain. (a) IGBT-based powertrains. (b) MOSFET-based powertrains.*

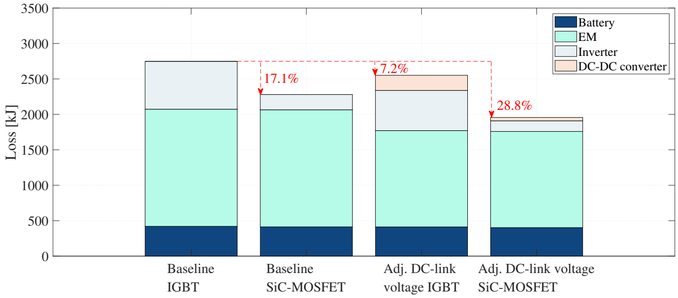

Figure 5.7: *Powertrain loss breakdown.*

The battery OCV varies significantly with the SoC as well as substantial variations in the terminal voltage during drive cycle operation, consequently affecting the overall powertrain efficiency. To capture this effect, simulations are conducted for an initial SoC of 20 %, representing low-SoC operating conditions.

Table 5.2: Energy consumption of baseline and adjustable DC-link voltage powertrains under the WLTC drive cycle at 20% battery SoC.

Semiconductor	**Baseline powertrain [kWh/100 km]**	**Adjustable DC-link voltage powertrain [kWh/100 km]**
Si IGBT	20.28	19.77 (-2.51%)
SiC MOSFET	19.72	19.08 (-3.25%)

Table 5.2 presents the WLTC drive-cycle energy consumption results for the low SoC condition. Compared with the high SoC case (80 %) shown in Table 5.1, the baseline powertrains exhibit an increase in energy consumption of approximately 2.1 % for both IGBT- and MOSFET-based powertrains when the battery SoC decreases to 20 %. In contrast, this efficiency degradation due to reduced battery SoC is significantly mitigated

when an adjustable DC-link voltage is employed. The corresponding increase in energy consumption is limited to approximately 0.8 % for the adjustable DC-link voltage powertrains. This indicates that the adjustable DC-link voltage concept not only improves overall energy efficiency but also reduces the sensitivity of powertrain efficiency to battery SoC variations.

5.3.2 Buck configuration in 900 V system

As modern BEV platforms increasingly adopt high-voltage battery architectures (800 V and above), it becomes important to evaluate the effectiveness of adjustable DC-link voltage powertrains for such systems, particularly the potential benefit of employing a buck converter. In this section, a baseline powertrain supplied directly by a 900 V high-voltage battery is compared with an adjustable DC-link voltage powertrain employing a buck configuration with the same battery. In addition, an adjustable DC-link voltage powertrain using a lower-voltage 400 V battery combined with a boost configuration is also investigated.

The power electronics (with Infineon FS01MR12A8MA2B SiC MOSFET module) and the motor (shown in Figure 5.8) are designed for 900 V nominal DC-link voltage. To enable a fair and systematic comparison, the 400 V and 900 V battery packs are constructed using the same cell, with different numbers of series-connected cells to achieve the desired voltage classes while maintaining realistic pack energy levels representative of modern BEVs. The investigated battery configurations are summarized in Table 5.3.

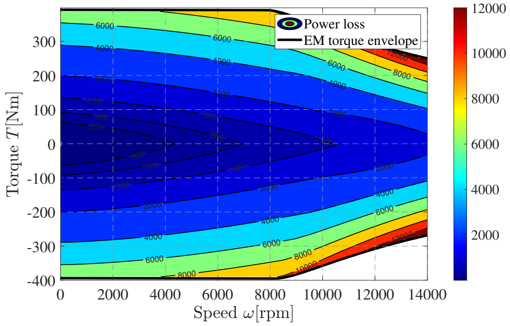

Figure 5.8: *Motor loss map at 900 V DC-link voltage.*

Table 5.3: Investigated battery pack configurations.

Nominal voltage	No. of series cells	No. of parallel strings	Pack energy [kWh]
400 V	107	2	90.0
900 V	241	1	101.4

Table 5.4 summarizes the overall energy consumption over the WLTC drive cycle for the three investigated powertrain configurations. Both adjustable DC-link voltage powertrain with either buck or boost configurations, demonstrate superior energy efficiency compared to the baseline powertrain, achieving energy consumption reductions of 0.64% and 1.02%, respectively.

Table 5.4: WLTC drive-cycle energy consumption of investigated powertrains.

Powertrain	**Battery voltage [V]**	**Energy consumption [kWh/100 km]**
Conventional voltage	900	18.55
Adjustable DC-link voltage powertrain (buck)	900	18.43 (-0.64%)
Adjustable DC-link voltage powertrain (boost)	400	18.36 (-1.02%)

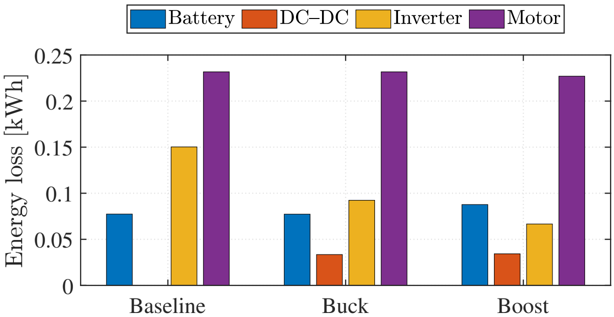

Figure 5.9: *Powertrain loss breakdown over the WLTC drive cycle.*

From the detailed loss breakdown in Figure. 5.9, it can be observed that the motor losses are nearly identical across all three configurations. This is because each configuration is capable of achieving the same maximum DC-link voltage of 900 V, enabling equivalent voltage capability for MTPA region and field-weakening operation at high speeds. In contrast, inverter losses show substantial variation. The baseline powertrain exhibits the highest inverter loss, as the inverter operates continuously at the full 900 V DC-link voltage, leading to increased switching losses. As shown in Figure 5.10, the adjustable DC-link voltage powertrain significantly reduces inverter losses by dynamically lowering the DC-link voltage during operating conditions where high voltage is unnecessary. Since inverter switching loss scales strongly with DC-link voltage, this voltage reduction directly decreases inverter loss. This improvement, however, comes at the cost of additional losses introduced by the DC–DC converter. While both buck and boost configurations incur converter losses, these losses are outweighed by the reduction in inverter losses achieved through DC-link voltage optimization. It is also observed that the baseline powertrain and adjustable DC-link voltage powertrain with buck configurations exhibit slightly lower battery losses, as they operate at higher battery voltages, resulting in lower battery current and consequently reduced ohmic losses.

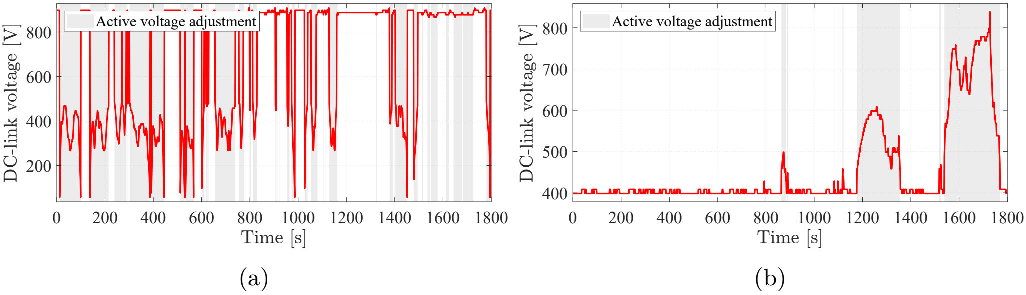

Figure 5.10: *Optimized DC-link voltage over the WLTC drive cycle. (a) Buck configuration (with minimum 50 V DC-link voltage). (b) Boost configuration.*

5.3.3 Summary

This chapter investigated the effectiveness of adjustable DC-link voltage as a system-level approach for improving powertrain energy efficiency. By decoupling the DC-link voltage from the battery terminal voltage, the proposed powertrain enables dynamic voltage adjustment over a wide range of operating conditions, thereby enhancing overall efficiency.

The results further demonstrate that the efficiency benefits of adjustable DC-link voltage are more pronounced when SiC-MOSFET semiconductors are employed. Their lower switching and conduction losses allow the advantages of voltage optimization to be more fully exploited compared with Si-IGBT-based implementations. In addition, the proposed powertrain reduces the sensitivity of energy efficiency to battery SoC variations, enabling more consistent energy consumption under low-SoC conditions.

The analysis also indicates that the concept remains beneficial for higher-voltage powertrain architectures. For systems designed with a nominal DC-link voltage of 900 V, a buck configuration enables dynamic voltage reduction during low- and medium-speed operation, thereby mitigating excessive inverter switching losses without compromising high-speed performance. From an energy-efficiency perspective, however, the results suggest that a lower-voltage battery combined with a boost configuration can achieve superior efficiency when system-level constraints such as fast-charging requirements or component voltage limitations are not dominant.

6 Powertrain Torque Modulation

This chapter is based on the work presented in Paper IV. The objective of this chapter is to develop a torque modulation strategy that alternates the powertrain torque demand for improving powertrain energy efficiency.

6.1 Operating principle

EDUs can achieve high peak efficiency at their optimal operating point. However, this efficiency is not uniform over the full speed–torque operating range [120, 121]. In practice, motors and inverters often operate less efficiently at low torque demand [122, 123], as illustrated in Figure 6.1.

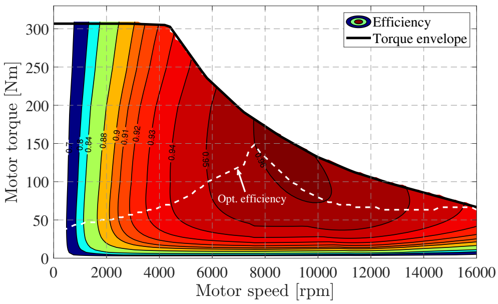

Figure 6.1: *Combined efficiency map of inverter and motor assembly.*

One approach to mitigate this issue is to avoid continuous operation at inefficient low-torque operating points. Torque modulation addresses this by replacing a low torque demand with a pulsating torque command that alternates between zero torque and a higher torque level while preserving the same average delivered torque. By doing so, the EDU can operate in a more efficient region of the torque–speed plane and thereby avoid the low-efficiency zone. As depicted in Figure 6.2, the desired torque demand is modulated into a pattern of alternating between zero and a higher amplitude at a specific modulation frequency, denoted as f_{mod}. Within each modulation period, T_{mod}, the on-state torque, T_{on} lasts for a certain duration, t_{on}, followed by the off-state when the inverter is switched off below base speed. To maintain the same averaged output torque, the relation between the raw torque demand and the modulated torque can be described as

$$T_{\text{dem}} = \frac{t_{\text{on}}}{T_{\text{mod}}} T_{\text{on}} = D T_{\text{on}}. \tag{6.1}$$

where D is the modulation duty cycle which is defined as $\frac{t_{\text{on}}}{T_{\text{mod}}}$.

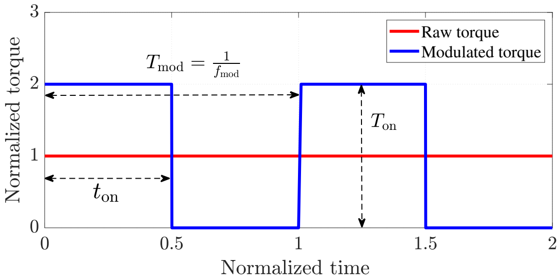

Figure 6.2: *Illustration of torque modulation with a duty cycle of 0.5.*

From an overall powertrain perspective, each component might exhibit distinct loss characteristics in response to such an operation, which is described in the following.

IPMSM

The torque generated by an IPMSM consists of magnetic torque and reluctance torque which are linear and quadratic functions of the stator current according to (2.12) and the resistive copper losses in the motor windings quadratically increase with the stator currents as (2.16). This suggests that the torque modulation will increase the motor copper losses by a factor of $(\frac{1}{D})^2 \cdot D = \frac{1}{D}$ compared to the no-modulation case for the linear term in (2.12). In contrast, for the quadratic term of (2.12), the copper loss remains unchanged with torque modulation $((\frac{1}{\sqrt{D}}^2) \cdot D = 1)$. As a result, it can be concluded that the total copper losses of the motor are increased with torque modulation. However, the iron losses can be reduced when the inverter is switched off, as the magnetic excitation approaches a sinusoidal waveform and the additional harmonic components introduced by PWM switching are eliminated [124]. In the low torque region where the iron losses are more dominant (shown in Figure 6.3), the overall loss of the IPMSM can be reduced with the torque modulation.

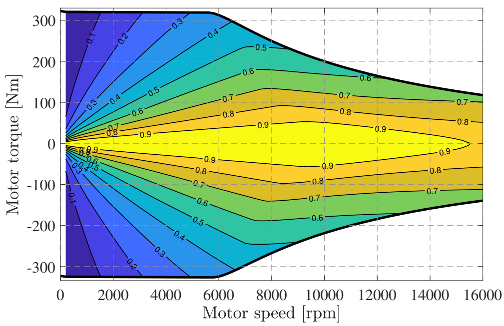

Figure 6.3: *Relative proportion of iron losses to the sum of iron and copper losses.*

Inverter

The inverter losses mainly consist of conduction losses and switching losses, as described in Section 2.1.2. These losses can be represented by a quadratic term and linear terms with respect to the current. Similar to the motor copper losses, the quadratic loss component increases with torque modulation, whereas the linear loss components, including the conduction loss caused by voltage drop and the switching loss, may decrease.

Battery

Battery losses are primarily resistive and scale with the square of the current. Consequently, higher instantaneous current resulting from torque modulation can lead to increased battery losses.

Transmission

The transmission achieves higher efficiency at higher torque demands as illustrated in Figure 6.4, which means the transmission losses can be reduced with the torque modulation.

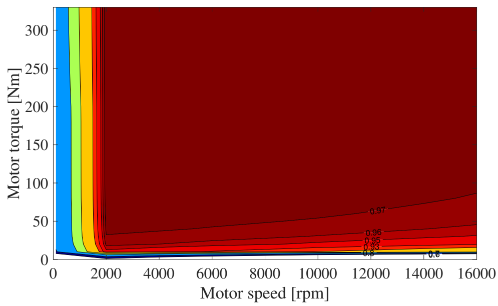

Figure 6.4: *Transmission efficiency map.*

6.2 Optimal modulation strategy

6.2.1 Modulation duty cycle

The modulation duty cycle for each operating point (in reference to unmodulated torque demand) should be determined by considering the losses of the entire powertrain, including the battery, inverter, motor, and transmission.

Modulation with single motor

For powertrain consisting one set of EDU, the overall powertrain loss during one torque modulation period consists of the losses occurring during both the on-state and the off-state, which can be expressed as

$$P_{\mathrm{loss}} = \frac{\overbrace{\int_{0}^{DT_{\mathrm{mod}}} \left(P_{\mathrm{EDU,loss}}\left(\omega, \frac{T_{\mathrm{dem}}}{D}\right) + P_{\mathrm{bat,loss}} \right) dt}^{\text{On-state}} + \overbrace{\int_{DT_{\mathrm{mod}}}^{T_{\mathrm{mod}}} P_{\mathrm{EDU,no\text{-}load}}(\omega)\, dt}^{\text{Off-state}}}{T_{\mathrm{mod}}}, \tag{6.2}$$

where $P_{\mathrm{EDU,no\text{-}load}}$ is the EDU loss during the off-state.

To capture the dynamic and transient battery behavior under high-frequency pulsating current, a first-order RC equivalent circuit model is adopted to represent the battery operation, which is influenced by the pulsating loads induced by torque modulation. For the purpose of analytical loss estimation, the battery ohmic loss can be approximated using a simplified resistive representation as

$$P_{\mathrm{bat}} = 0.8 \cdot I_{\mathrm{bat}}^2 \cdot (R_0 + R_1), \tag{6.3}$$

where I_{bat} is the DC current and R_1 represents the resistance associated with the RC branch. This simplified representation is used to reduce the complexity of the analytical formulation. As reported in [125], a pure resistive model tends to overestimate battery losses by up to 20% compared with the full first-order RC model used in powertrain simulations. Therefore, a correction factor of 0.8 is introduced. The battery losses can be further expressed as

$$P_{\mathrm{bat,loss}} = 0.8 \left(\frac{P_{\mathrm{bat}}}{V_{\mathrm{bat}}} \right)^2 (R_0 + R_1) = 0.8 \left[\frac{\frac{2\pi}{60}\omega \frac{T_{\mathrm{dem}}}{D} + P_{\mathrm{EDU,loss}}\left(\omega, \frac{T_{\mathrm{dem}}}{D}\right)}{V_{\mathrm{bat}}} \right]^2 (R_0 + R_1). \tag{6.4}$$

It is worth noting that the nominal values of V_{bat}, R_0 and R_1 are used in the calculation with their dependency on the battery loading and SoC neglected for simplification. By combining (6.2) and (6.4), the overall powertrain losses of the single-motor powertrain with torque modulation technique can be simplified to

$$
\begin{aligned}
P_{\text{loss}} = D\,P_{\text{EDU,loss}}\left(\omega, \frac{T_{\text{dem}}}{D}\right) + 0.8D\left[\frac{\frac{2\pi}{60}\omega\frac{T_{\text{dem}}}{D} + P_{\text{EDU,loss}}\left(\omega, \frac{T_{\text{dem}}}{D}\right)}{V_{\text{bat}}}\right]^2 (R_0 + R_1) \\
+ (1 - D)P_{\text{EDU,no-load}}(\omega).
\end{aligned}
\tag{6.5}
$$

Finally, for each powertrain operating point, the optimization problem that minimizes the overall powertrain loss with regard to the optimal torque modulation duty cycle can be generalized as

$$
\begin{aligned}
\min_{D} \quad & P_{\text{loss}}(D), \\
\text{s.t.} \quad & 0 \leq D \leq 1, \\
& 0 \leq \omega \leq \omega_b, \\
& T_{\min}(\omega) \leq \frac{T_{\text{dem}}}{D} \leq T_{\max}(\omega),
\end{aligned}
\tag{6.6}
$$

where ω_b is the motor base speed. To find the optimal duty cycle for each powertrain operating point of ω and T_{dem}, a grid-search-based method is employed.

Modulation with dual motors

The implementation of the torque modulation in a dual-motor powertrain should ensure complementary on- and off-states between the two motors. That is, when one motor is in the on-state, the other should be in the off-state to prevent superimposed high powertrain torque outputs and intermittent battery currents and, thereby, avoid increased battery losses and deteriorated driver comfort. This requires complementary torque modulation PWM waveforms used for the front and rear motor. Depending on the modulation duty cycle of the front and rear motor (denoted as D_f and D_r, respectively), three different scenarios can occur as illustrated in Figure 6.5.

In Scenario I, where the sum of D_f and D_r is smaller than one, the front and rear motor have complementary on-state timings with a torque blanking time between the respective on-states. Scenario II represents a specific scenario where the sum of the front and rear modulation duty cycles is exactly one, meaning that there is no torque blanking time from the powertrain. In addition, if both D_f and D_r are equal to 0.5, the front and rear motor have perfectly complementary modulation so that there is no torque fluctuation from the powertrain. While in Scenario III, where the sum of D_f and D_r, is bigger than one, an overlapped modulation time occurs and both front and rear motors are simultaneously operating at on-state, resulting in a high torque output from the powertrain. This also leads to superimposed battery currents, hence amplified battery losses.

The overall powertrain losses of a dual-motor powertrain with the torque modulation

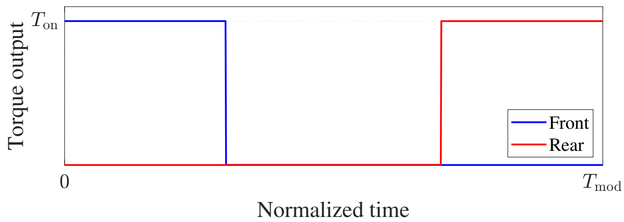

(a)

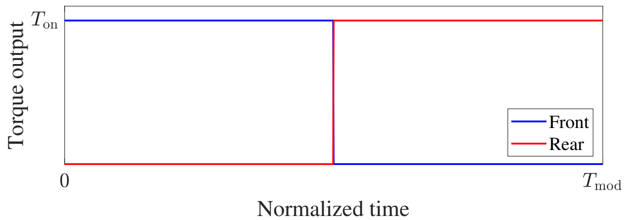

(b)

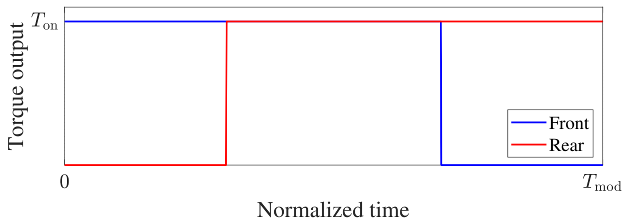

(c)

Figure 6.5: *Possible scenarios of torque modulation in a dual-motor powertrain. (a) Scenario I: $D_f + D_r < 1$. (b) Scenario II: $D_f + D_r = 1$. (c) Scenario III: $D_f + D_r > 1$.*

consist of the losses occurring during on- and off-states for the identical front and rear EDUs as

$$
\begin{aligned}
P_{\mathrm{loss}} &= \frac{1}{T_{\mathrm{mod}}}\left[\int_0^{D_f T_{\mathrm{mod}}} P_{\mathrm{EDU,loss}}(\omega, T_f)\, dt + \int_{D_f T_{\mathrm{mod}}}^{T_{\mathrm{mod}}} P_{\mathrm{EDU,no\text{-}load}}(\omega)\, dt \right.\\
&\quad \left. + \int_0^{D_r T_{\mathrm{mod}}} P_{\mathrm{EDU,loss}}(\omega, T_r)\, dt + \int_{D_r T_{\mathrm{mod}}}^{T_{\mathrm{mod}}} P_{\mathrm{EDU,no\text{-}load}}(\omega)\, dt \right] + P_{\mathrm{bat,loss}}\\
&= D_f T_{\mathrm{mod}} P_{\mathrm{EDU,loss}}(\omega, T_f) + (2 - D_f - D_r) P_{\mathrm{EDU,no\text{-}load}}(\omega) + D_r T_{\mathrm{mod}} P_{\mathrm{EDU,loss}}(\omega, T_r)\\
&\quad + P_{\mathrm{bat,loss}},
\end{aligned}
\tag{6.7}
$$

where T_f and T_r are the on-torque of front and rear EDU, respectively. Based on the three scenarios, the battery loss can be further expressed as

$$
\begin{aligned}
&\text{if } D_f + D_r \leq 1: \\
&P_{\text{bat,loss}} = 0.8 \left[D_f \left(\frac{\frac{2\pi}{60}\omega T_f + P_{\text{EDU,loss}}(\omega, T_f)}{V_{\text{bat}}} \right)^2 \right. \\
&\qquad \left. + D_r \left(\frac{\frac{2\pi}{60}\omega T_r + P_{\text{EDU,loss}}(\omega, T_r)}{V_{\text{bat}}} \right)^2 \right] (R_0 + R_1), \\
&\text{if } D_f + D_r > 1: \\
&P_{\text{bat,loss}} = 0.8 \left[(1 - D_r) \left(\frac{\frac{2\pi}{60}\omega T_f + P_{\text{EDU,loss}}(\omega, T_f)}{V_{\text{bat}}} \right)^2 \right. \\
&\qquad + (1 - D_f) \left(\frac{\frac{2\pi}{60}\omega T_r + P_{\text{EDU,loss}}(\omega, T_r)}{V_{\text{bat}}} \right)^2 \\
&\qquad + \left(\frac{\frac{2\pi}{60}\omega (T_f + T_r) + P_{\text{EDU,loss}}(\omega, T_f) + P_{\text{EDU,loss}}(\omega, T_r)}{V_{\text{bat}}} \right)^2 \\
&\qquad \left. (D_f + D_r - 1) \right] (R_0 + R_1)
\end{aligned}
\tag{6.8}
$$

Thus, the optimization problem can be formulated as

$$
\begin{aligned}
\min_{D_f, D_r, T_f, T_r} \quad & P_{\text{loss}}(D_f, D_r, T_f, T_r), \\
\text{s.t.} \quad & 0 \leq D_f \leq 1, \\
& 0 \leq D_r \leq 1, \\
& 0 \leq \omega \leq \omega_b, \\
& T_{\min}(\omega) \leq T_f \leq T_{\max}(\omega), \\
& T_{\min}(\omega) \leq T_r \leq T_{\max}(\omega), \\
& D_f T_f + D_r T_r = T_{\text{dem}}.
\end{aligned}
\tag{6.9}
$$

The cost function for the dual motor powertrain (6.7) involves more variables with conditional expressions associated with battery loss (6.8), therefore PSO algorithm is used for identifying the optimal D_f, D_r, T_f and T_r for each powertrain operating point.

6.2.2 Modulation frequency

The torque modulation frequency is constrained within specific upper and lower limits. On one hand, this frequency must not surpass the motor torque response time to ensure enough time for the motor to reach the desired T_{on} within the on-state duration, t_{on}. On the other hand, an excessively low modulation frequency should be avoided, as it may lead to discernible pulsating torque output which could potentially compromise driver comfort.

Upper limit

The motor torque response time is closely related to the performance of the current control loop. In this study, two commonly used current control strategies are considered: a proportional–integral (PI)-based current control and a deadbeat control. With an inverter switching frequency of $f_{sw} = 10\,\text{kHz}$ and an equal sampling frequency of $f_s = 10\,\text{kHz}$, the resulting current control bandwidth is approximately 1000 rad/s. Accordingly, the time constant for the torque response is $\tau = 0.001\,\text{s}$ [126]. For a PI-based current control, the torque response time (from 0% to 98.2% of the target value) can therefore be estimated as

$$t_{\text{resp,PI}} = 4\tau = 0.004s \tag{6.10}$$

The deadbeat control serves as a promising alternative to be applied along with the torque modulation, since it calculates control actions at each sampling instant to reach the desired setpoint in minimal steps. Therefore, it pushes the torque response time of the discrete-time system to the limit set by the inverter switching frequency [126, 127], achieving a much faster torque response time as

$$t_{\text{resp,DB}} = \frac{1}{f_{\text{sw}}} = 0.001s \tag{6.11}$$

Figure 6.6 illustrates the torque and three-phase current response with the two current control methods.

Therefore, the theoretical maximum torque modulation frequencies for ensuring the motor has sufficient time to reach T_{on} within one modulation period T_{mod} for the PI controller and deadbeat controller are 250 Hz and 1000 Hz, respectively. However, since the on-state duration t_{on} can be significantly shorter than the duration of one modulation period T_{mod} in the case of a low modulation duty cycle, and the desired T_{on} needs to last for an adequate duration to effectively utilize the torque modulation strategy, it is advisable to keep the torque response time within 10% of one modulation period. Therefore, an appropriate upper limit for the modulation frequency can be determined as 25 Hz for the PI controller and 100 Hz for the deadbeat controller.

Lower limit

A low torque modulation frequency may result in perceptible driver discomfort due to the pulsating torque output. Therefore, the lower limit of the modulation

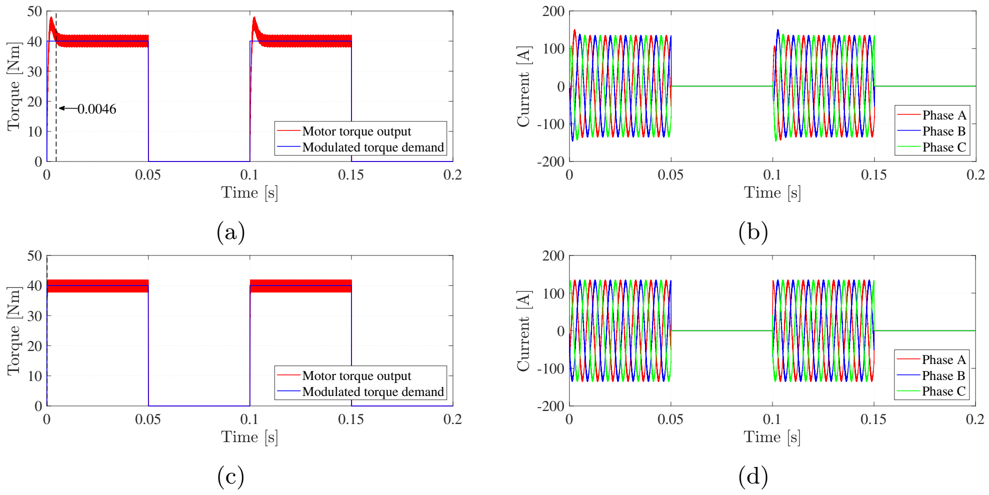

Figure 6.6: *Illustration of torque and three-phase current response. (a) Motor torque response with PI control. (b) Phase currents with PI control. (c) Motor torque response with deadbeat control. (d) Phase currents with deadbeat control.*

frequency is governed by the threshold of the driver discomfort which depends on both the torque amplitude, T_{on}, and the modulation frequency, f_{mod}. The discomfort level can be quantified using vibration total value (VTV) according to ISO2631-1, which indicates the potential impact of vibrations on human discomfort by considering factors such as the magnitude of the vibration, its frequency, the direction of vibration, as well as the duration of exposure. The ISO2631-1 also lists the reference values used to assess the discomfort level as given in Table 6.1.

Table 6.1: Approximate indications of likely reactions to various VTVs.

VTV [m/s^2]	**Comfort level**
Less than 0.315	Not uncomfortable
0.315 - 0.63	A little uncomfortable
0.5 - 1	Fairly uncomfortable
0.8 - 1.6	Uncomfortable
1.25 - 2.5	Very uncomfortable
Greater than 2	Extremely uncomfortable

The frequency-weighted Root-Mean-Square (RMS) acceleration, a_w, can be derived as

$$a_w = \sqrt{\sum_i (w_i a_i)^2} \tag{6.12}$$

where a_i is the RMS acceleration for the corresponding frequency and w_i is the weighting factor for each frequency, as shown in Figure 6.7.

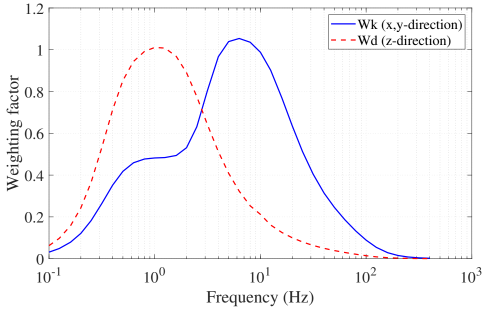

Figure 6.7: *ISO2631 frequency weighting curves.*

The VTV combines the vibration in all directions and is then assessed at the vehicle center of gravity as

$$a_v = \sqrt{k_x^2 a_{wx}^2 + k_y^2 a_{wy}^2 + k_z^2 a_{wz}^2} \tag{6.13}$$

where a_{wx}, a_{wy}, a_{wz} are the frequency-weighted RMS accelerations with respect to the orthogonal axes x, y and z, respectively; k_x, k_y, k_z are the weighing factors.

6.3 Results and discussion

6.3.1 Optimal modulation duty cycle

The studied EDU efficiency characteristics are illustrated in Figure 6.1 and Figure 6.4. The optimal modulation duty cycle for the single-motor powertrain, adopting one EDU, is illustrated in Figure 6.8.

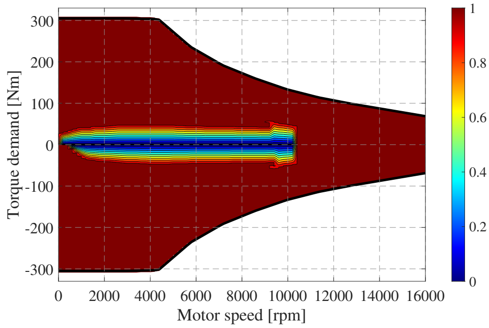

Figure 6.8: *Optimal modulation duty cycle of the single-motor powertrain.*

For the dual-motor powertrain, two identical EDUs are employed in FRID configuration. Due to system symmetry, the optimal modulation duty cycle yields $D_f = D_r$ and $T_f = T_r$ for all the operating points. Hence, for the dual-motor powertrain, the optimal modulation duty cycle can be expressed as $D_f = D_r = D_{\text{opt}}$ and $T_f = T_r = \frac{T_{\text{dem}}}{2D_{\text{opt}}}$. Figure 6.9 shows the optimal modulation duty cycle (D_{opt}) for both front and rear motors. Compared to the single-motor powertrain, the effective area of the torque modulation is expanded. The powertrain operates predominantly as in Scenario I in the low torque demand area. In contrast, in areas characterized by low speed but medium torque demand, Scenario III becomes the preferred mode of operation with reduced overall powertrain loss despite an increase in the battery loss. Notably, as the operating speed increases, the optimal modulation duty cycle is limited to a maximum of 0.5 (as in Scenario II) since the excessive battery losses caused by the superimposed battery current becomes significant within the powertrain.

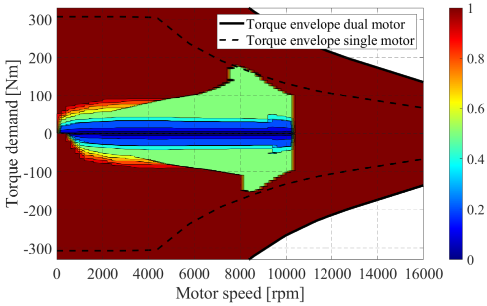

Figure 6.9: *Optimal modulation duty cycle of the dual-motor powertrain with* $T_f = T_r = \frac{T_{dem}}{2D}$.

6.3.2 Driver comfort

A full vehicle model of the considered vehicle is utilized in IPG CarMaker to calculate the body acceleration caused by the pulsating torque output from the powertrain, including effects such as suspension damping and powertrain torsional stiffness. The VTV is calculated and mapped across the entire powertrain operating range within the effective torque modulation area, following the procedure illustrated in Figure 6.10. For each operating point, the vehicle is initialized at the corresponding speed in the simulation setup. The torque demand is then modulated based on the optimal modulation duty cycle. The resulting body acceleration at the vehicle's center of gravity in the longitudinal (x) and vertical (z) accelerations are logged. Fast fourier transformation (FFT) is then applied for deriving the VTV according to (6.13).

The resulting VTV values are mapped over the entire powertrain operating region and are presented in Figure 6.11. As expected, increasing the modulation frequency leads to a reduction in the overall VTV values due to the diminished amplitude of

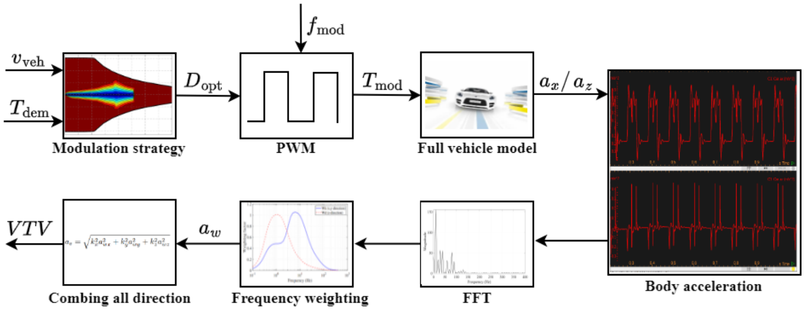

Figure 6.10: *Calculation procedure of VTV value.*

low-frequency torque pulsations transmitted to the vehicle body. Furthermore, the dual-motor configuration consistently exhibits lower VTV values than the single-motor powertrain for the same powertrain operating point due to complementary operation.

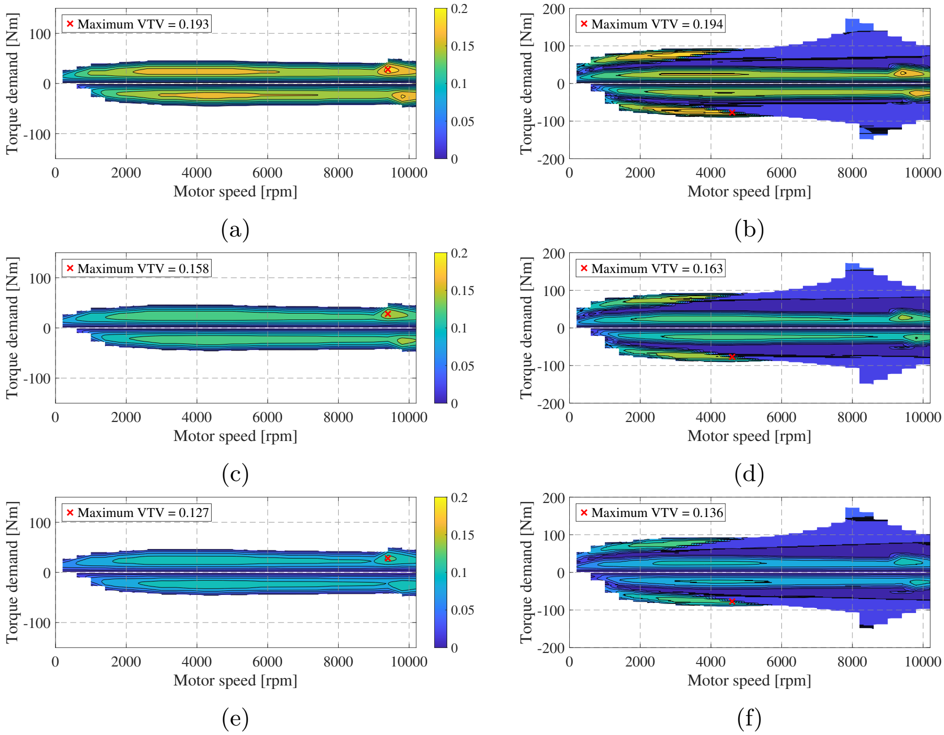

Figure 6.11: *VTV values of single- and dual-motor powertrains with optimal modulation duty cycle at different torque modulation frequencies. (a), (c), and (e) correspond to the single-motor powertrain at* 10 Hz, 15 Hz, *and* 20 Hz, *respectively. (b), (d), and (f) correspond to the dual-motor powertrain at* 10 Hz, 15 Hz, *and* 20 Hz, *respectively.*

In regions where the torque modulation strategy operates under Scenario III, characterized by overlapping on-states of the front and rear motors, the VTV values reach their peak. Nevertheless, these values remain below the threshold of perceived discomfort. In contrast, when the strategy operates under Scenario II, corresponding to perfectly complementary on- and off-states of the two motors, the modulation-induced vibration becomes almost negligible.

Overall, the results indicate that increasing the modulation frequency improves vibration comfort; however, even at a relatively low modulation frequency of 10 Hz, the perceived discomfort is effectively eliminated for both single- and dual-motor powertrains.

6.3.3 Efficiency improvement

To demonstrate the energy efficiency improvement achieved through torque modulation, the WLTC drive-cycle energy consumption is evaluated for both powertrain configurations and compared against regular operation without torque modulation, based on the vehicle parameters specified in Table 3.2. The energy consumption results are summarized in Table 6.2. It can be observed that the application of torque modulation effectively reduces energy consumption for both configurations.

Table 6.2: WLTC drive-cycle energy consumption of single- and dual-motor powertrains.

Powertrain configuration	**No modulation [kWh/100 km]**	**Torque modulation [kWh/100 km]**
Single-motor	19.68	19.47 (-1.05%)
Dualmotor	20.78	20.32 (-2.21%)

Note: Results obtained with a torque modulation frequency of 20 Hz and PI current control.

Figure 6.12 presents the detailed loss breakdown of the powertrain components. For the single-motor powertrain, torque modulation leads to noticeable reductions in inverter, motor, and transmission losses due to improved operation within higher efficiency regions. However, the pulsating current associated with torque modulation introduces additional battery loss. Nevertheless, a net reduction in total powertrain loss is achieved.

A similar trend is observed for the dual-motor powertrain. Despite the inherently higher baseline energy consumption caused by additional no-load loss from the second EDU, torque modulation provides a more pronounced reduction in total energy consumption. This improvement can be attributed to two main factors. First, the effective operating region where torque modulation can be applied is significantly expanded in the dual-motor powertrain, as shown in Figure 6.13. Second, the torque demand is shared between two EDUs, enabling each unit to operate at lower torque levels, where the effectiveness of torque modulation increases as the torque demand decreases. As a result, the torque modulation strategy can be utilized more effectively while maintaining an acceptable increase in battery loss. It should be noted that, in the dual-motor powertrain, an operating

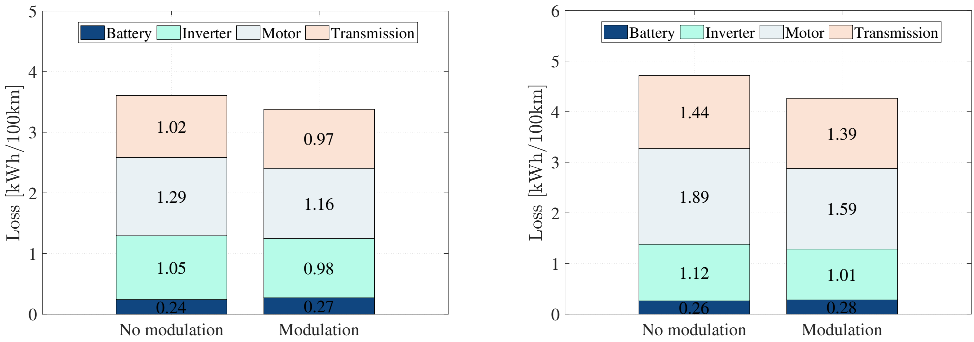

(a) (b)

Figure 6.12: *WLTC drive-cycle losses breakdown. (a) Single-motor powertrain. (b) Dual-motor powertrain.*

condition with a modulation duty cycle of $D = 0.5$ results in operation equivalent to having one inverter completely deactivated while the other EDU delivers the required torque. In this particular case, the effect is similar to single-motor operation without torque modulation. However, the distribution of operating points over the WLTC drive cycle, shown in Figure 6.13, indicates that the powertrain operates outside the $D = 0.5$ regime for most of the cycle duration, where the benefits of torque modulation can be effectively exploited.

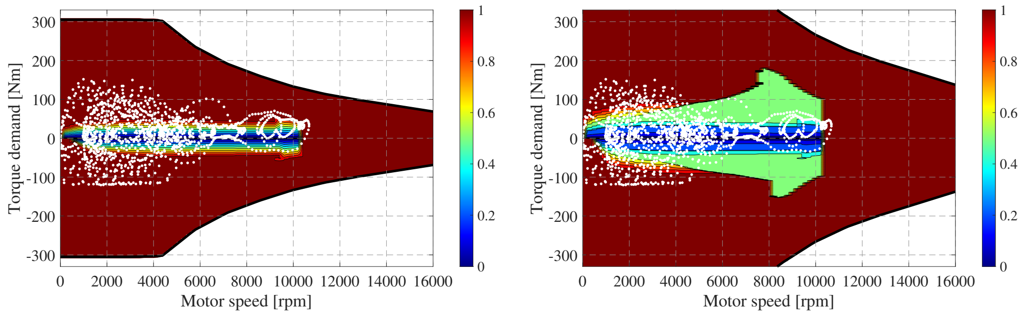

(a) (b)

Figure 6.13: *WLTC drive-cycle powertrain operating points projected on the effective torque modulation area. (a) Single-motor powertrain. (b) Dual-motor powertrain.*

6.3.4 Summary

This chapter investigated the effectiveness of the proposed torque modulation control strategy in improving powertrain energy efficiency. By transforming the raw torque demand into a pulsating torque request under low-to-medium load conditions and below the base speed region, torque modulation enables more efficient operation of the EDU. Although the introduction of pulsating current results in additional battery loss, the reductions in inverter, motor, and transmission losses outweigh this penalty, leading to an overall improvement in system efficiency.

The results further demonstrate that the efficiency benefit of torque modulation is more pronounced when applied to a dual-motor powertrain with FRID configuration. The additional degree of freedom in torque distribution between the two EDUs expands the effective operating region in which torque modulation can be utilized, thereby enhancing the achievable efficiency gains.

Furthermore, the analysis indicates that the potential impact on driver comfort caused by pulsating torque output can be maintained at a negligible level when an appropriate modulation frequency is selected. In dual-motor configurations, the complementary operation of the two EDUs further mitigates perceived drivability disturbances.

7 Energy-Efficient Powertrain Thermal Management

This chapter is based on the work presented in Paper V. The objective of this chapter is to develop an energy-efficient powertrain thermal management strategy that actively regulates the temperatures of powertrain components in order to minimize powertrain losses and the corresponding auxiliary energy consumption associated with the thermal management system.

7.1 Thermal management system

Figure 7.1 illustrates the schematic of the investigated powertrain thermal management system, which comprises interconnected oil and coolant circuits. In the oil circuit, an electric oil pump circulates oil from the sump through the oil cooler. The cooled oil is then delivered to spray channels, where it is injected onto the motor end windings through spray nozzles and subsequently flows into the transmission for lubrication and cooling. Finally, the oil returns to the sump by gravity.

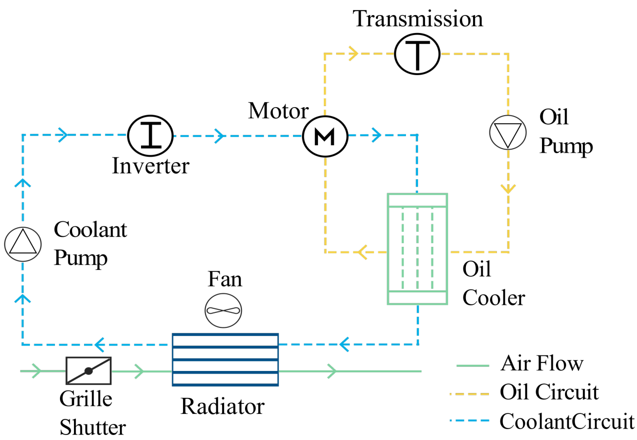

Figure 7.1: *Schematic of the investigated powertrain thermal management system.*

In the coolant circuit, an electric coolant pump circulates a water–glycol mixture (EGL50/50) through the inverter cooling channel, the motor housing water jacket, and the oil cooler. After absorbing heat from these components, the heated coolant flows to the radiator, where thermal energy is dissipated to the ambient air. Airflow through the radiator is regulated by a radiator fan and an active grille shutter (AGS), which improves cooling performance while maintaining aerodynamic efficiency.

7.2 Energy-efficient powertrain thermal management strategy

The goal of powertrain thermal management is to maintain component temperatures within operational limits while ensuring efficient operation in optimal ranges. Conventionally, rule-based strategies assign temperature targets to each component, regulating auxiliary actuators (e.g., pumps and fans) to meet these targets. However, these approaches can result in overly conservative control and excessive energy consumption by auxiliaries. This section introduces an energy-efficient thermal management strategy based on MPC which minimizes energy consumption in both powertrain and auxiliary components.

7.2.1 Problem formulation

Unlike conventional rule-based thermal management strategies that track predefined temperature references, the energy-efficient powertrain thermal management problem is formulated as an OCP. The objective is to minimize the total electrical energy consumption associated with powertrain operation and thermal actuation while satisfying component temperature limits and actuator constraints.

The states of interest correspond to the temperatures at critical locations within the powertrain and thermal management system. The state vector is defined as

$$x = \left[T_{\mathrm{jt}},\ T_{\mathrm{w}},\ T_{\mathrm{pm}},\ T_{\mathrm{ici}},\ T_{\mathrm{ico}},\ T_{\mathrm{emco}},\ T_{\mathrm{emoi}},\ T_{\mathrm{emoo}},\ T_{\mathrm{so}}\right]^{\top}, \tag{7.1}$$

where T_{jt} is the inverter junction temperature, T_{w} is the motor winding temperature, T_{pm} is the permanent magnet temperature, T_{ici} and T_{ico} are the inverter coolant inlet and outlet temperatures, respectively, T_{emco} is the motor coolant outlet temperature, T_{emoi} and T_{emoo} are the motor oil inlet and outlet temperatures, respectively, and T_{so} is the sump oil temperature.

The control variables governing the thermal management system actuation are defined as

$$u = \left[\phi,\ d_{\mathrm{fan}},\ \dot{V}_{\mathrm{c}},\ \dot{V}_{\mathrm{o}}\right], \tag{7.2}$$

where ϕ is the AGS opening angle, d_{fan} is the radiator fan duty cycle, and $\dot{V}_{\mathrm{c}}$ and $\dot{V}_{\mathrm{o}}$ are the coolant and oil volumetric flow rates, respectively.

The nonlinear thermal dynamics governing the temperature evolution of the powertrain components are represented in discrete-time form as

$$x(k+1) = f\big(x(k), u(k)\big), \tag{7.3}$$

where the function $f(\cdot)$ represents the discretized form of powertrain thermal dynamics detailed in Section 7.3. The OCP is formulated over a finite prediction horizon N, which is chosen to be equal to the control horizon, as

$$\begin{aligned}
\min_{u(\cdot)} \quad & \sum_{k=0}^{N} f_0(x(k), u(k)) \\
\text{s.t.} \quad & x(k+1) = f(x(k), u(k)), \\
& x_{\min} \le x(k) \le x_{\max}, \\
& u_{\min} \le u(k) \le u_{\max}, \\
& x(0) = x_0.
\end{aligned} \tag{7.4}$$

The cost function minimizes the total electrical energy drawn from the high-voltage battery over the prediction horizon. To this end, the discrete-time stage cost $f_0(k)$ represents the instantaneous electrical power consumption at time step k and is defined as

$$\begin{aligned}
f_0(k) = {} & \underbrace{P_{\text{trac}}(k)}_{\text{Traction power}} + \underbrace{P_{\text{loss,w}}(k) + P_{\text{loss,pm}}(k) + P_{\text{loss,inv}}(k) + P_{\text{loss,tran}}(k)}_{\text{Powertrain losses}} \\
& + \underbrace{P_{\text{fan}}(k) + P_{\text{pu,c}}(k) + P_{\text{pu,o}}(k)}_{\text{Cooling power}}.
\end{aligned} \tag{7.5}$$

where P_{trac} denotes the mechanical traction power demand, influenced by the AGS angle ϕ through aerodynamic drag. Positive values of P_{trac} indicate propulsion, where minimization reduces the electrical energy required from the battery. Negative values correspond to regenerative braking, and minimizing this term promotes maximization of the recovered electrical energy through regeneration. $P_{\text{loss,w}}$ represents the lumped motor loss at the winding node, $P_{\text{loss,pm}}$ the lumped loss at the magnet node, and $P_{\text{loss,tran}}$ the transmission power loss. Furthermore, P_{fan} denotes the electrical power consumption of the radiator fan, while $P_{\text{pu,c}}$ and $P_{\text{pu,o}}$ represent the coolant and oil pump power consumption, respectively.

The optimization is subject to physical and safety constraints on both the system states and control inputs. The temperature limits of the critical powertrain components are imposed as

$$T_{\mathrm{w}} \leq 180\,^{\circ}\mathrm{C}, \tag{7.6}$$
$$T_{\mathrm{pm}} \leq 140\,^{\circ}\mathrm{C}, \tag{7.7}$$
$$T_{\mathrm{jt}} \leq 150\,^{\circ}\mathrm{C}, \tag{7.8}$$

while the coolant and oil temperatures are constrained within the admissible operating range to avoid fluid phase changes and ensure proper thermal performance

$$-20 \leq T_{\mathrm{c}} \leq 100\,^{\circ}\mathrm{C}, \tag{7.9}$$
$$-20 \leq T_{\mathrm{o}} \leq 100\,^{\circ}\mathrm{C}. \tag{7.10}$$

In addition, the control inputs are bounded by actuator and system limitations

$$0 \leq \phi \leq 90^{\circ}, \tag{7.11}$$
$$0 \leq d_{\mathrm{fan}} \leq 100\,\%, \tag{7.12}$$
$$2\,\mathrm{L\,min^{-1}} \leq \dot{V}_{\mathrm{c}} \leq 18\,\mathrm{L\,min^{-1}}, \tag{7.13}$$
$$1\,\mathrm{L\,min^{-1}} \leq \dot{V}_{\mathrm{o}} \leq 18\,\mathrm{L\,min^{-1}}. \tag{7.14}$$

The AGS angle is restricted to 0°- 90°, representing fully closed and fully open positions, respectively. The fan is regulated via a PWM duty cycle, constrained between 0 % and 100 %. The coolant flow rate is bounded between $2\,\mathrm{L\,min^{-1}}$ and $18\,\mathrm{L\,min^{-1}}$, whereas the oil flow rate ranges from $1\,\mathrm{L\,min^{-1}}$ to $18\,\mathrm{L\,min^{-1}}$, ensuring maintenance of idle flow.

7.2.2 MPC setup

The energy-efficient thermal management OCP is solved in a receding-horizon framework using MPC. At each control update, the OCP defined in (4.14) is solved over a finite prediction horizon using the latest available preview of the vehicle speed profile. A discretization step of $\Delta t = 1$ s is adopted, which is sufficient to capture the dominant thermal dynamics while maintaining computational tractability. The prediction horizon is set to $N = 10$, corresponding to a preview duration of 10 s.

For the considered thermal management strategy, the OCP is formulated as a continuous NLP problem since all control inputs (e.g., coolant flow rate, pump/fan actuation) are continuous. The resulting NLP is solved using a sequential quadratic programming (SQP) method, which is well suited for smooth nonlinear optimal control problems with constraints and enables fast convergence in receding-horizon applications.

To improve computational efficiency in the receding-horizon implementation, a warm-start strategy is employed.

7.3 Control-oriented model

A control-oriented model is developed to capture the thermal dynamics of the powertrain components, cooling auxiliaries, and temperature-dependent loss characteristics. This model provides a computationally efficient representation of the coupled thermal–electrical behavior of the system and is used for the formulation and real-time solution of the OCP underlying the proposed energy-efficient powertrain thermal management strategy. For compactness, a function of multiple variables is denoted as $(\cdot)$ and fitted coefficients are represented by α and β.

7.3.1 Thermal model

Inverter

Figure 7.2 illustrates the inverter geometry together with the corresponding reduced-order lumped-parameter thermal network (LPTN) [128, 129].

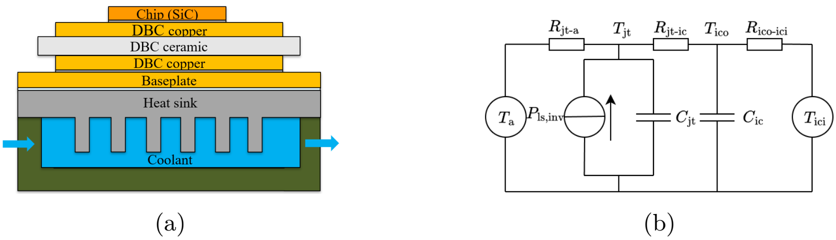

Figure 7.2: *Inverter cooling system and thermal model. (a) Geometry. (b) Reduced-order LPTN representation.*

For simplicity, the inverter loss power is applied to a single junction node representing the average temperature of the semiconductor devices. The generated heat is rejected to the coolant through convection and to the surrounding air in the powertrain compartment, which is assumed to be at ambient temperature T_{a}. The thermal dynamics of the junction temperature T_{jt} and inverter coolant outlet temperature T_{ico} are described as

$$\frac{dT_{\text{jt}}}{dt} = \frac{1}{C_{\text{jt}}}\left(P_{\text{loss,inv}} - \frac{T_{\text{jt}} - T_{\text{ico}}}{R_{\text{jt-c}}} - \frac{T_{\text{jt}} - T_{\text{a}}}{R_{\text{jt-a}}}\right), \tag{7.15}$$

$$\frac{dT_{\text{ico}}}{dt} = \frac{1}{C_{\text{ico}}} \left(\frac{T_{\text{jt}} - T_{\text{ico}}}{R_{\text{jt-c}}} - \frac{T_{\text{ico}} - T_{\text{ici}}}{R_{\text{ico-ici}}} \right), \tag{7.16}$$

where C_{jt} and C_{ico} denote the thermal capacitances of the junction and inverter coolant outlet nodes, respectively, $R_{\text{jt-c}}$ is the thermal resistance between the semiconductor junction and the coolant, $R_{\text{jt-a}}$ is the thermal resistance between the junction and the ambient air, and $R_{\text{ico-ici}}$ is the thermal resistance associated with heat transfer between the inverter coolant outlet and inlet.

The thermal resistances associated with convective heat transfer to the coolant, $R_{\text{jt-c}}$ and $R_{\text{ico-ici}}$, depend on the coolant volumetric flow rate $\dot{V}_{\text{c}}$. Following the simplified formulation proposed by Semikron [130], the flow-rate-dependent thermal resistance is modeled as

$$R = R_{\text{ref}} \left(\frac{\dot{V}_{\text{c}}}{\dot{V}_{\text{ref}}} \right)^{\beta}, \tag{7.17}$$

where R_{ref} is the reference thermal resistance at the reference flow rate $\dot{V}_{\text{ref}}$.

IPMSM

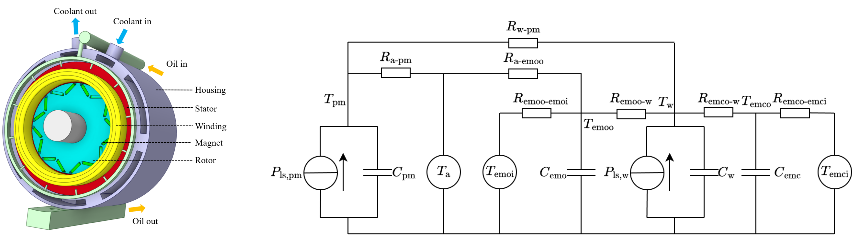

(a) (b)

Figure 7.3: *Motor cooling system and thermal model. (a) Geometry. (b) Reduced-order LPTN representation.*

Figure 7.3 illustrates the motor geometry and the corresponding reduced-order LPTN. Due to the high level of abstraction, the stator and winding losses are aggregated into a single heat source $P_{\text{loss,w}}$ applied at the winding node. Similarly, rotor and permanent magnet losses are combined into a single heat source $P_{\text{loss,pm}}$ applied at the magnet node. The thermal dynamics are described as

$$\frac{dT_{\mathrm{w}}}{dt} = \frac{1}{C_{\mathrm{w}}} \left(P_{\mathrm{loss,w}} - \frac{T_{\mathrm{w}} - T_{\mathrm{emco}}}{R_{\mathrm{emco\text{-}w}}} - \frac{T_{\mathrm{w}} - T_{\mathrm{pm}}}{R_{\mathrm{w\text{-}pm}}} - \frac{T_{\mathrm{w}} - T_{\mathrm{emoo}}}{R_{\mathrm{emoo\text{-}w}}} \right), \tag{7.18}$$

$$\frac{dT_{\mathrm{pm}}}{dt} = \frac{1}{C_{\mathrm{pm}}} \left(P_{\mathrm{loss,pm}} + \frac{T_{\mathrm{w}} - T_{\mathrm{pm}}}{R_{\mathrm{w\text{-}pm}}} + \frac{T_{\mathrm{a}} - T_{\mathrm{pm}}}{R_{\mathrm{a\text{-}pm}}} \right), \tag{7.19}$$

$$\frac{dT_{\mathrm{emco}}}{dt} = \frac{1}{C_{\mathrm{emc}}} \left(\frac{T_{\mathrm{w}} - T_{\mathrm{emco}}}{R_{\mathrm{emco\text{-}w}}} - \frac{T_{\mathrm{emco}} - T_{\mathrm{emci}}}{R_{\mathrm{emco\text{-}emci}}} \right), \tag{7.20}$$

$$\frac{dT_{\mathrm{emoo}}}{dt} = \frac{1}{C_{\mathrm{emo}}} \left(\frac{T_{\mathrm{w}} - T_{\mathrm{emoo}}}{R_{\mathrm{emoo\text{-}w}}} - \frac{T_{\mathrm{emoo}} - T_{\mathrm{emoi}}}{R_{\mathrm{emoo\text{-}emoi}}} + \frac{T_{\mathrm{a}} - T_{\mathrm{emoo}}}{R_{\mathrm{a\text{-}emoo}}} \right), \tag{7.21}$$

where C_{w}, C_{pm}, C_{emc}, and C_{emo} denote the thermal capacitances of the winding, permanent magnet, motor coolant, and motor oil nodes, respectively. $R_{\mathrm{w\text{-}pm}}$ is the thermal resistance between the winding and the permanent magnet. $R_{\mathrm{emco\text{-}w}}$ and $R_{\mathrm{emoo\text{-}w}}$ are the thermal resistances between the winding and the motor coolant outlet and motor oil outlet, respectively. $R_{\mathrm{emco\text{-}emci}}$ and $R_{\mathrm{emoo\text{-}emoi}}$ are the thermal resistances between the coolant outlet and inlet, and between the oil outlet and inlet, respectively. $R_{\mathrm{a\text{-}pm}}$ and $R_{\mathrm{a\text{-}emoo}}$ account for the thermal resistances between the ambient and the permanent magnet, and between the ambient and the motor oil outlet, respectively. T_{emci} denote the motor coolant inlet temperature, which is assumed to be the same as the inverter coolant outlet temperature T_{ico}.

The thermal resistances associated with convective heat transfer to coolant and oil, $R_{\mathrm{emco\text{-}w}}$, $R_{\mathrm{emco\text{-}emci}}$, $R_{\mathrm{emoo\text{-}w}}$, and $R_{\mathrm{emoo\text{-}emoi}}$, are modeled according to (7.17), thereby capturing their dependence on the coolant and oil volumetric flow rate.

Transmission

Heat transfer within the transmission occurs through two primary pathways: natural convection to the surrounding air in the powertrain compartment and convection to the lubricating oil via both dripping oil exiting the motor and the immersion of gear pairs in the oil sump. The thermal model focuses on the oil sump temperature T_{so}, as it correlates strongly with transmission power losses [131, 132]. Transmission losses arising from gear mesh friction and bearing friction are treated as uniformly distributed heat sources in the oil mass, while the sump oil exchanges heat with the ambient air through an effective heat transfer coefficient h_{so} and associated area A_{so}.

Applying the first law of thermodynamics to the oil sump control volume yields the energy balance as

$$m_{\text{so}} c_{p,\text{o}} \frac{dT_{\text{so}}}{dt} = \dot{m}_{\text{emoo}} c_{p,\text{o}} (T_{\text{emoo}} - T_{\text{so}}) + P_{\text{loss,tran}} - h_{\text{so}} A_{\text{so}} (T_{\text{so}} - T_{\text{a}}), \tag{7.22}$$

where m_{so} is the oil mass in the sump, $c_{p,\text{o}}$ is the specific heat capacity of the oil, and $\dot{m}_{\text{emoo}}$ is the oil mass flow rate returning from the motor.

7.3.2 Auxiliary component

AGS

The AGS regulates the airflow entering the radiator, thereby influencing the cooling performance of the thermal management system as well as the vehicle aerodynamic drag. With AGS, the aerodynamic drag coefficient in (2.20) is determined as

$$C_d(\phi) = \sum_{i=0}^{1} \alpha_i \, \phi^i. \tag{7.23}$$

Pump

The electrical power consumption of each pump is estimated using polynomial fits based on the fluid flow rate and corresponding pressure rise, as

$$P_{\text{pu,c}}(\dot{V}_{\text{c}}, \Delta p_{\text{pu,c}}) = \sum_{i=0}^{3} \sum_{j=0}^{1} \alpha_{ij} \dot{V}_{\text{c}}^i \Delta p_{\text{pu,c}}^j, \tag{7.24}$$

$$P_{\text{pu,o}}(\dot{V}_{\text{o}}, \Delta p_{\text{pu,o}}) = \sum_{i=0}^{3} \sum_{j=0}^{1} \alpha_{ij} \dot{V}_{\text{o}}^i \Delta p_{\text{pu,o}}^j, \tag{7.25}$$

where $\Delta p_{\text{pu,c}}$ and $\Delta p_{\text{pu,o}}$ are the corresponding pump pressure rises.

The pressure drops in the coolant circuit—across the radiator ($\Delta p_{\text{rad,c}}$), inverter cooling channel ($\Delta p_{\text{inv,c}}$), motor housing water jacket ($\Delta p_{\text{em,c}}$), and oil cooler ($\Delta p_{\text{oc,c}}$)—as well as those in the oil circuit—across the oil cooler ($\Delta p_{\text{oc,o}}$) and motor oil spray channel ($\Delta p_{\text{em,o}}$)—are modeled using polynomial fits. Each pressure drop is expressed as a function of fluid flow rate and inlet temperature. The pressure losses in connecting pipes are neglected. Thus, the required pressure rise of the coolant pump $\Delta p_{\text{pu,c}}$ and oil pump $\Delta p_{\text{pu,o}}$ are approximated as the sum of the major component pressure drops as

$$\Delta p_{\mathrm{pu,c}}(\cdot) = \Delta p_{\mathrm{rad,c}}(\dot{V}_{\mathrm{c}}, T_{\mathrm{occo}}) + \Delta p_{\mathrm{inv,c}}(\dot{V}_{\mathrm{c}}, T_{\mathrm{ici}}) + \Delta p_{\mathrm{em,c}}(\dot{V}_{\mathrm{c}}, T_{\mathrm{emci}}) + \Delta p_{\mathrm{oc,c}}(\dot{V}_{\mathrm{c}}, T_{\mathrm{emco}})$$
$$= \sum_{i=0}^{2}\sum_{j=0}^{1}\left(\alpha_{ij}\dot{V}_{\mathrm{c}}^{i}T_{\mathrm{occo}}^{j} + \alpha_{ij}\dot{V}_{\mathrm{c}}^{i}T_{\mathrm{ici}}^{j} + \alpha_{ij}\dot{V}_{\mathrm{c}}^{i}T_{\mathrm{emci}}^{j} + \alpha_{ij}\dot{V}_{\mathrm{c}}^{i}T_{\mathrm{emco}}^{j}\right), \tag{7.26}$$

$$\Delta p_{\mathrm{pu,o}}(\cdot) = \Delta p_{\mathrm{oc,o}}(\dot{V}_{\mathrm{o}}, T_{\mathrm{so}}) + \Delta p_{\mathrm{em,o}}(\dot{V}_{\mathrm{o}}, T_{\mathrm{emoi}}) = \sum_{i=0}^{2}\sum_{j=0}^{1}\left(\alpha_{ij}\dot{V}_{\mathrm{o}}^{i}T_{\mathrm{so}}^{j} + \alpha_{ij}\dot{V}_{\mathrm{o}}^{i}T_{\mathrm{emoi}}^{j}\right). \tag{7.27}$$

Heat exchanger

The coolant temperature at the radiator inlet is assumed equal to the oil cooler outlet temperature T_{occo}. The radiator outlet temperature is taken as the inverter coolant inlet temperature T_{ici}. The oil cooler coolant inlet temperature is set to the motor coolant outlet temperature T_{emco}. On the oil side, the cooler inlet temperature is assumed equal to the sump oil temperature T_{so}, and the outlet temperature is assumed to be equal to the motor oil inlet temperature T_{emoi}.

For both the radiator and oil cooler, the heat transfer rate is modeled as a polynomial function of the fluid inlet temperatures and flow rates as

$$Q_{\mathrm{rad}}(\cdot) = \sum_{i=0}^{2}\sum_{j=0}^{3}\sum_{k=0}^{1}\alpha_{ijk}\dot{V}_{\mathrm{c}}^{i}\dot{m}_{\mathrm{air}}^{j}T_{\mathrm{occo}}^{k} \tag{7.28}$$

$$Q_{\mathrm{oc}}(\cdot) = \sum_{i=0}^{3}\sum_{j=0}^{2}\sum_{k=0}^{1}\sum_{l=0}^{1}\alpha_{ijkl}\dot{V}_{\mathrm{c}}^{i}\dot{V}_{\mathrm{o}}^{j}T_{\mathrm{emco}}^{k}T_{\mathrm{so}}^{l} \tag{7.29}$$

where Q_{rad} and Q_{oc} are the radiator and oil cooler heat transfer rates, respectively. For (7.28) a certain ambient temperature is assumed.

Fan

The electrical power consumption of the fan is approximated as a polynomial function of the air mass flow rate and PWM duty cycle as

$$P_{\text{fan}}(\dot{m}_{\text{air}}, d_{\text{fan}}) = \sum_{i=0}^{1}\sum_{j=0}^{1} \alpha_{ij}\dot{m}_{\text{air}}^{i} d_{\text{fan}}^{j}. \tag{7.30}$$

The air mass flow rate through the radiator is approximated using a polynomial fit as a function of the AGS position angle, fan PWM duty cycle, and vehicle speed as

$$\dot{m}_{\text{air}}(\cdot) = \sum_{i=0}^{1}\sum_{j=0}^{2} \alpha_{ij} d_{\text{fan}}^{i} v^{j} \cdot \sum_{k=0}^{2} \alpha_k \phi^k. \tag{7.31}$$

7.3.3 Temperature-dependent loss

Inverter

For the inverter loss model described in (2.9), the AC current amplitude is primarily determined by the motor operating point. In addition, the winding and permanent magnet temperatures influence the current required for a certain motor operating point [133, 134]. Therefore, the AC current amplitude is approximated using a polynomial fit as a function of motor speed, torque, winding temperature, and permanent magnet temperature as

$$I_o(\cdot) = \sum_{i=0}^{2}\sum_{j=0}^{2}\sum_{k=0}^{1}\sum_{l=0}^{1} \alpha_{ijkl}\omega_{\text{em}}^{i} T_{\text{em}}^{j} T_{\text{w}}^{k} T_{\text{pm}}^{l}, \tag{7.32}$$

where ω_{em} is the motor speed and torque T_{em} is the motor torque. In addition to the temperature-dependent current usage, the on-state resistance and switching energy are approximated by polynomial fits as functions of the junction temperature as

$$r_{ds}(T_{\text{jt}}) = \sum_{i=0}^{2} \alpha_{ij} T_{\text{jt}}^{i}, \tag{7.33}$$

$$E_{sw}(T_{\text{jt}}) = \sum_{i=0}^{2} \alpha_{ij} T_{\text{jt}}^{i}. \tag{7.34}$$

Motor

The power loss $P_{\text{loss,w}}$ at the winding node includes both copper losses and stator iron losses, whereas $P_{\text{loss,pm}}$ represents the combined magnet losses and rotor iron losses. These losses depend on the motor operating point and both winding and permanent magnet temperatures. Therefore, polynomial fits are used to approximate the winding and magnet losses as

$$P_{\text{loss,w}}(\cdot) = \sum_{i=0}^{2}\sum_{j=0}^{3}\sum_{k=0}^{1}\sum_{l=0}^{1} \alpha_{ijkl}\omega_{\text{em}}^{i}T_{\text{em}}^{j}T_{\text{w}}^{k}T_{\text{pm}}^{l} \tag{7.35}$$

$$P_{\text{loss,pm}}(\cdot) = \sum_{i=0}^{3}\sum_{j=0}^{2}\sum_{k=0}^{1}\sum_{l=0}^{1} \alpha_{ijkl}\omega_{\text{em}}^{i}T_{\text{em}}^{j}T_{\text{w}}^{k}T_{\text{pm}}^{l} \tag{7.36}$$

Transmission

The transmission loss $P_{\text{loss,tran}}$ is approximated as a function of motor speed, motor torque, and sump oil temperature as

$$P_{\text{loss,tran}} = \sum_{i=0}^{1}\sum_{j=0}^{3}\sum_{k=0}^{2} \alpha_{ijk}\omega_{\text{em}}^{i}T_{\text{em}}^{j}T_{\text{so}}^{k} \tag{7.37}$$

7.4 Results and discussion

7.4.1 Rule-based strategy

A rule-based thermal management strategy is implemented as a baseline, with the objective of maintaining component temperatures within predefined operational limits. In such strategies, temperature targets are assigned to individual components, and auxiliary actuators (e.g., pumps and fans) are regulated to track these targets. As illustrated in Figure 7.4, the rule-based thermal management strategy is divided into three independent domains: air, coolant, and oil flow management.

In the airflow control domain, the actuator is governed by the radiator coolant outlet temperature, T_{ici}. When T_{ici} is below 65 °C, the AGS remains fully closed ($\phi = 0°$), and the fan is turned off. When $T_{\text{ici}} \geq 65$ °C, the AGS is fully open ($\phi = 90°$), and the fan PWM duty cycle is regulated proportionally to the deviation from the preset 65 °C target. To avoid frequent toggling of the fan, a 10-s hysteresis delay is introduced between transitions.

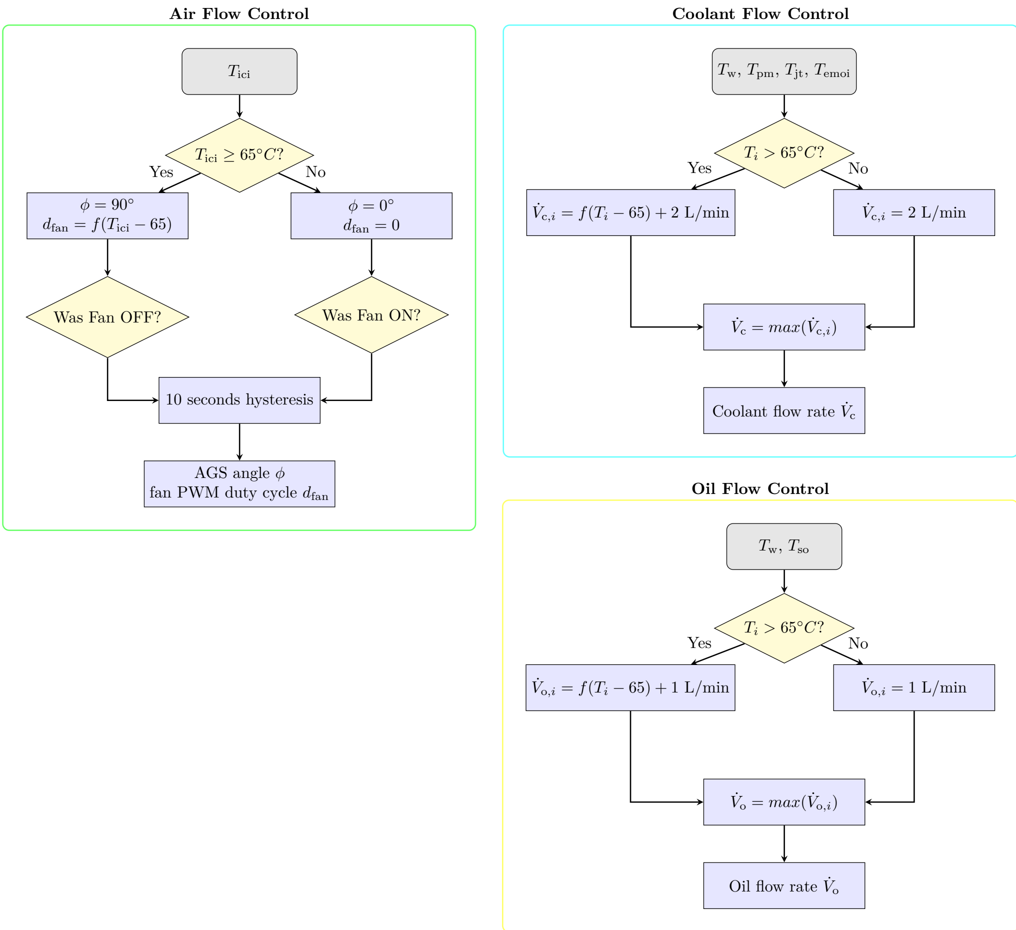

Figure 7.4: *Rule-based powertrain thermal management strategy.*

The coolant flow control domain monitors four component temperatures: winding T_w, magnet T_pm, inverter junction T_jt, and motor oil inlet T_emoi. For each temperature exceeding the preset threshold of 65 °C, the coolant flow request is computed linearly based on the deviation from this target, according to $\dot{V}_{\mathrm{c},i} = f(T_i - 65) + 2\,\mathrm{L\,min^{-1}}$, where $2\,\mathrm{L\,min^{-1}}$ represents the idle flow—i.e., the minimum flow rate required to circulate coolant through the circuit. If the temperature remains below the threshold, the idle flow $\dot{V}_{\mathrm{c},i}$, is maintained at $2\,\mathrm{L\,min^{-1}}$. Among the four individual requests, the maximum is selected to determine the final coolant flow rate demand: $\dot{V}_\mathrm{c} = \max(\dot{V}_{\mathrm{c},i})$.

The oil flow control follows a similar manner as the coolant, regulating flow based on the winding temperature T_w and sump oil temperature T_so. For each temperature exceeding 65 °C, the requested oil flow is computed as $\dot{V}_{\mathrm{o},i} = k(T_i - 65) + 1\,\mathrm{L\,min^{-1}}$, whereas idle flow $\dot{V}_{\mathrm{o},i} = 1\,\mathrm{L\,min^{-1}}$ is applied otherwise. The final oil flow rate demand is given by the maximum of the two individual requests: $\dot{V}_\mathrm{o} = \max(\dot{V}_{\mathrm{o},i})$.

7.4.2 Driving route

To evaluate the effectiveness of the proposed thermal management strategy under representative real-world conditions, sufficiently long driving routes are considered. Due to the inherently slow thermal dynamics of powertrain components, short driving routes may not lead to significant temperature rise and therefore cannot adequately reveal the impact of thermal management strategies on energy efficiency and component thermal limits.

Accordingly, two routes in Gothenburg are selected: one representing low-speed urban driving conditions and the other corresponding to high-speed highway operation. The associated vehicle speed profiles and road grade information for each route are shown in Figure 7.5.

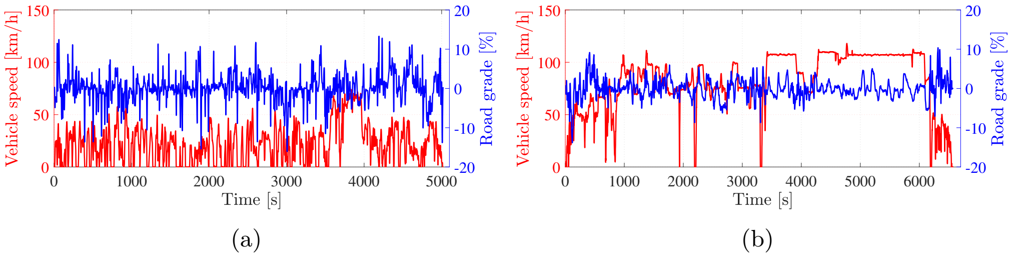

Figure 7.5: *Speed profile and road grade of the representative real-world driving routes. (a) Urban. (b) Highway.*

The urban route lasts 5019 s and is characterized by low speeds (mostly below 50 km/h) and frequent stop-and-go traffic. The road grade is dynamic, with multiple steep uphill and downhill segments reaching ±10 %. In contrast, the highway route spans 6576 s, beginning with a short rural segment averaging 70 km/h for the first 1000 s, followed by sustained high-speed driving near the speed limit of 110 km/h. The highway portion has a relatively smooth road grade with minimal variation.

7.4.3 Efficiency improvement

The simulation adopts a co-simulation approach using GT-Suite, Motor-CAD, and Simulink. An electro-mechanical-thermal model of the powertrain is developed in the GT-Suite, incorporating detailed representations of key powertrain components and the thermal management system. The motor is simulated in Motor-CAD and integrated into GT-Suite as a functional mock-up unit, allowing for high-fidelity thermal behavior within the system-level simulation.

The thermal management strategy is implemented in Simulink and interacts with the plant model in a closed loop. As illustrated in Figure 7.6, the MPC receives the ambient temperature, the vehicle speed profile, and the road slope over the prediction horizon as external inputs. It continuously updates relevant temperature states using feedback from the plant model. Based on this information, the controller computes the optimal AGS angle, fan PWM duty cycle, coolant flow rate, and oil flow rate by solving an NLP problem using the CasADi toolbox. The optimal actuation commands are then sent back to the plant model as the control inputs.

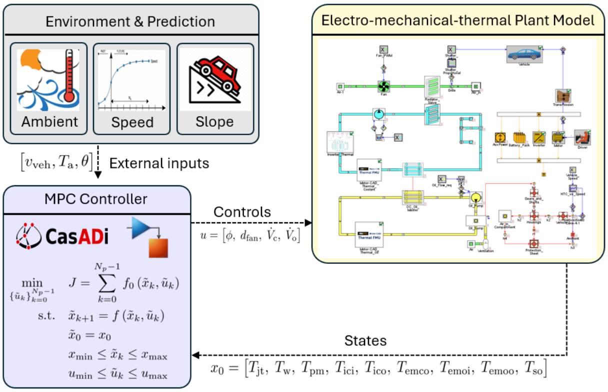

Figure 7.6: *Implementation of the MPC-based thermal management strategy and its closed-loop interaction with the powertrain plant model.*

The energy consumption for the urban and highway routes under rule-based and MPC-based thermal management strategies is summarized in Table 7.1. For this study, the ambient temperature is set at 23 °C, and the vehicle is assumed to be fully thermally soaked to this temperature prior to departure. The results indicate that the MPC-based strategy reduces battery energy consumption compared to the rule-based strategy in both driving routes. The urban route shows a marginal reduction of 0.26 % is observed, while the highway route achieves a more significant saving of 1.06 %.

Table 7.1: Energy consumption of rule-based and MPC-based thermal management strategies.

Route	**Rule-based [kWh/100 km]**	**MPC-based [kWh/100 km]**
Urban	15.36	15.32 (-0.26%)
Highway	20.85	20.63 (-1.06%)

A detailed breakdown of energy usage differences between the rule-based and MPC-based strategies, categorized into auxiliary component consumption, powertrain losses, and aerodynamic energy losses, is shown in Figure. 7.7.

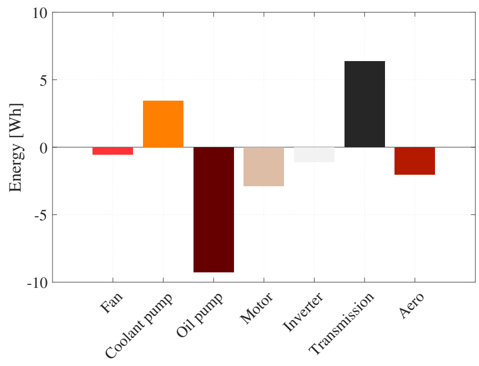

(a)

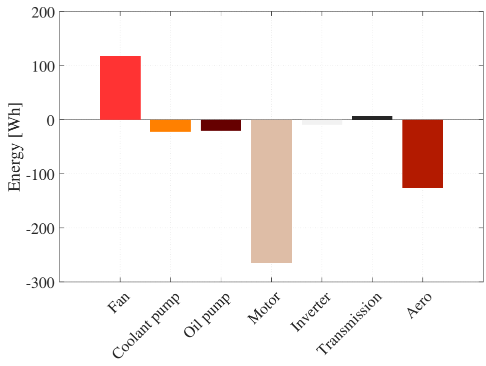

(b)

Figure 7.7: *Breakdown of energy usage difference between rule-based and MPC-based thermal management strategies. (a) Urban route and (b) Highway route.*

Urban route

Figure 7.8 illustrates the comparison of actuator control commands and key component temperatures under MPC-based and rule-based strategies during the urban route. Both strategies maintain powertrain component temperatures within safe limits. However, owing to the low-speed and low-power nature of the urban route, thermal stress is minimal, resulting in all component temperatures remaining well below their upper bounds.

The MPC-based strategy relies on AGS instead of the fan to increase airflow through the radiator. At low speeds, aerodynamic drag is negligible, so the increased AGS opening has minimal impact on energy consumption. The fan is not used under the MPC-based strategy, whereas the rule-based strategy activates the fan occasionally after 3000 s along with a fully opened AGS. In contrast, the MPC strategy employs partial but more frequent AGS openings, resulting in energy savings of 2.03 Wh from aerodynamic drag and 0.53 Wh from the fan.

In the rule-based strategy, no active cooling occurs during the first 2000 s, as the target threshold of 65 °C is not reached. In contrast, the MPC-based strategy initiates active cooling earlier by increasing the coolant flow rate. This results in slightly lower powertrain component temperatures and an increase in coolant pump energy consumption of 3.43 Wh. Reduced inverter and motor temperatures contribute to lower power losses, yielding savings of 1.09 Wh and 2.89 Wh, respectively. These savings result from reduced current demand due to enhanced magnet strength with cooler magnets under the maximum-torque-per-ampere control strategy, as well as temperature-dependent reductions in motor winding resistance, semiconductor on-state resistance, and switching energy [133, 135]. Furthermore, the MPC-based strategy maintains the oil pump at idle flow for almost the entire route, resulting in a 9.25 Wh reduction in oil pump energy. The coolant loop can sufficiently handle the thermal load under mild urban driving

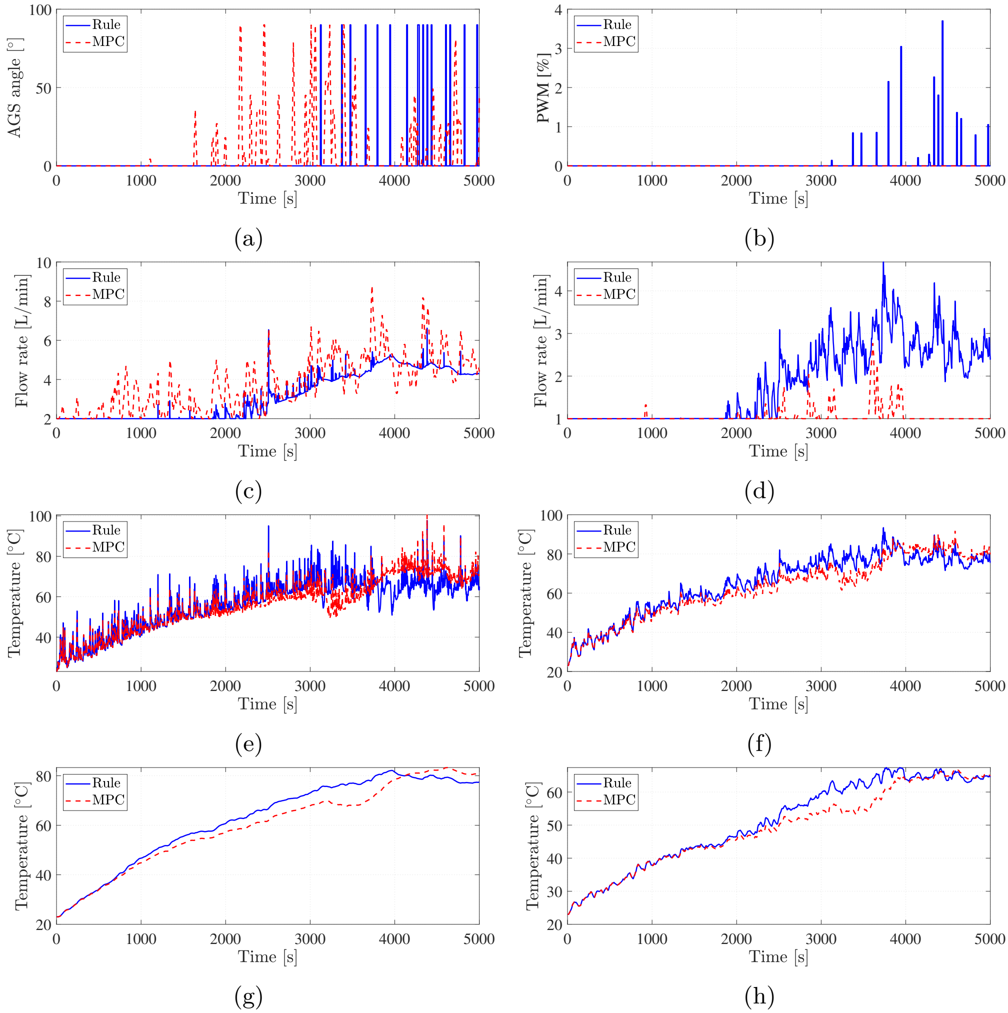

Figure 7.8: *Actuator control commands and key component temperatures for the urban route. (a) AGS angle. (b) Fan PWM duty cycle. (c) Coolant flow rate. (d) Oil flow rate. (e) Inverter junction temperature. (f) Motor winding temperature. (g) Motor magnet temperature. (h) Transmission sump oil temperature.*

conditions and is more energy-efficient than the oil circuit, which operates at higher pumping pressure. Conversely, the transmission experiences a 6.37 Wh increase in losses under the MPC-based strategy. For the studied transmission, efficiency follows a parabolic relationship with oil temperature, peaking approximately at 80 °C. Operating below this optimal temperature leads to increased losses due to higher oil viscosity.

The MPC-based strategy results in higher coolant pump energy consumption and increased transmission losses, offset by greater savings in inverter and motor losses, oil pump usage, and aerodynamic drag. This leads to a modest 0.26 % reduction in battery energy consumption over the urban route, consistent with the low power demand and limited thermal stress characteristic of mild driving conditions. The results indicate that under urban driving conditions, transmission losses and associated oil pump energy consumption significantly affect thermal management optimization. Specifically, oil pump energy reduction and increased transmission losses yield a net contribution of 2.88 Wh toward energy reduction. However, when excluding the oil pump and transmission losses, the remaining energy terms reflect a net reduction of 3.13 Wh, comparable to the transmission-oil pump contribution. This demonstrates that the transmission and oil circuit play a critical role in optimizing integrated powertrain thermal management. Consequently, MPC-based thermal management strategies developed without considering the transmission may not fully exploit potential energy savings under low-speed operating conditions.

Highway cycle

Figure 7.9 shows the details and comparison of the actuator control commands and key component temperatures under MPC-based and rule-based strategies during the highway cycle. The highway cycle involves high-speed, high-power operation, resulting in greater thermal stress on powertrain thermal management compared to the low-speed, low-power urban cycle. Consequently, powertrain component temperatures are significantly higher in both rule-based and MPC-based strategies. The MPC-based strategy permits components to operate closer to their thermal limits, with motor winding, magnet, and transmission sump oil temperatures nearing their upper bounds, and the inverter junction temperature reaching its limit approximately at 2000 s.

In the rule-based strategy, a strong cooling effort is evident, characterized by frequent fully opened AGS angles but limited fan activation. In contrast, the MPC-based strategy features fewer AGS openings, applying increased fan usage in the later stages of the cycle where accumulated thermal stress becomes critical. Given the high vehicle speeds during highway driving, natural airflow through the AGS is more effective, favoring the rule-based strategy. However, this results in higher aerodynamic drag, with 125.22 Wh consumed versus 117.19 Wh in the MPC-based strategy. Thus, in high-speed scenarios, it may be more energy-efficient to use fans with partially open AGS rather than fully opening the AGS, as aerodynamic drag has a stronger impact.

Furthermore, both coolant and oil flow rates are generally lower in the MPC-based strategy, and active cooling starts much later at approximately 2000 s compared to 800 s in the rule-based strategy. At this point, powertrain component temperatures are nearing their upper limits: the magnet reaches 140 °C, the transmission sump oil approaches 100 °C, the inverter junction hovers approximately at 100 °C, and the motor winding reaches 150 °C. Conversely, the rule-based strategy implements conservative cooling, maintaining lower component temperatures: inverter junction at 70 °C, motor winding at 100 °C, magnet at 100 °C, and transmission sump oil at approximately 75 °C, after an initial warm-up phase. This approach leads to higher auxiliary energy consumption, with

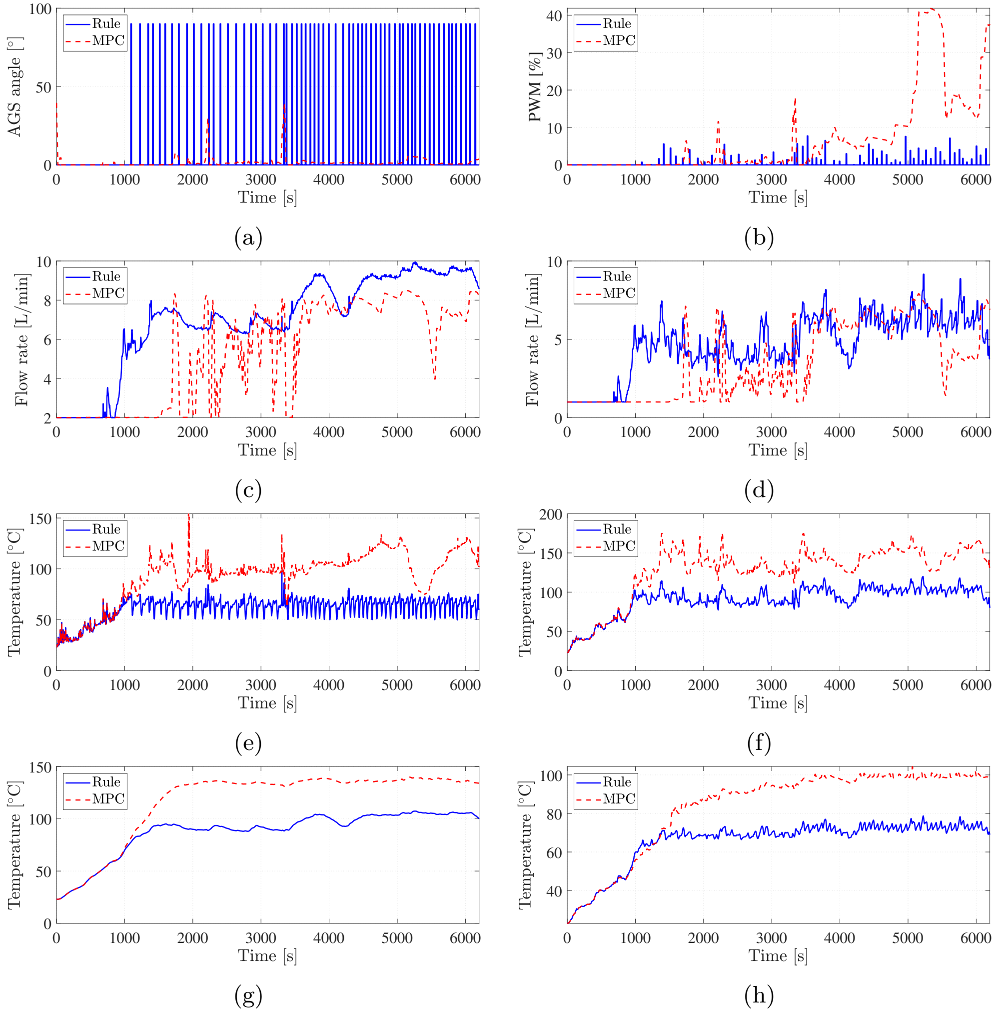

Figure 7.9: *Actuator control commands and key component temperatures for the highway route. (a) AGS angle. (b) Fan PWM duty cycle. (c) Coolant flow rate. (d) Oil flow rate. (e) Inverter junction temperature. (f) Motor winding temperature. (g) Motor magnet temperature. (h) Transmission sump oil temperature.*

21.36 Wh and 19.99 Wh used for the coolant and oil pumps, respectively. The elevated operating temperatures under the MPC-based strategy yield the opposite effect compared to the urban cycle regarding powertrain losses. During highway driving, vehicle speed exceeds 100 km/h, corresponding to motor speeds above 8000 rpm, entering the field weakening region for the studied IPMSM. The increased magnet temperature reduces its strength, thereby requiring less demagnetizing current. Despite higher winding resistance, semiconductors' on-state resistance and switching energy due to elevated temperatures, the inverter and motor losses are reduced by 9.01 Wh and 264.61 Wh as an overall result, respectively. The MPC-based strategy effectively utilizes the full thermal operating range of powertrain components, leveraging predictive information to maximize thermal margins and minimize cooling efforts. This reduces auxiliary energy use and component losses, resulting in a significant 1.06 % reduction in battery energy consumption over the highway cycle, consistent with the high power and thermal demand of this driving condition.

Additionally, the sump oil temperature in the MPC-based strategy is slightly above the optimal level, whereas it is slightly below in the rule-based strategy. Consequently, the transmission experiences marginally higher losses in the MPC case, with an increase of 6.5 Wh compared to the rule-based approach. In the highway cycle, overall energy reduction is primarily driven by motor loss reduction, unlike the urban cycle. The MPC-based strategy intentionally regulates the transmission sump oil temperature near its upper limit of 100 °C to enhance motor efficiency. Without explicitly modeling the integrated oil-cooled transmission, high-temperature operation could risk transmission overheating. Thus, incorporating the transmission and oil circuit is essential to fully leverage temperature-dependent motor efficiency benefits under highway driving conditions.

7.4.4 Summary

This chapter investigated the effectiveness of an energy-efficient powertrain thermal management strategy in improving powertrain energy efficiency. The conventional rule-based strategy maintains conservative temperature margins by activating cooling auxiliaries based on predefined thresholds, leading to persistent auxiliary power consumption and limited utilization of temperature-dependent efficiency characteristics. In contrast, the proposed MPC-based energy-efficient thermal management strategy coordinates thermal management actuators using predictive information, enabling powertrain components to operate closer to their admissible thermal limits while minimizing cooling effort.

The results further demonstrate that the achievable efficiency benefit depends strongly on the thermal loading imposed by the driving condition. Under urban operation, limited thermal stress restricts the potential for reducing powertrain losses, and energy savings are primarily associated with reduced auxiliary operation. Under highway operation, higher thermal loading allows the MPC strategy to exploit the full admissible thermal operating range of powertrain components. Elevated operating temperatures improve motor efficiency in the field-weakening region and reduce cooling demand, resulting in energy savings dominated by reductions in motor and inverter losses.

8 Conclusions and Future Work

This chapter summarizes the work presented in this thesis and outlines the future work.

8.1 Conclusions and discussion

This thesis has investigated energy-efficient BEV powertrains from the perspectives of powertrain architecture, control, and thermal management. A common finding throughout the studies is that system-level approaches, which modify either the powertrain architecture or its operation to shift key components toward more favorable operating conditions, can effectively improve the energy efficiency of BEV powertrains.

For dual-motor powertrains, disconnect functionality provides a significant efficiency benefit by eliminating unnecessary no-load losses from inactive EDUs. For the investigated AFRID powertrain, the optimized operating-mode strategy reduces WLTC energy consumption by 8.21% compared with the conventional FRID configuration. The results also demonstrate the strong coupling between powertrain architecture and control: the additional operating flexibility introduced by the clutches can only be fully exploited through an appropriate EMS. This interaction can be further strengthened through configuration-aware motor design, where jointly optimizing the front and rear motor geometries and EMS provides an additional energy-consumption reduction of approximately 0.98% compared with an AFRID configuration employing identical motors.

Disconnect functionality can provide further benefits when combined with eco-driving. By allowing controlled deviations from the reference vehicle speed, longer and more frequent free-coasting periods can be introduced in which the powertrain is completely disconnected and EDU no-load losses are avoided. The achievable energy saving depends strongly on the allowable speed deviation and the availability of predictive road and traffic information. Although this approach can provide substantial efficiency improvement, its practical implementation requires closer integration with advanced driver assistance systems and navigation functions.

Adjustable DC-link voltage provides an additional degree of freedom by decoupling the DC-link voltage from the battery voltage. The results show that the optimal DC-link voltage varies with operating condition and battery terminal voltage. For lower-voltage battery systems, a boost configuration can improve efficiency particularly at high-speed operation, whereas high-voltage architectures can benefit from buck conversion by reducing unnecessary switching losses at lower-load conditions. The use of SiC-MOSFETs further improves the energy-saving potential by reducing the additional losses introduced by the DC–DC converter. However, these benefits must be balanced against the added converter cost, mass, packaging, and control complexity.

Torque modulation demonstrates that powertrain efficiency can also be improved primarily through control adaptation without substantial hardware changes. By periodically shifting operation away from inefficient low-torque regions, overall energy losses can be reduced when the modulation parameters are optimized from a complete powertrain perspective rather than considering only the motor and inverter. In dual-motor powertrains, complementary modulation between the front and rear motors provides additional operating freedom and can reduce the resulting total powertrain torque fluctuation. Nevertheless, the efficiency benefit must be balanced against driver comfort and the additional cyclic loading imposed on powertrain components.

The thermal-management study further shows that component temperature can be treated as an optimization variable rather than only as a constraint. By coordinating powertrain component temperatures together with the thermal management system, the proposed strategy balances temperature-dependent powertrain losses against cooling-system auxiliary consumption. However, operating components at temperatures that are favorable from an energy-efficiency perspective may increase thermal aging. The resulting efficiency benefit must therefore be balanced against component lifetime.

Considering the investigated solutions together, there is a clear trade-off between achievable energy saving and implementation effort. Architecture-level solutions such as disconnect functionality and adjustable DC-link voltage introduce additional operating flexibility, but also require additional hardware, packaging, and control development. Their effectiveness is closely linked to the corresponding control strategy, highlighting that novel powertrain architectures and control optimization should preferably be developed together rather than independently. Configuration-aware motor optimization follows the same principle and is particularly relevant during the early stages of powertrain development.

In contrast, control-oriented solutions such as torque modulation can generally be introduced with fewer hardware modifications and therefore potentially lower implementation cost. Energy-oriented thermal management can also make greater use of existing hardware, although it requires more advanced numerical modeling, control, and calibration. These approaches may provide smaller or more operating-condition-dependent energy savings, but can be attractive when major hardware redesign is undesirable. Their implementation must, however, account for trade-offs with other vehicle attributes, particularly driver comfort and component durability.

Overall, approaches with larger potential energy savings often require greater hardware modification or system integration, whereas software-oriented approaches can usually be implemented with lower additional cost but provide more operating-condition-dependent benefits. The appropriate solution should therefore be selected by considering energy-efficiency improvement together with implementation effort, cost, complexity, drivability, and durability. The findings consequently emphasize the importance of coordinated powertrain architecture, control, and thermal management in the development of energy-efficient BEV powertrains.

8.2 Future work

Based on the work presented in this thesis, the following research can be conducted in the future.

- **Integration of architecture-level efficiency enhancement methods.**

  In this thesis, architecture-level efficiency improvement methods are investigated in dedicated studies. Future research may explore their integrated application. For instance, the combination of disconnect functionality and adjustable DC-link voltage in dual-motor powertrains could further expand system operating flexibility. In particular, the front and rear EDUs could be designed to operate at different DC-link voltage levels depending on driving conditions, where one EDU is primarily dedicated to low-speed operation using a buck-configured DC–DC converter, while the other is optimized for high-speed operation with a higher DC-link voltage. When combined with task-oriented asymmetric motor design, such an architecture could enable the two EDUs to cover complementary high-efficiency regions more effectively and enhance the flexibility of FWD/RWD operation. However, this may increase system cost and control complexity. Therefore, a thorough investigation is required to evaluate the overall trade-offs between efficiency improvement, hardware cost, system reliability, and control implementation feasibility.

- **Thermal management with complex powertrain architectures.**

  This thesis investigates energy-efficient thermal management for a simple single-motor powertrain architecture. Future research can investigate the coordinated design of thermal management strategies with more complex powertrain architectures. For example, in dual-motor powertrains, torque split optimization could be extended to explicitly consider the thermal states and limits of individual EDUs, enabling thermally aware energy management and improved system efficiency. In addition, different powertrain architectures may require tailored thermal management system designs. For instance, the introduction of adjustable DC-link voltage architectures necessitates dedicated cooling considerations for additional components such as DC–DC converters. Therefore, integrated electro-thermal powertrain optimization frameworks should be developed to capture the interactions between powertrain configuration, control strategies, and thermal system design.

- **Integrated vehicle-level energy and thermal management.**

  This thesis primarily focuses on powertrain-related energy losses and thermal management. Future research should extend the proposed efficiency-oriented control and optimization frameworks to the complete vehicle energy management system, including cabin heating and cooling, battery thermal management, and other auxiliary circuits. In particular, the interactions between the powertrain thermal management system and cabin climate control become critical under extreme ambient conditions, especially in cold-weather operation where heating demand can significantly affect overall energy consumption and driving range. Developing coordinated vehicle-level energy and thermal management strategies would enable more effective utilization of waste heat, improved system integration, and enhanced overall vehicle efficiency.

- **Real-time implementation of predictive control strategies.**

  Several strategies proposed in this thesis rely on optimization-based predictive control, such as MPC-based eco-driving with disconnect functionality, which leads to mixed-integer nonlinear optimization problems. Standard solution methods, e.g., branch-and-bound, may not be sufficiently fast for real-time onboard applications. Moreover, these strategies typically depend on route preview information and online optimization. Future work should therefore focus on reducing computational complexity, improving solver efficiency, and developing embedded implementations suitable for real-time vehicle control units. In addition, robustness against model mismatch, sensor uncertainty, and imperfect route preview information should be systematically investigated.

- **Adaptive and learning-based models for powertrain efficiency optimization.**

  The control-oriented models adopted in this thesis are primarily based on physics-informed approximations and fitted loss maps. In addition, static maps used for constraining the EMS are typically generated offline and may become inaccurate due to variations in operating conditions, temperature effects, aging, and component degradation. Future research can therefore investigate adaptive or hybrid physics-based and data-driven modeling approaches that enable online parameter updating using operational data. Such methods could improve the prediction accuracy of thermal behavior, powertrain losses, and route-dependent vehicle performance over the vehicle lifetime, thereby enhancing the effectiveness of EMS.

Bibliography

[1] Changlong Ling, Junqing Tang, Pengjun Zhao, Lei Xu, Qiuchen Lu, Linchuan Yang, Fengjue Huang, Wei Lyu, and Jiawen Yang. "Unraveling the relation between carbon emission and carbon footprint: A literature review and framework for sustainable transportation". In: *npj Sustainable Mobility and Transport* 1.1 (2024), p. 13.

[2] Paulina Jaramillo, Suzana Kahn Ribeiro, Peter Newman, Subash Dhar, Ogheneruona E Diemuodeke, Tsutomu Kajino, David Simon Lee, Sudarmanto Budi Nugroho, Xunmin Ou, Anders Hammer Strømman, et al. "Transport (chapter 10)". In: *IPCC 2022: Climate Change 2022: Mitigation of Climate Change. Contribution of Working Group III to the Sixth Assessment Report of the Intergovernmental Panel on Climate Change* (2023), pp. 1049–1160.

[3] Joris Šimaitis, Rick Lupton, Christopher Vagg, Isabela Butnar, Romain Sacchi, and Stephen Allen. "Battery electric vehicles show the lowest carbon footprints among passenger cars across 1.5–3.0° C energy decarbonisation pathways". In: *Communications Earth & Environment* 6.1 (2025), p. 476.

[4] IEA Global EV Outlook et al. *Trends in electric car markets.* 2025.

[5] Yinxin Fei, Ping Qin, Yanlai Chu, Huanhuan Zheng, Jie-Sheng Tan-Soo, and Xiao-Bing Zhang. "Does high gasoline price spur electric vehicle adoption? Evidence from Chinese cities". In: *Energy Economics* 142 (2025), p. 108188.

[6] Giuseppe Rainieri, Chiara Buizza, and Alberto Ghilardi. "The psychological, human factors and socio-technical contribution: A systematic review towards range anxiety of battery electric vehicles' drivers". In: *Transportation research part F: traffic psychology and behaviour* 99 (2023), pp. 52–70.

[7] Marc A Melliger, Oscar PR van Vliet, and Heikki Liimatainen. "Anxiety vs reality–Sufficiency of battery electric vehicle range in Switzerland and Finland". In: *Transportation Research Part D: Transport and Environment* 65 (2018), pp. 101–115.

[8] Dong Guo, Ruiyuan Liu, Minghui Li, Xiaochuan Tan, Pengcheng Ma, and Hongjia Zhang. "An approach to optimizing the layout of charging stations considering differences in user range anxiety". In: *Sustainable Energy, Grids and Networks* 38 (2024), p. 101292.

[9] Abdullah Isilti and James E Tate. “Technical performance evolution of BEVs: range, consumption and weight projections to 2050”. In: *Transportation Research Part D: Transport and Environment* 152 (2026), p. 105172.

[10] Axel Celadon, Huaihu Sun, Shuhui Sun, and Gaixia Zhang. “Batteries for electric vehicles: Technical advancements, environmental challenges, and market perspectives”. In: *SusMat* 4.5 (2024), e234.

[11] Jingjing Xu, Xingyun Cai, Songming Cai, Yaxin Shao, Chao Hu, Shirong Lu, and Shujiang Ding. “High-energy lithium-ion batteries: recent progress and a promising future in applications”. In: *Energy & Environmental Materials* 6.5 (2023), e12450.

[12] FM Nizam Uddin Khan, Mohammad G Rasul, ASM Sayem, and Nirmal Mandal. “Maximizing energy density of lithium-ion batteries for electric vehicles: A critical review”. In: *Energy Reports* 9 (2023), pp. 11–21.

[13] Jari Vepsäläinen, Klaus Kivekäs, Kevin Otto, Antti Lajunen, and Kari Tammi. “Development and validation of energy demand uncertainty model for electric city buses”. In: *Transportation Research Part D: Transport and Environment* 63 (2018), pp. 347–361.

[14] Mingcai Zhao, Carlos M Costa, Irune Villaluenga, Frieder Scheiba, Juan Zhang, Wei Wang, Senentxu Lanceros-Méndez, and Qi Zhang. “Should EVs prioritize range? Strategies for efficient battery use, energy transition, and sustainability”. In: *Materials Today Energy* 52 (2025), p. 101945.

[15] Michael A Roscher, Roland Michel, and Wolfgang Leidholdt. “Improving energy conversion efficiency by means of power splitting in dual drive train EV applications”. In: *International Journal of Vehicular Technology* 2013 (2013).

[16] Wang Da and Wang Bo. “Research on driving force optimal distribution and fuzzy decision control system for a dual-motor electric vehicle”. In: *2015 34th Chinese Control Conference (CCC)*. IEEE. 2015, pp. 8146–8153.

[17] Nobuyoshi Mutoh. “Front-and-rear-wheel-independent-drive-type electric vehicle (FRID EV) with compatible driving performance and safety”. In: *World Electric Vehicle Journal* 3.1 (2009), pp. 17–26.

[18] Nobuyoshi Mutoh, Yusuke Takahashi, and Yoshiki Tomita. “Failsafe drive performance of FRID electric vehicles with the structure driven by the front and rear wheels independently”. In: *IEEE Transactions on Industrial Electronics* 55.6 (2008), pp. 2306–2315.

[19] Marco Veliz Castro, Shruthi Mukundan, Claudio Lopes Filho, Glenn Byczynski, Bruce Minaker, Jimi Tjong, and Narayan C. Kar. “A Review of Existing Multi-Motor Electric Powertrain Sizing Strategies”. In: *2021 24th International Conference on Electrical Machines and Systems (ICEMS)*. 2021, pp. 2419–2424. DOI: 10.23919/ICEMS52562.2021.9634221.

[20] Nobuyoshi Mutoh, Takuro Kazama, and Kazuya Takita. "Driving characteristics of an electric vehicle system with independently driven front and rear wheels". In: *IEEE Transactions on Industrial Electronics* 53.3 (2006), pp. 803–813.

[21] Utkal Ranjan Muduli, Abdul R. Beig, Khaled Al Jaafari, Jamal Y. Alsawalhi, and Ranjan Kumar Behera. "Interrupt-Free Operation of Dual-Motor Four-Wheel Drive Electric Vehicle Under Inverter Failure". In: *IEEE Transactions on Transportation Electrification* 7.1 (2021), pp. 329–338. DOI: 10.1109/TTE.2020.2997354.

[22] Uwe Vollmer and Uwe Schäfer. "An at-all operating points highly efficient PMSM for HEV". In: *World Electric Vehicle Journal* 2.4 (2008), pp. 334–342.

[23] Dongmei Wu, Yang Li, Jianwei Zhang, and Changqing Du. "Torque distribution of a four in-wheel motors electric vehicle based on a PMSM system model". In: *Proceedings of the Institution of Mechanical Engineers, Part D: Journal of Automobile Engineering* 232.13 (2018), pp. 1828–1845.

[24] Wang Da and Wang Bo. "Research on driving force optimal distribution and fuzzy decision control system for a dual-motor electric vehicle". In: *2015 34th Chinese Control Conference (CCC)*. IEEE. 2015, pp. 8146–8153.

[25] Xiaosong Hu, Yapeng Li, Chen Lv, and Yonggang Liu. "Optimal Energy Management and Sizing of a Dual Motor-Driven Electric Powertrain". In: *IEEE Transactions on Power Electronics* 34.8 (2019), pp. 7489–7501. DOI: 10.1109/TPEL.2018.2879225.

[26] Minghui Hu, Jianfeng Zeng, Shaozhi Xu, Chunyun Fu, and Datong Qin. "Efficiency Study of a Dual-Motor Coupling EV Powertrain". In: *IEEE Transactions on Vehicular Technology* 64.6 (2015), pp. 2252–2260. DOI: 10.1109/TVT.2014.2347349.

[27] Khalil Abdelali, Bachir Bendjedia, and Nassim Rizoug. "A Comparative Study of IPMSM Efficiency Using Complete Driving Cycles and Representative Clustering Techniques in EV Applications". In: *2025 11th International Conference on Control, Decision and Information Technologies (CoDIT)*. Vol. 1. IEEE. 2025, pp. 3037–3041.

[28] Yuancong Gong, Andreas Gneiting, Chongshen Zhao, Nejila Parspour, and Hao Chen. "Comparative Study of Different Data-Driven Surrogate Models for Optimization of Synchronous Reluctance Machine". In: *IEEE Transactions on Industry Applications* 62.1 (2025), pp. 857–869.

[29] Kihan Kwon, Minsik Seo, and Seungjae Min. "Efficient multi-objective optimization of gear ratios and motor torque distribution for electric vehicles with two-motor and two-speed powertrain system". In: *Applied Energy* 259 (2020), p. 114190.

[30] Yang Tian, Yahui Zhang, Hongmin Li, Jinwu Gao, Austin Swen, and Guilin Wen. "Optimal sizing and energy management of a novel dual-motor powertrain for electric vehicles". In: *Energy* 275 (2023), p. 127315.

[31] Xiaosong Hu, Yapeng Li, Chen Lv, and Yonggang Liu. "Optimal energy management and sizing of a dual motor-driven electric powertrain". In: *IEEE Transactions on Power Electronics* 34.8 (2018), pp. 7489–7501.

[32] Xiaoyu Ding, Xinbo Chen, Jiantao Zhang, and Aijing Kong. "Matching Strategy and Optimization of Propulsion System Parameters for the Front-Centralized and Rear-Distributed Drive Electric Vehicle". In: *2025 IEEE 2nd International Conference on Energy and Electrical Engineering (EEE)*. IEEE. 2025, pp. 1–6.

[33] Cong Thanh Nguyen, Paul D Walker, Shilei Zhou, and Nong Zhang. "Optimal sizing and energy management of an electric vehicle powertrain equipped with two motors and multi-gear ratios". In: *Mechanism and Machine Theory* 167 (2022), p. 104513.

[34] Zejia He, Qin Shi, Yujiang Wei, Jianxin Zheng, Bingzhao Gao, and Lin He. "A torque demand model predictive control approach for driving energy optimization of battery electric vehicle". In: *IEEE Transactions on Vehicular Technology* 70.4 (2021), pp. 3232–3242.

[35] Dong-mei Wu, Yue Li, Chang-qing Du, Hai-tao Ding, Yang Li, Xiao-bo Yang, and Xin-yue Lu. "Fast velocity trajectory planning and control algorithm of intelligent 4WD electric vehicle for energy saving using time-based MPC". In: *IET Intelligent Transport Systems* 13.1 (2019), pp. 153–159.

[36] Christian Sohn, Jakob Andert, and Dejan Jolovic. "An analysis of the tradeoff between fuel consumption and ride comfort for the pulse and glide driving strategy". In: *IEEE Transactions on Vehicular Technology* 69.7 (2020), pp. 7223–7233.

[37] C Freitas Salgueiredo, Olivier Orfila, Guillaume Saint Pierre, Philippe Doublet, Sébastien Glaser, Stéphane Doncieux, and Véronique Billat. "Experimental testing and simulations of speed variations impact on fuel consumption of conventional gasoline passenger cars". In: *Transportation Research Part D: Transport and Environment* 57 (2017), pp. 336–349.

[38] Jae Hyuk Lee, Jung Hyo Lee, Jin Ho Park, and Chung Yuen Won. "Field-weakening strategy in condition of DC-link voltage variation using on electric vehicle of IPMSM". In: *2011 International Conference on Electrical Machines and Systems*. IEEE. 2011, pp. 1–6.

[39] Nan Zhao, Nigel Schofield, Rong Yang, and Ran Gu. "Investigation of DC-link voltage and temperature variations on EV traction system design". In: *IEEE Transactions on Industry Applications* 53.4 (2017), pp. 3707–3718.

[40] Jorge O Estima and Antonio J Marques Cardoso. "Efficiency analysis of drive train topologies applied to electric/hybrid vehicles". In: *IEEE Transactions on Vehicular Technology* 61.3 (2012), pp. 1021–1031.

[41] Kashyap Kumar Prabhakar, Maloth Ramesh, Ankit Dalal, C Upendra Reddy, Amit Kumar Singh, and Praveen Kumar. "Efficiency investigation for electric

vehicle powertrain with variable DC-link bus voltage". In: *IECON 2016-42nd Annual Conference of the IEEE Industrial Electronics Society*. IEEE. 2016, pp. 1796–1801.

[42] Chen-Yen Yu, Jun Tamura, and Robert D Lorenz. "Optimum DC bus voltage analysis and calculation method for inverters/motors with variable DC bus voltage". In: *IEEE Transactions on Industry Applications* 49.6 (2013), pp. 2619–2627.

[43] Camilo Suarez and Wilmar Martinez. "Fast and ultra-fast charging for battery electric vehicles–a review". In: *2019 IEEE Energy Conversion Congress and Exposition (ECCE)*. IEEE. 2019, pp. 569–575.

[44] Sukanya Dutta and Jennifer Bauman. "An overview of 800 V passenger electric vehicle onboard chargers: Challenges, topologies, and control". In: *IEEE Access* 12 (2024), pp. 105850–105864.

[45] Mohammad Hossein Mousavi, Hassan Moradi, and Kumars Rouzbehi. "Transition of DC link voltage from 400V to 800V in electric vehicles: performance, trade-offs, and technical insights". In: *2025 10th International Conference on Technology and Energy Management (ICTEM)*. IEEE. 2025, pp. 1–7.

[46] Wolfgang Wenzel, Prashant Hegde, and Gabriel Domingues. "Optimized System Voltage Level for Increased Efficiency of Battery-electric Vehicles". In: *ATZextra worldwide* 28.1 (2023), pp. 18–21.

[47] Zhiqian Chen, P Carvell, and M Younkins. "Optimizing electric motor controls with dynamic motor drive". In: *30th Aachen Coll. Sustainable Mobility* (2021).

[48] M Younkins, P Carvell, and J Fuerst. "Dynamic motor drive: Optimizing electric motor controls to improve efficiency". In: *42nd International Vienna Motor Symposium Vienna*. 2021.

[49] Md Zakirul Islam, Amnish Singh, Anastasios Arvanitis, Matthew Younkins, Siyu Leng, Paul Carvell, Adya Tripathi, Zhiqian Chen, and Andrew Phillips. *Efficiency improvement of electric motor drives using dynamic motor drive technology*. Tech. rep. SAE Technical Paper, 2022.

[50] Yinye Yang, Berker Bilgin, Michael Kasprzak, Shamsuddeen Nalakath, Hossam Sadek, Matthias Preindl, James Cotton, Nigel Schofield, and Ali Emadi. "Thermal management of electric machines". In: *IET Electrical Systems in Transportation* 7.2 (2017), pp. 104–116.

[51] Ahmed Al-Timimy, Paolo Giangrande, Michele Degano, Michael Galea, and Chris Gerada. "Investigation of ac copper and iron losses in high-speed high-power density PMSM". In: *2018 XIII International Conference on Electrical Machines (ICEM)*. IEEE. 2018, pp. 263–269.

[52] Lin Liu, Youguang Guo, Gang Lei, and Jianguo Zhu. "Comparative Iron Loss Analysis of the Interior PMSMs for Electric Vehicles Considering the Effects

of Temperature Variation”. In: *2023 IEEE International Conference on Applied Superconductivity and Electromagnetic Devices (ASEMD)*. IEEE. 2023, pp. 1–2.

[53] Debi Prasad Nayak, Ravi Kumar Yakala, Manish Kumar, and Sumit Kumar Pramanick. “Temperature-dependent reverse recovery characterization of SiC MOSFETs body diode for switching loss estimation in a half-bridge”. In: *IEEE Transactions on Power Electronics* 37.5 (2021), pp. 5574–5582.

[54] Furong Jiang, Kuang Sheng, and Qing Guo. “Comparative study of temperature-dependent characteristics for SiC MOSFETs”. In: *2016 13th China International Forum on Solid State Lighting: International Forum on Wide Bandgap Semiconductors China (SSLChina: IFWS)*. IEEE. 2016, pp. 50–53.

[55] Shufa Yan, Zhuo Kong, Hongwei Liu, Lin Zhang, Xiaoyu Hu, and Yuanjing Hou. “Power Loss Evaluation of an E-Axle Gearbox Considering the Influence of Gear Oil Factors”. In: *Lubricants* 12.1 (2024), p. 11.

[56] İsmail Kaya and Cemal Baykara. “The investigation of the effect of operating conditions in gearboxes on efficiency”. In: *Advances in Mechanical Engineering* 16.4 (2024), p. 16878132241248072.

[57] Jiamin Xu, Caizhi Zhang, Ruijia Fan, Huanhuan Bao, Yi Wang, Shulong Huang, Cheng Siong Chin, and Congxin Li. “Modelling and control of vehicle integrated thermal management system of PEM fuel cell vehicle”. In: *Energy* 199 (2020), p. 117495.

[58] Dongjun Li, Caizhi Zhang, Ruijia Fan, Lei Xu, Yi Wang, Wenjun Guo, Jinrui Chen, and Meng Ni. “An innovative thermal management method for cooling loop of electric driving system for durable and high efficiency electric vehicle”. In: *Applied Thermal Engineering* 195 (2021), p. 117176.

[59] Thomas Bächle, Knut Graichen, Michael Buchholz, and Klaus Dietmayer. “Loss-focused predictive thermal management of induction motors in electric vehicles using nonlinear fixed-point MPC”. In: *2016 IEEE Conference on Control Applications (CCA)*. IEEE. 2016, pp. 1392–1397.

[60] Mohammad Ghazali, Mario Vukotić, Damijan Miljavec, and Ahu Ece Hartavi. “Temperature-adaptive torque allocation for all wheel drive electric trucks”. In: *Applied thermal engineering* (2025), p. 126846.

[61] Lulu Guo, Bowen Yang, and Jin Ye. “Predictive energy management for dual-motor BEVs considering temperature-dependent traction inverter loss”. In: *IEEE transactions on transportation electrification* 8.1 (2021), pp. 1501–1515.

[62] Xinran Tao, Kan Zhou, John R Wagner, and Heath Hofmann. “An electric motor thermal management system for hybrid vehicles: modelling and control”. In: *International Journal of Vehicle Performance* 2.3 (2016), pp. 207–227.

[63] Xuanyao Wang and Youwang Feng. “Research on Energy Consumption Optimization Control Strategy of Electric Vehicle Electric Drive Oil/Water Cooling System”. In: *International Journal of Automotive Technology* 25.3 (2024), pp. 595–610.

[64] Shervin Shoai Naini, Richard Steven Miller, Denise Rizoo, and John Wagner. “A Model Reference Adaptive Controller for an Electric Motor Thermal Management System in Autonomous Vehicles”. In: *SAE International Journal of Electrified Vehicles* 12.1 (2023), pp. 3–16.

[65] Sheng Yu, Cuneyt Haspolat, Yaprak Yalcin, Saleh Msaddi, Boli Chen, Simos A Evangelou, and Imad M Jaimoukha. “Motor-Temperature-Aware Optimal Energy Management for Dual-Motor Electric Buses”. In: *2024 IEEE Vehicle Power and Propulsion Conference (VPPC)*. IEEE. 2024, pp. 1–6.

[66] Stefan Schaut, Eckhard Arnold, and Oliver Sawodny. “Predictive thermal management for an electric vehicle powertrain”. In: *IEEE Transactions on Intelligent Vehicles* 8.2 (2021), pp. 1957–1970.

[67] Alexander Wahl, Christoph Wellmann, Björn Krautwig, Patrick Manns, Bicheng Chen, Christof Schernus, and Jakob Andert. “Efficiency increase through model predictive thermal control of electric vehicle powertrains”. In: *Energies* 15.4 (2022), p. 1476.

[68] Alexander Wahl, Christoph Wellmann, Christian Monissen, and Jakob Andert. “Active temperature control of electric drivetrains for efficiency increase”. In: *Applied Energy* 338 (2023), p. 120887.

[69] Christoph Wellmann, Abdul Rahman Khaleel, Tobias Brinkmann, Alexander Wahl, Christian Monissen, Markus Eisenbarth, and Jakob Andert. “Electric machine co-optimization for EV drive technology development: Integrating Bayesian optimization and nonlinear model predictive control”. In: *eTransportation* 23 (2025), p. 100392.

[70] Ahmad Rahmoun and Helmuth Biechl. “Parameters identification of equivalent circuit diagrams for li-ion batteries”. In: *Proceedings of the 11th International Symposium PÄRNU “Topical Problems in the Field of Electrical and Power Engineering” and “Doctoral School of Energy and Geotechnology”, Pärnu, Estonia*. 2012, pp. 16–21.

[71] Gaizka Saldaña, José Ignacio San Martín, Inmaculada Zamora, Francisco Javier Asensio, and Oier Oñederra. “Analysis of the current electric battery models for electric vehicle simulation”. In: *Energies* 12.14 (2019), p. 2750.

[72] Xin Lai, Shuyu Wang, Shangde Ma, Jingying Xie, and Yuejiu Zheng. “Parameter sensitivity analysis and simplification of equivalent circuit model for the state of charge of lithium-ion batteries”. In: *Electrochimica Acta* 330 (2020), p. 135239.

[73] Julian Estaller, Anton Kersten, Manuel Kuder, Ali Mashayekh, Johannes Buberger, Torbjörn Thiringer, Richard Eckerle, and Thomas Weyh. “Battery Impedance Modeling and Comprehensive Comparisons of State-Of-The-Art Cylindrical 18650 Battery Cells considering Cells’ Price, Impedance, Specific Energy and C-Rate”. In: *2021 IEEE International Conference on Environment and Electrical Engineering and 2021 IEEE Industrial and Commercial Power Systems Europe (EEEIC / I&CPS Europe)*. 2021, pp. 1–8. DOI: 10.1109/EEEIC/ICPSEurope51590.2021.9584562.

[74] Julian Estaller, Anton Kersten, Manuel Kuder, Torbjörn Thiringer, Richard Eckerle, and Thomas Weyh. “Overview of Battery Impedance Modeling Including Detailed State-of-the-Art Cylindrical 18650 Lithium-Ion Battery Cell Comparisons”. In: *Energies* 15.10 (2022), p. 3822.

[75] Si Li and Ximing Cheng. “A comparative study on RC models of lithium-ion battery”. In: *2014 IEEE Conference and Expo Transportation Electrification Asia-Pacific (ITEC Asia-Pacific)*. IEEE. 2014, pp. 1–4.

[76] John Reimers, Lea Dorn-Gomba, Christopher Mak, and Ali Emadi. “Automotive traction inverters: Current status and future trends”. In: *IEEE Transactions on Vehicular Technology* 68.4 (2019), pp. 3337–3350.

[77] Jelena Loncarski, Mattia Ricco, Vítor Monteiro, and Vito Giuseppe Monopoli. “Efficiency comparison of a DC-DC interleaved converter based on SiC-MOSFET and Si-IGBT devices for EV chargers”. In: *2020 ieee 14th international conference on compatibility, power electronics and power engineering (cpe-powereng)*. Vol. 1. IEEE. 2020, pp. 517–522.

[78] Kichiro Yamamoto, Katsuji Shinohara, and Hitoshi Makishima. “Comparison between flux weakening and PWM inverter with voltage booster for permanent magnet synchronous motor drive”. In: *Proceedings of the Power Conversion Conference-Osaka 2002 (Cat. No. 02TH8579)*. Vol. 1. IEEE. 2002, pp. 161–166.

[79] Kichiro Yamamoto, Katsuji Shinohara, and Takahiro Nagahama. “Characteristics of permanent-magnet synchronous motor driven by PWM inverter with voltage booster”. In: *IEEE Transactions on Industry Applications* 40.4 (2004), pp. 1145–1152.

[80] Power Semiconductors. “Application manual power semiconductors”. In: *SEMIKRON International GmbH: Nuremberg, Germany* (2010).

[81] Tsuyoshi Funaki, Masashi Matsushita, Masashi Sasagawa, Tsunenobu Kimoto, and Takashi Hikihara. “A study on SiC devices in synchronous rectification of DC-DC converter”. In: *APEC 07-Twenty-Second Annual IEEE Applied Power Electronics Conference and Exposition*. IEEE. 2007, pp. 339–344.

[82] Alessandro Acquaviva, Artem Rodionov, Anton Kersten, Torbjörn Thiringer, and Yujing Liu. “Analytical conduction loss calculation of a mosfet three-phase

inverter accounting for the reverse conduction and the blanking time". In: *IEEE Transactions on Industrial Electronics* 68.8 (2020), pp. 6682–6691.

[83] Sepideh Amirpour, Torbjörn Thiringer, and Dan Hagstedt. "Energy Loss Analysis in a SiC/IGBT Propulsion Inverter over Drive Cycles Considering Blanking time, MOSFET's Reverse Conduction and the Effect of Thermal Feedback". In: *2020 IEEE Energy Conversion Congress and Exposition (ECCE)*. IEEE. 2020, pp. 1505–1511.

[84] Dong Jiang, Rolando Burgos, Fei Wang, and Dushan Boroyevich. "Temperature-dependent characteristics of SiC devices: Performance evaluation and loss calculation". In: *IEEE Transactions on Power Electronics* 27.2 (2011), pp. 1013–1024.

[85] K Vinoth Kumar, Prawin Angel Michael, Joseph P John, S Suresh Kumar, et al. "Simulation and comparison of SPWM and SVPWM control for three phase inverter". In: *ARPN journal of engineering and applied sciences* 5.7 (2010), pp. 61–74.

[86] Michael H Bierhoff and Friedrich W Fuchs. "Semiconductor losses in voltage source and current source IGBT converters based on analytical derivation". In: *2004 IEEE 35th Annual Power Electronics Specialists Conference (IEEE Cat. No. 04CH37551)*. Vol. 4. IEEE. 2004, pp. 2836–2842.

[87] Yuan Zhu, Mingkang Xiao, Xiezu Su, Gang Yang, Ke Lu, and Zhihong Wu. "Modeling of conduction and switching losses for IGBT and FWD based on SVPWM in automobile electric drives". In: *Applied Sciences* 10.13 (2020), p. 4539.

[88] Zhi Yang, Fei Shang, Ian P Brown, and Mahesh Krishnamurthy. "Comparative study of interior permanent magnet, induction, and switched reluctance motor drives for EV and HEV applications". In: *IEEE Transactions on Transportation Electrification* 1.3 (2015), pp. 245–254.

[89] Hicham El Hadraoui, Mourad Zegrari, Ahmed Chebak, Oussama Laayati, and Nasr Guennouni. "A multi-criteria analysis and trends of electric motors for electric vehicles". In: *World Electric Vehicle Journal* 13.4 (2022), p. 65.

[90] Anton Dianov, Fabio Tinazzi, Sandro Calligaro, and Silverio Bolognani. "Review and classification of MTPA control algorithms for synchronous motors". In: *IEEE Transactions on Power Electronics* 37.4 (2021), pp. 3990–4007.

[91] Adrian Młot, Mariusz Korkosz, Piotr Grodzki, and Marian Łukaniszyn. "Analysis of the proximity and skin effects on copper loss in a stator core". In: *Archives of Electrical Engineering* 63.2 (2014), pp. 211–225.

[92] Rafal Wrobel, Daniel E Salt, Antonio Griffo, Nick Simpson, and Phil H Mellor. "Derivation and scaling of AC copper loss in thermal modeling of electrical machines". In: *IEEE Transactions on Industrial Electronics* 61.8 (2013), pp. 4412–4420.

[93] Katsumi Yamazaki and Shinjiro Watari. “Loss analysis of permanent-magnet motor considering carrier harmonics of PWM inverter using combination of 2-D and 3-D finite-element method”. In: *IEEE Transactions on Magnetics* 41.5 (2005), pp. 1980–1983.

[94] Lin Liu, Youguang Guo, Gang Lei, and Jianguo Zhu. “Efficient iron loss estimation of interior PMSMs in electric vehicles: analytical modelling and experimental validation”. In: *IEEE Transactions on Applied Superconductivity* 34.8 (2024), pp. 1–5.

[95] Peter Gustavsson Mårdestam and Adam Lundin. *Efficiency Analysis of a Planetary Gearbox*. 2010.

[96] Vasilios Bakolas, Philipp Roedel, Oliver Koch, and Michael Pausch. “A first approximation of the global energy consumption of ball bearings”. In: *Tribology Transactions* 64.5 (2021), pp. 883–890.

[97] S Laruelle, C Fossier, C Changenet, F Ville, and S Koechlin. “Experimental investigations and analysis on churning losses of splash lubricated spiral bevel gears”. In: *Mechanics & Industry* 18.4 (2017), p. 412.

[98] S Seetharaman and A Kahraman. “Load-independent spin power losses of a spur gear pair: model formulation”. In: (2009).

[99] Jiageng Ruan, Paul Walker, and Nong Zhang. “A comparative study energy consumption and costs of battery electric vehicle transmissions”. In: *Applied energy* 165 (2016), pp. 119–134.

[100] Frans JR Verbruggen, Varun Rangarajan, and Theo Hofman. “Powertrain design optimization for a battery electric heavy-duty truck”. In: *2019 American Control Conference (ACC)*. IEEE. 2019, pp. 1488–1493.

[101] Monica Tutuianu, Pierre Bonnel, Biagio Ciuffo, Takahiro Haniu, Noriyuki Ichikawa, Alessandro Marotta, Jelica Pavlovic, and Heinz Steven. “Development of the World-wide harmonized Light duty Test Cycle (WLTC) and a possible pathway for its introduction in the European legislation”. In: *Transportation research part D: transport and environment* 40 (2015), pp. 61–75.

[102] Emma Arfa Grunditz and Torbjörn Thiringer. “Characterizing bev powertrain energy consumption, efficiency, and range during official and drive cycles from gothenburg, sweden”. In: *IEEE Transactions on Vehicular Technology* 65.6 (2015), pp. 3964–3980.

[103] T Holdstock, A Sorniotti, M Everitt, M Fracchia, S Bologna, and S Bertolotto. “Energy consumption analysis of a novel four-speed dual motor drivetrain for electric vehicles”. In: *2012 IEEE vehicle power and propulsion conference*. IEEE. 2012, pp. 295–300.

[104] Minghui Hu, Shuang Chen, and Jianfeng Zeng. “Control strategy for the mode switch of a novel dual-motor coupling powertrain”. In: *IEEE Transactions on Vehicular Technology* 67.3 (2017), pp. 2001–2013.

[105] Jianjun Hu, Lingling Zheng, Meixia Jia, Yi Zhang, and Tao Pang. “Optimization and model validation of operation control strategies for a novel dual-motor coupling-propulsion pure electric vehicle”. In: *Energies* 11.4 (2018), p. 754.

[106] Richard Bellman. “Dynamic programming”. In: *science* 153.3731 (1966), pp. 34–37.

[107] Kailas S Holkar and Laxman M Waghmare. “An overview of model predictive control”. In: *International Journal of control and automation* 3.4 (2010), pp. 47–63.

[108] Cong Guo, Chunyun Fu, Ronghua Luo, and Guanlong Yang. “Energy-oriented car-following control for a front-and rear-independent-drive electric vehicle platoon”. In: *Energy* 257 (2022), p. 124732.

[109] Huseyin Ayhan Yavasoglu, Junyi Shen, Chuan Shi, Metin Gokasan, and Alireza Khaligh. “Power Split Control Strategy for an EV Powertrain With Two Propulsion Machines”. In: *IEEE Transactions on Transportation Electrification* 1.4 (2015), pp. 382–390. DOI: 10.1109/TTE.2015.2504406.

[110] Arbaaz Khan, Mohammad Hossain Mohammadi, Vahid Ghorbanian, and David Lowther. “Efficiency map prediction of motor drives using deep learning”. In: *IEEE Transactions on Magnetics* 56.3 (2020), pp. 1–4.

[111] Arbaaz Khan, Mohammad Hossain Mohammadi, Vahid Ghorbanian, and David Lowther. “Transfer learning for efficiency map prediction”. In: *2020 IEEE 19th Biennial Conference on Electromagnetic Field Computation (CEFC)*. IEEE. 2020, pp. 1–4.

[112] Mohamed Abdulsamad, Himavarsha Dhulipati, and Hicham Chaoui. “Comprehensive Drive-Cycle-Based Analysis of Hairpin vs Stranded Windings for EV”. In: *2024 IEEE International Conference on Power Electronics, Drives and Energy Systems (PEDES)*. IEEE. 2024, pp. 1–6.

[113] Xibo Yuan and Jiabin Wang. “Torque distribution strategy for a front-and rear-wheel-driven electric vehicle”. In: *IEEE Transactions on Vehicular Technology* 61.8 (2012), pp. 3365–3374.

[114] Masayuki Sanada and Shigeo Morimoto. “Efficiency improvement at high-speed operation using large air-gap configuration for PMSM”. In: *2008 18th International Conference on Electrical Machines*. IEEE. 2008, pp. 1–6.

[115] DK Kana Padinharu, Guang-Jin Li, ZQ Zhu, Ziad Azar, Richard Clark, and Arwyn Thomas. “Effect of airgap length on electromagnetic performance of permanent magnet vernier machines with different power ratings”. In: *IEEE Transactions on Industry Applications* 58.2 (2021), pp. 1920–1930.

[116] Huai-cong Liu and Minseong Lee. “Design Analysis of an Interior Permanent Magnet Synchronous Motor with Hybrid Hair-Pin and Litz Wire Windings”. In: *Electronics* 14.17 (2025), p. 3350.

[117] Taha El Hajji, Sami Hlioui, François Louf, Mohamed Gabsi, Anouar Belahcen, Guillaume Mermaz-Rollet, and M’hamed Belhadi. “Ac losses in windings: Review and comparison of models with application in electric machines”. In: *IEEE Access* 12 (2023), pp. 1552–1569.

[118] Tobia Marcucci and Russ Tedrake. “Warm start of mixed-integer programs for model predictive control of hybrid systems”. In: *IEEE Transactions on Automatic Control* 66.6 (2020), pp. 2433–2448.

[119] Joel Andersson, Joris Gillis, Greg Horn, Jim Rawlings, and Moritz Diehl. “CasADi—A software framework for nonlinear optimization and optimal control”. In: *Mathematical Programming Computation* 11.1 (2018), pp. 1–36.

[120] Qian Chen, Xun Fan, Guohai Liu, Liang Xu, and Meimei Xu. “Regulation of high-efficiency region in permanent magnet machines according to a given driving cycle”. In: *IEEE Transactions on Magnetics* 53.11 (2017), pp. 1–5.

[121] ZQ Zhu, WQ Chu, and Y Guan. “Quantitative comparison of electromagnetic performance of electrical machines for HEVs/EVs”. In: *CES Transactions on Electrical Machines and Systems* 1.1 (2017), pp. 37–47.

[122] Mlungisi Ntombela, Kabeya Musasa, and Katleho Moloi. “A Comprehensive Review for Battery Electric Vehicles (BEV) Drive Circuits Technology, Operations, and Challenges”. In: *World Electric Vehicle Journal* 14.7 (2023), p. 195.

[123] Uwe Vollmer and Uwe Schäfer. “An at-all operating points highly efficient PMSM for HEV”. In: *World Electric Vehicle Journal* 2.4 (2008), pp. 334–342.

[124] Andreas Krings. “Iron losses in electrical machines-influence of material properties, manufacturing processes, and inverter operation”. PhD thesis. KTH Royal Institute of Technology, 2014.

[125] Oskar Theliander, Anton Kersten, Manuel Kuder, Weiji Han, Emma Arfa Grunditz, and Torbjorn Thiringer. “Battery Modeling and Parameter Extraction for Drive Cycle Loss Evaluation of a Modular Battery System for Vehicles Based on a Cascaded H-Bridge Multilevel Inverter”. In: *IEEE Transactions on Industry Applications* 56.6 (2020), pp. 6968–6977. DOI: 10.1109/TIA.2020.3026662.

[126] Lennart Harnefors. “Control of power electronic converters and variable-speed drives”. In: *Västerås, Sweden, Department of Electronics, Mälardalens University* (2002).

[127] Haiyi Fang, Xiaoli Duan, Yang Yang, Yiyan Wang, and Guangzhao Luo. “Deadbeat control of permanent magnet synchronous motor based on mras parameter

identification". In: *2020 23rd International Conference on Electrical Machines and Systems (ICEMS)*. IEEE. 2020, pp. 161–166.

[128] Bicheng Chen, Carsten Wulff, Konstantin Etzold, Patrick Manns, Georg Birmes, Jakob Andert, and Stefan Pischinger. "A comprehensive thermal model for system-level electric drivetrain simulation with respect to heat exchange between components". In: *2020 19th IEEE Intersociety Conference on Thermal and Thermomechanical Phenomena in Electronic Systems (ITherm)*. IEEE. 2020, pp. 558–567.

[129] Alexandre Bourgault, Omolbanin Taqavi, Ze Li, Glenn Byczynski, and Narayan C Kar. "Advanced Lumped Parameter Thermal Network for Modeling of Cooling Solutions in Electric Vehicle Motor Applications". In: *IEEE Transactions on Magnetics* (2024).

[130] Arendt Wintrich, Ulrich Nicolai, Werner Tursky, and Tobias Reimann. *Application manual power semiconductors*. Vol. 2. ISLE Verlag Ilmenau, Germany, 2015.

[131] J Durand de Gevigney, Christophe Changenet, Fabrice Ville, and Philippe Velex. "Thermal modelling of a back-to-back gearbox test machine: Application to the FZG test rig". In: *Proceedings of the Institution of Mechanical Engineers, Part J: Journal of Engineering Tribology* 226.6 (2012), pp. 501–515.

[132] Peng Tang, Zhiguo Zhao, and Haodi Li. "Transient temperature field short-term prediction of electric drive gearbox based on thermal network static and dynamic graph construction". In: *Applied Thermal Engineering* 248 (2024), p. 123323.

[133] Thien-Phuoc Nguyen, Thanh-Anh Huynh, Chin-Wei Chang, and Min-Fu Hsieh. "An Accurate MTPA Control for IPMSM Considering Variations of Motor Parameters and Temperatures". In: *2023 IEEE Vehicle Power and Propulsion Conference (VPPC)*. IEEE. 2023, pp. 1–6.

[134] Silong Li, Bulent Sarlioglu, Sinisa Jurkovic, Nitin R Patel, and Peter Savagian. "Analysis of temperature effects on performance of interior permanent magnet machines for high variable temperature applications". In: *IEEE Transactions on Industry Applications* 53.5 (2017), pp. 4923–4933.

[135] Jun-Hyeok Lee, Tae-Gyeom Woo, Dong-Sup Jin, and Young-Doo Yoon. "Neural Network-based MTPA Control Considering Temperature Variation in IPMSMs". In: *2024 IEEE Energy Conversion Congress and Exposition (ECCE)*. IEEE. 2024, pp. 6264–6269.